RECORD
2024/5

CARBONATITE, LAMPROPHYRE AND HOST ROCKS IN THE NORTHERN AILERON PROVINCE

DE Kelsey, IOH Fielding, MTD Wingate, RH Smithies, RE Turnbull, BV Ribeiro, R Maas, A Wainwright, CL Kirkland, K Goemann, SS Romano, M Dröllner

GOVERNMENT OF WESTERN AUSTRALIA
Department of **Energy, Mines, Industry Regulation and Safety**

Geological Survey of Western Australia

Department of **Energy, Mines, Industry Regulation and Safety**

GOVERNMENT OF WESTERN AUSTRALIA

RECORD 2024/5

CARBONATITE, AILLIKITE LAMPROPHYRE AND HOST ROCKS IN THE NORTHERN AILERON PROVINCE

DE Kelsey, IOH Fielding, MTD Wingate, RH Smithies, RE Turnbull, BV Ribeiro[1], R Maas[2], A Wainwright[2], CL Kirkland[1], K Goemann[3], SS Romano[1], M Dröllner[1]

1 Timescales of Mineral Systems Group, Curtin Frontier Institute of Geoscience Solutions (C-FIGS), School of Earth and Planetary Sciences, Curtin University, Bentley WA 6102

2 School of Geography, Earth and Atmospheric Sciences, University of Melbourne, Parkville VIC 3010

3 Central Science Laboratory, University of Tasmania, Sandy Bay TAS 7005

PERTH 2024

Geological Survey of Western Australia

MINISTER FOR MINES AND PETROLEUM
Hon David Robert Michael MLA

DIRECTOR GENERAL, DEPARTMENT OF ENERGY, MINES, INDUSTRY REGULATION AND SAFETY
Richard Sellers

EXECUTIVE DIRECTOR, GEOLOGICAL SURVEY AND RESOURCE STRATEGY
Michele Spencer

REFERENCE
The recommended reference for this publication is:
Kelsey DE, Fielding IOH, Wingate MTD, Smithies RH, Turnbull RE, Ribeiro BV, Maas R, Wainwright A, Kirkland CL, Goemann K, Romano SS, Dröllner M 2024, Carbonatite, aillikite lamprophyre and host rocks in the northern Aileron Province: Geological Survey of Western Australia, Record 2024/5, 37p.

ISBN 978-1-74168-051-5
ISSN 2204-4345

A catalogue record for this book is available from the National Library of Australia

Grid references in this publication refer to the Geocentric Datum of Australia 1994 (GDA94). Locations mentioned in the text are referenced using Map Grid Australia (MGA) coordinates, Zone 52. All locations are quoted to at least the nearest 100 m.

Curtin University: John de Laeter Centre and Curtin Frontier Institute of Geoscience Solutions acknowledgement
Isotope and element analyses were conducted using instrumentation at the GeoHistory laser ablation inductively coupled plasma mass spectrometry (ICP-MS) Facility and the sensitive highresolution ion microprobe (SHRIMP) facilities at the John de Laeter Centre (JdLC) at Curtin University, with the financial support of the Australian Research Council and the AuScope National Collaborative Research Infrastructure Strategy (NCRIS). Method development, analysis, and data reduction were performed by the Curtin Frontier Institute of Geoscience Solutions (C-FIGS).

The TESCAN Integrated Mineral Analyser (TIMA) instrument was funded by a grant from the Australian Research Council (LE140100150) and is operated by the JdLC with the support of the Geological Survey of Western Australia, The University of Western Australia and Murdoch University.

University of Melbourne acknowledgement
Whole-rock isotope analyses were conducted using the Nu Instruments™ Sapphire multi-collector inductively coupled plasma mass spectrometry (MCICPMS) facility at the Melbourne Analytical Geochemistry (MAG) in the School of Geography, Earth and Atmospheric Sciences at the University of Melbourne. Method development, analysis, and data reduction were performed by Roland Maas and Ashlea Wainwright of MAG.

University of Tasmania acknowledgement
Electron probe microanalyses were conducted on a JEOL JXA-8530F Plus instrument at the Central Science Laboratory, University of Tasmania, which was purchased with the financial support of Australian Research Council Linkage Infrastructure, Equipment And Facilities (LIEF) grant LE160100032. Method development was performed by Karsten Goemann, analysis by Sandra Romano and Karsten Goemann, and data reduction by Sandra Romano, Karsten Goemann and David Kelsey.

Acknowledgement of Country
We respectfully acknowledge Aboriginal peoples as the Traditional Custodians of this land on which we deliver our services to the communities throughout Western Australia. We acknowledge their enduring connection to the lands, waterways and communities and pay our respects to Elders past and present.

Published 2024 by the Geological Survey of Western Australia
This Record is published in digital format (PDF) and is available online at <www.demirs.wa.gov.au/GSWApublications>.

Further details of geoscience products are available from:
First Floor Counter
Department of Energy, Mines, Industry Regulation and Safety
100 Plain Street
EAST PERTH WA 6004
Telephone: +61 8 9222 3459 Email: publications@demirs.wa.gov.au
www.demirs.wa.gov.au/GSWApublications

Cover image: Oblique aerial view of the Aileron–Warumpi Province (photograph taken in 2007 by Catherine Spaggiari)

Contents

Appendices

Available with the PDF online as an accompanying digital resource

Figures

Tables

Carbonatite, aillikite lamprophyre and host rocks in the northern Aileron Province

DE Kelsey, IOH Fielding, MTD Wingate, RH Smithies, RE Turnbull, BV Ribeiro[1], R Maas[2], A Wainwright[2], CL Kirkland[1], K Goemann[3], SS Romano[1], M Dröllner[1]

Abstract

The Western Australian portion of the Paleoproterozoic Aileron Province is poorly characterized due to its remoteness and poor outcrop. Exploration diamond cores drilled in 2020 and 2023 into a prominent east–west-trending belt of high magnetic intensity in the northern Aileron Province offer a rare and valuable opportunity to characterize this crystalline basement geology, which is almost entirely known only in the subsurface. From these diamond drillcores we derive lithology, mineralogy, geochemistry, mineral chemistry, isotope and geochronology data. The drillcores consist of granitic gneisses with magmatic crystallization ages of 1776–1767 Ma – ages that overlap with the c. 1770 Ma ages of felsic plutons of the Carrington Suite – that occur together with gabbronoritic gneiss, as well as younger garnet-bearing granitic gneiss (1608 Ma), metamorphosed banded iron-formation and pelitic migmatite. Gabbronoritic gneiss, metamorphosed banded iron-formation and some Fe-rich pelitic migmatite are highly magnetic and likely contribute to the regional high magnetic intensity. The high-intensity magnetic belt is distinct in including the 1750–1640 Ma Lake Mackay Quartzite and unnamed Fe-rich pelitic rocks of similar age; whereas, the metasedimentary 1858–1799 Ma Lander Rock Formation appears to be absent. The Lander Rock Formation is widespread elsewhere throughout the Aileron Province and occurs in lower magnetic intensity regions to the immediate north and south of the high-intensity magnetic belt studied here. Granulite facies metamorphism to produce partial melting and migmatization of granitic and pelitic rocks occurred at 1594–1575 Ma, based on U–Pb analyses of zircon rims. Some of the gneissic rocks are intruded by aillikite-type lamprophyre (also highly magnetic) and carbonatite, which are distinctly non-metamorphosed. Carbonatite is of high exploration interest due to the occurrence of Nb (in pyrochlore) and elevated light rare earth elements (LREE). Host-rock alteration and local sodic (antiskarn) metasomatism are common in the drillcores, with the most intense metasomatism in the vicinity of lamprophyre and carbonatite intrusions. Carbonatite and lamprophyre typically do not occur in proximity to each other, except in one drillcore that preserves strongly interlayered lamprophyre and carbonatite, indicating a cogenetic relationship. The magmatic crystallization age for emplacement of lamprophyre and carbonatite proved challenging using U–Pb zircon and U–Pb and Lu–Hf apatite geochronology. A maximum crystallization age of c. 690 Ma is proposed, which is younger than a U–Pb perovskite date of c. 806 Ma reported for intrusion of aillikite about 60 km to the south within the Aileron Province (Sudholz et al., 2023). Aillikites documented in our study appear to be more fractionated than those reported in Sudholz et al. (2023). This difference in fractionation could be important in relation to the capacity to form Nb–REE mineralizing carbonatite magmas.

KEYWORDS: carbonatite, geochronology, geological history, isotope geochemistry, lamprophyre, Precambrian, Proterozoic

Introduction

Carbonatite (sövite) and lamprophyre (aillikite) have been intersected in drillcore in the northern Aileron Province, central Australia, representing a major new find of ultrapotassic alkaline rocks in Australia (see also Sudholz et al., 2023). In particular, the intersection of carbonatite in this area has generated major exploration interest in this remote and poorly understood region due to significant intersections of rare earth element (REE) and Nb mineralization (e.g. Encounter Resources Ltd, 2023, 2024; WA1 Resources Ltd, 2022, 2023). Aillikites are a rare subclass of carbonate-rich ultramafic lamprophyre characterized by strong SiO_2 undersaturation, groundmass carbonate and melanite (Ti-rich andradite garnet) (Tappe et al., 2006; Veter et al., 2017). Aillikites contain many of the common minerals and textures observed in kimberlites and lamproites (i.e. olivine, clinopyroxene, perovskite, phlogopite, ilmenite and spinel) but differ in their abundant groundmass clinopyroxene, carbonate, phenocrystic olivine, and absence of feldspathoids (e.g. leucite) (Tappe et al., 2006; Veter et al., 2017).

Globally, there is a close spatial and probably temporal association between carbonatite and aillikite lamprophyre, and such relationships have been linked to the early stages of intracontinental rifting, including that related to supercontinent breakup (see Sudholz et al., 2023, for references). The Aileron Province carbonatites and lamprophyres, including those documented by Sudholz et al., (2023), are proximal to the southwestern margin of

1 Timescales of Mineral Systems Group, Curtin Frontier Institute of Geoscience Solutions (C-FIGS), School of Earth and Planetary Sciences, Curtin University, Bentley WA 6102

2 School of Geography, Earth and Atmospheric Sciences, University of Melbourne, Parkville VIC 3010

3 Central Science Laboratory, University of Tasmania, Sandy Bay TAS 7005

the North Australian Craton (e.g. Kelsey et al., 2022b; Martin et al., 2022) and within the region affected by intracratonic rifting related to Rodinia breakup and development of the Neoproterozoic Centralian Superbasin (Walter et al., 1995; Walter and Veevers, 1997).

This study of five drillcores characterizes geological features of carbonatite, lamprophyre and their host rocks from the tenement held by Encounter Resources Ltd by presenting lithology, mineralogy, geochemistry, isotope and geochronology data. The aim is to provide constraints on the geological setting and ages of these important rocks. The broader purpose is to provide a chrono-magmatic framework for further studies into REE and Nb mineralizing systems, as Australia moves towards new energy sources and a greater reliance on critical minerals.

Location and geological background

The Paleoproterozoic Aileron Province is located in central Australia and is part of the southern portion of the North Australian Craton (NAC). The Aileron Province is located mostly within the Northern Territory with an overall east–west-trending structural grain over a strike length of about 1100 km. Approximately 175 km of that distance is in Western Australia, located entirely within the Kiwirrkurra Indigenous Protected Area (IPA) and Ngururrpa IPA (e.g. Simeonova and Hardwick, 2023). The likely western termination of the Aileron Province and the NAC is the north-northeast-trending Lasseter Shear Zone, which is buried under cover of the Phanerozoic Canning Basin (Kelsey et al., 2022b; Martin et al., 2022). Farther west under cover, crystalline basement is interpreted to be the isotopically distinct Percival Lakes Province (Kelsey et al., 2022b; Lu et al., 2022), equivalent to the Punmu Seismic Province (Doublier et al., 2020) or the isotopically defined Mirning Ocean (Kirkland et al., 2017; Gardiner et al., 2018; Zhao et al., 2022), which is buried beneath the main depocentre of the Canning Basin (e.g. Frogtech Geoscience, 2017; Zhan, 2018; Doublier et al., 2020). To the south of the Aileron Province is the late Paleoproterozoic to Mesoproterozoic Warumpi Province, and the two are separated by the Central Australian Suture (e.g. Scrimgeour et al., 2005a; Hollis et al., 2013). It remains unresolved whether the Central Australian Suture defines the southern margin of the NAC, or whether the Warumpi Province is also part of the NAC (Scrimgeour et al., 2005b; Hollis et al., 2013; Martin et al., 2022; March et al., 2024).

An excellent summary of the geology and time–space evolution of the Aileron Province is provided by Scrimgeour (2013a). Nevertheless, comprehensive understanding of the geology and geological evolution of the western Aileron Province is hampered by remoteness, access difficulties and extensive regolith cover. However, the western Aileron Province is considered to largely consist of 1858–1799 Ma metasedimentary rocks of the Lander Rock Formation (and equivalents) that are intruded by suites of felsic and mafic meta-igneous intrusive rocks, including:

- 1779 to 1767 Ma granitic rocks of the Carrington Suite (Young et al., 1995a; Young et al., 1995b; Edgoose et al., 2008a, 2008b; Hollis et al., 2013; Scrimgeour, 2013a),
- unnamed c. 1624 to 1604 Ma granitic rocks (Kositcin et al., 2013; Scrimgeour, 2013a; Beyer, 2017; Kelsey et al., 2022b; Wingate et al., 2022a)
- c. 1615 Ma Rapide Granite (Kositcin et al., 2014)
- c. 1570 to 1530 Ma Southwark Suite and Wabudali Granite (Young et al., 1995a; Young et al., 1995b; Cross et al., 2005a; Scrimgeour, 2013a; Kositcin and McGloin, 2017)
- numerous dated and undated meta-igneous mafic intrusive rocks (Close et al., 2004; Vandenberg et al., 2006; Edgoose et al., 2008b; Scrimgeour, 2013a; Spaggiari et al., 2016).

In the Northern Territory, the c. 1780 Ma metasedimentary Reynolds Range Group, and age equivalents — for example, the Nyirripi beds (Rubatto et al., 2001; Cross et al., 2005b; Worden et al., 2006; Worden et al., 2008) — unconformably overlies the Lander Rock Formation. The Reynolds Range Group has been interpreted to occur undercover within the Northern Territory, almost reaching the Western Australian border (Edgoose et al., 2008a); albeit, under Lake Mackay. However, it is unknown whether the Reynolds Range Group occurs in Western Australia. Limited data from the poorly age-constrained 1750–1640 Ma Lake Mackay Quartzite, which has been recognized only in the Western Australian portion of the Aileron Province, suggest that it is younger than the Reynolds Range Group (see below).

The drillcores investigated here are located within a distinct east–west-trending, fault-bounded belt about 25 km wide and 200 km long, straddling the Western Australia–Northern Territory border. The belt has higher magnetic intensity than rocks to the north and south (Fig. 1). Little is known about the geology of this belt as outcrop is poor. The Lander Rock Formation is currently mapped to the north and south of this belt, but not within it (Edgoose et al., 2008a, 2008b; Spaggiari et al., 2016). However, distinct layering recognizable in magnetic intensity maps suggests that metasedimentary rocks are abundant in the belt, at least in Western Australia. Where there is outcrop, the belt consists of metasedimentary rock (quartzite), and detrital zircon age data from this outcrop were used to define the Lake Mackay Quartzite, which has a maximum deposition age of either 1750 ± 19 Ma (1σ, single analysis), or a more conservative estimate of 1775 ± 7 Ma based on the 15 youngest analyses (GSWA 184341; Kirkland et al., 2009; Hollis et al., 2013). A more recently dated sample of interpreted Lake Mackay Quartzite yields a maximum deposition age of either 1697 ± 21 Ma for the youngest two analyses on a single zircon, or a more conservative estimate of 1745 ± 10 Ma for the youngest 15 analyses (GSWA 184344, Wingate et al., 2024b). These data suggest the Lake Mackay Quartzite is younger than the >c. 1800 Ma Lander Rock Formation and probably also the Reynolds Range Group. In addition, a thick package of metasedimentary magnetite–apatite-rich garnet–biotite–muscovite ± sillimanite schist (Wingate et al., 2022b; Kelsey et al., 2022a; Fielding et al., 2023) was previously intersected by drilling of a magnetic anomaly on the southern margin of this belt in 2010 (Reddy, 2012). A sample of this schist yielded a maximum depositional age of either 1766 ± 15 Ma (1σ), or more conservatively 1802 ± 7 Ma (GSWA 243061, Wingate et al., 2022b). Thus, it remains equivocal whether this package is a part of the Lake Mackay Quartzite or whether it could be an equivalent (or part) of the Reynolds Range Group. Additional garnet–

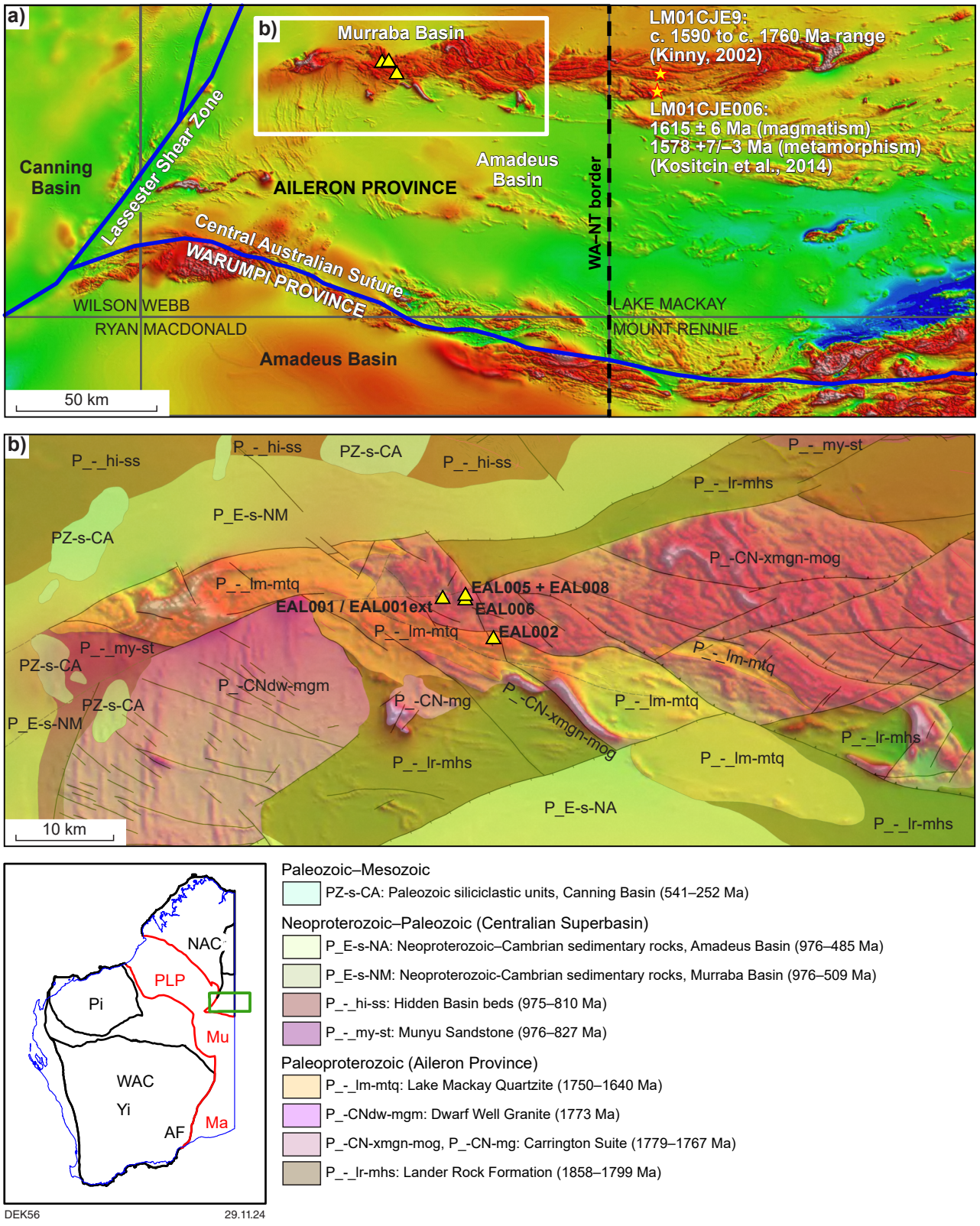

Figure 1. Location map of the study area: a) reduced to pole (RTP) magnetic image of a portion (all of the WA portion) of the Aileron and Warumpi Provinces, which occur either side of the Central Australian Suture, to highlight the high-intensity magnetic belt in the northern Aileron Province that straddles the border. The flat, featureless magnetic intensity parts of the map are where basement is buried beneath younger strata of the Centralian Superbasin (Amadeus and Murraba Basins) and Canning Basin, as well as by regolith. Two existing geochronology samples (LM01CJE9, LM01CJE006) of the Rapide Granite from the high-intensity magnetic belt in Northern Territory are shown. Abbreviations for inset: AF, Albany–Fraser Orogen; Ma, Madura Province; Mu, Musgrave Province; NAC, North Australian Craton; Pi, Pilbara Craton; PLP, Percival Lakes Province; WAC, West Australian Craton; Yi, Yilgarn Craton. The green box in the inset shows the location of the main image; b) Enlargement of the area inside the white rectangle in (a), showing reduced to pole magnetic image overlain by detail of the 1:250 000 interpreted basement geology within, and to the north and south of, the high-intensity magnetic belt, as well as locations of the drillcores (EAL001 / EAL001ext, EAL002, EAL005, EAL008, EAL006) sampled for this study. Age ranges in the legend were obtained from the GSWA Explanatory Notes System (ENS) for the 1:250 000 interpreted bedrock geology layer in GeoVIEW <geoview.dmp.wa.gov.au/geoview/?Viewer=GeoView>

sillimanite-bearing metasedimentary rocks have been reported in this belt from reverse circulation (RC) drilling (Wray, 2023) and were encountered in the drillcores reported herein. Nevertheless, the portion of the belt in the Northern Territory was interpreted to be characterized dominantly by a variety of weakly foliated granites, with rarer possible middle amphibolite to granulite facies metasedimentary rocks and, at the easternmost end, abundant mafic intrusive rocks (Edgoose et al., 2008a).

Metagranitic rocks in the high-intensity magnetic belt can be divided into two distinct suites. First, an outcrop sample of granitic gneiss yielded an igneous crystallization age of 1780 ± 10 Ma (GSWA 184343, Wingate et al., 2024f). Second, the metagranitic Rapide Granite of the Northern Territory has a magmatic crystallization age of 1615 ± 6 Ma and a metamorphic age, based on high-U zircon rims, of 1578 +7/−3 Ma (sample LM01CJE006, Kositcin et al., 2014). Another sample of Rapide Granite was originally dated by Kinny (2002) and provided an inconclusive spread of data from c. 1760 to 1590 Ma. Zircon from altered, mica-poor granitic gneiss in the set of drillcores presented herein previously yielded a magmatic crystallization age of 1608 ± 7 Ma and an age for high-grade metamorphism of 1577 ± 7 Ma (GSWA 203749, Wingate et al., 2022a). More information and discussion of the geology of this high-intensity magnetic belt, including the occurrence of carbonatite and lamprophyre, is provided later in this study.

More than 250 lamprophyre pipes with diameters typically between 180 m and 300 m are known to intrude the southern Aileron Province (Sudholz et al., 2023) in Western Australia, some 60 km south of the current study area, but they do not outcrop. They intrude the Neoproterozoic (Tonian) Bitter Springs Formation (logs in drilling appendices of report by van Raalte, 2023; pers. comm. Peter Haines, 2023) but not the late Neoproterozoic (Ediacaran) Angas Hills Formation (Spaggiari et al., 2016); thus, potentially bracketing their emplacement age. A perovskite common-Pb isochron concordia intercept date of 806 ± 22 Ma (n = 57, MSWD = 0.64) reported by Sudholz et al. (2023) is consistent with lamprophyre emplacement during the Neoproterozoic.

The Neoproterozoic Amadeus and Murraba Basins of the Centralian Superbasin and the Phanerozoic Canning Basin unconformably overlie the Aileron (and Warumpi) Province (e.g. Haines et al., 2015; Spaggiari et al., 2016; Haines and Allen, 2017; Haines et al., 2018). More recent sediments – especially aeolian dune fields – also overlie and bury the crystalline basement (Spaggiari et al., 2016; Haines et al., 2018).

Study site and sample details

Samples for this study come from five diamond drillcores within a poorly exposed belt of high magnetic intensity in the northern Aileron Province in Western Australia. These drillcores provide the most extensive window into the geology of this belt. A total of 202 samples were collected, including 198 for petrography, 38 for whole-rock geochemistry, eight for geochronology and 13 for whole-rock isotope analysis.

The cores were drilled in 2020, 2022 and 2023 by Encounter Aileron Pty Ltd — a subsidiary of Hamelin Resources Pty Ltd and Encounter Resources Ltd — initially (until February 2021) as part of a joint venture with Newcrest Mining Limited within their tenement E 80/5169 (McGregor et al., 2021; Simeonova and Hardwick, 2023; Simeonova, 2024). Some of the drilling was co-funded under the Western Australian government's Exploration Incentive Scheme (EIS). The tenement is approximately 70 km west of the Western Australia–Northern Territory border, 80 km north of Kiwirrkurra and 440 km south of Halls Creek. A summary of the diamond drilling is provided in Table 1, and the drillhole locations are shown in Figure 1.

Methodology

Whole-rock geochemistry

Crushing and sample preparation for whole-rock geochemistry was undertaken at the GSWA Laboratory at Carlisle. Milling and geochemical analysis was undertaken at ALS using the methodology outlined in Lowrey et al. (2023). Standard major element oxides were analysed together with 51 trace elements including Li, Au, Re, F, Cl and, for some rock types, C. Geochemical data are available in GeoVIEW at <https://geoview.dmp.wa.gov.au/geoview/?Viewer=GeoView>.

Table 1. Diamond drillcores by Encounter Aileron Pty Ltd within tenement E 80/5169 as part of its Aileron project

Hole ID	*EIS co-funded?*	*Northing (m)*	*Easting (m)*	*Dip (°)*	*Azimuth (°)*	*Length (m)*	*End of hole (m)*	*Collar date*	*Target name*
EAL001	Yes	7547143	424991	-60	360	157.8	157.8	6 Oct 2020	Hoschke
EAL001ext	No	7547143	424991	-60	360	414.7	572.5	11 May 2023	Hoschke
EAL002	Yes	7543072	429832	-60	180	384.5	463.3	11 May 2023	Caird
EAL005	Yes	7547479	427149	-60	180	388.5	473.1	11 May 2023	Crean
EAL006	No	7547013	427143	-60	180	452.0	520	11 May 2023	Crean
EAL008	No	7547479	427150	-60	360	119.3	208	26 June 2023	Crean

NOTE: UTM coordinates are Zone 52. Additional details can be found in drilling reports by McGregor et al. (2021), Simeonova and Hardwick (2023) and Simeonova (2024)

Electron probe microanalysis

All electron probe microanalysis (EPMA) was conducted at the University of Tasmania, using a JEOL JXA-8530F Plus field emission electron microprobe equipped with five wavelength-dispersive spectrometers. The EPMA is computer controlled by JEOL PC-EPMA and Probe For EPMA (version 13.8) and Probe Image software packages from Probe Software Inc. were used for all data acquisition and processing.

Silicates

Instrument operating conditions included an accelerating voltage of 15 kilovolts (kV), a beam current of 10 nanoamperes (nA), and a 5 micrometre (µm) defocussed beam. Matrix corrections of Armstrong-Love/Scott φ(ρz) (Armstrong, 1988) and Henke mass absorption coefficients were used for data reduction. Mean atomic number (MAN) background correction (e.g. Donovan and Tingle, 1996; Donovan et al., 2016) was used over traditional two-point background interpolation. Well-characterized natural minerals were used as standards for microprobe analytical sessions. Cations were calculated for biotite and amphibole using the principal component regression method of Li et al. (2020a, 2020b, 2022) and for all other minerals using the stoichiometric method of Droop (1987). Mineral abbreviations are as defined in Korhonen et al. (2020) and compositional parameters that define the chemistry of individual minerals are reported using THERMOCALC notation (e.g. White et al., 2014a,b). Amphibole type naming, incorporated into the calculation method of Li et al. (2020a), is according to International Mineralogical Association (IMA2012) nomenclature of Hawthorne et al. (2012). Excess F in apatite may be due to F occupying sites in addition to hydroxyl (Marincea et al., 2022), although this possibility for site assignment has not been explicitly accounted for.

Carbonates

Compositional analyses of carbonates were acquired with an accelerating voltage of 15 kV, a beam current of 10 nA, and a beam diameter of 10 µm, using the analyzing crystals LIFL for Mn and Fe; PETL for Ca, Ti, Sr and Ba; and TAP for Na and Mg. Lα X-ray lines were used for analysis of Sr and Ba and Kα lines for all other elements. The calibration standards were synthetic rutile for Ti; strontium titanite for Sr; jadeite Tawmaw for Na; rhodonite Broken Hill for Mn, baryte Cow Green Mine for Ba (all P&H Developments, UK); hematite Minas Gerais H 92649 for Fe (McGuire et al., 1992); calcite NMNH 136321 for Ca (Jarosewich and MacIntyre, 1983); and olivine MongOL Sh11-2 for Mg (Batanova et al., 2019).

Peak and background counting times were 10 seconds for Na, Ca and Ti; 20 seconds for Mg, Mn, Fe, Ba; and 30 seconds for Sr. The intensity data were corrected for time-dependent intensity (TDI) variations using a self-calibrated correction for Mg, Ca, Fe, and Sr. The mean atomic number (MAN) method was used for background correction, including continuum absorption correction for all elements (Donovan and Tingle, 1996). Unknown and standard intensities were corrected for deadtime. Oxygen was calculated by cation stoichiometry and included in the matrix correction. Carbon was calculated by stoichiometry of 0.333 atoms of carbon to 1 atom of oxygen for best matrix correction accuracy (Moy et al., 2023). The matrix correction method was Armstrong-Love/Scott φρZ with the LINEMU mass absorption coefficient dataset. Corrections were applied to Ti for interference by Ba; to Fe for interference by Mn, and to Ba for interference by Ti (Donovan et al., 1993).

Pyrochlore

Compositional analyses of pyrochlore were acquired with an accelerating voltage of 16 kV, a beam current of 100 nA, and a beam diameter of 5 µm. Tests were carried out before analysis to ensure the pyrochlore grains could withstand the beam conditions for the duration of each analysis. The shared background method was used for background correction (Allaz et al. 2019). Unknown and standard intensities were corrected for deadtime. Oxygen was calculated by cation stoichiometry and included in the matrix correction. Hydrogen was calculated by stoichiometry of 1 atom of hydrogen to 7 atoms of oxygen for best matrix correction accuracy (Moy et al., 2023). The matrix correction method was Armstrong-Love/Scott φρZ with the LINEMU mass absorption coefficient dataset. Additional measurement parameters, including interference corrections (Donovan et al., 1993) are listed in Appendix 1. Cation site assignment and site normalization was based on Zurevinski and Mitchell (2004) and Velásquez-Ruiz et al. (2024). The mineral abbreviation used for pyrochlore (i.e. pcl) is from Yavuz and Yavuz (2024).

In situ apatite Lu–Hf geochronology

In situ Lu–Hf geochronology was conducted on apatite grains mounted in polished epoxy mounts at the John de Laeter Centre GeoHistory Facility, by staff of the Frontier Institute for Geoscience Solutions, at Curtin University, Australia. The analytical setup includes a 193 nanometre (nm) argon fluoride (ArF) excimer laser equipped with a Laurin Technic S155 sample cell coupled to an Agilent 8900 triple quadrupole tandem inductively coupled plasma mass spectrometer (ICP-MS/MS) using 20% NH_3 in He pre-mixed gas in the reaction cell. This configuration enables measurement of Lu and Hf isotopes following the approach of Simpson et al. (2021). A 'squid' mixing device (Laurin Technic) was used to smooth the aerosol pulses between the laser and mass spectrometer. The sample cell was flushed with ultrahigh purity He (320 ml.min^{-1}) and N_2 (4 ml.min^{-1}), both of which were passed through an inline Hg trap. The low flow rate of N_2 was added to the carrier gas before the ICP torch to enhance sensitivity (Hu et al., 2008). Apatite samples and reference materials (Bamble and HR; Simpson et al., 2021, 2024) were ablated using a fluence of ~3.5 J.cm^{-2}, a repetition rate of 10 Hz and a circular laser beam of 80 µm; whereas, glass reference material NIST SRM 610 was ablated using a circular beam of 38 µm. Instrument tuning was performed using NIST SRM 610 glass in single quadrupole (no-gas mode) to optimize plasma conditions, minimize oxide interferences and maximize ^{175}Lu sensitivity using a circular laser beam of 50 µm. After shifting to tandem (MS/MS) mode, the ICP-MS was tuned for maximum sensitivity for Hf reaction products using NH_3/He with a flow rate of 22% (Ribeiro et al., 2024). To check for potential systematic errors in Lu–Hf from pulse/analogue (P/A) conversion in the 8900-detector system, we performed repeated measurements of the NIST SRM 610 using different spot sizes and detector modes for ^{175}Lu (33 µm and 64 µm), resulting in a P/A factor of ~0.18.

Glass NIST SRM 610 with known $^{176}Lu/^{177}Hf$ and $^{176}Hf/^{177}Hf$ composition (Nebel et al., 2009) was employed as the primary reference material; whereas, a secondary matrix correction was performed using Bamble apatite (1102 ± 5 Ma; Simpson et al., 2024) following procedures described in Ribeiro et al. (2024), whereas HR apatite was employed as a secondary reference and treated as an unknown. The Lu–Hf isochron ages were calculated using the inverse approach (Li and Vermeesch, 2021) in IsoplotR (Vermeesch, 2018) with ^{176}Lu decay constant after Scherer et al. (2001) and Söderlund et al. (2004). Inverse isochron ages and analytical uncertainties are stated at the 2 standard errors (2SE) level. Bamble apatite yield a matrix uncorrected inverse isochron age of 1157 ± 15 Ma (n = 25, MSWD = 1.1), indicating a positive offset of ~5% compared to the isotope dilution Lu–Hf reference age. After applying this correction factor to $^{176}Lu/^{176}Hf$ ratios (apatite reference materials and unknowns), the HR apatite yielded an inverse isochron age of 344 ± 14 Ma (n = 16, MSWD = 0.6), in agreement with multi-session Lu–Hf dates from this laboratory and elsewhere (Simpson et al., 2021, 2024).

Apatite U–Pb–trace elements

U–Pb–trace element analysis of apatite grains in polished epoxy mounts was conducted at the same facility at Curtin University as Lu–Hf analysis outlined above. The analytical setup includes a 193 nm ArF excimer laser equipped with a Laurin Technic S155 sample cell coupled to an Agilent 7900 ICP-MS for simultaneous measurement of U–Pb isotopes and trace elements. A 'squid' mixing device (Laurin Technic) was used to smooth the aerosol pulses between the laser and mass-spectrometer. The sample cell was flushed with ultrahigh purity He (320 $ml.min^{-1}$) and N_2 (4 $ml.min^{-1}$), both of which were passed through an inline Hg trap. The low flow rate of N_2 was added to the carrier gas before the ICP torch to enhance sensitivity (Hu et al., 2008). The samples and reference materials were ablated using a laser fluence of ~2.8 $J.cm^{-2}$, repetition rate of 7 Hz and a circular beam of 50 µm. Each analysis consisted of 20 seconds (s) of baseline acquisition, followed by a 30 s sample ablation and a 10 s fast washout. Instrument tunning was performed using NIST SRM 610 glass to optimise plasma conditions, maximise instrument sensitivity and minimise oxide interferences.

Unknowns were bracketed by a suite of apatite and glass reference materials. McClure Mountain apatite (Schoene and Bowring, 2006) and NIST SRM 610 were employed as primary reference materials for U–Pb and trace elements, respectively. Madagascar (Thomson et al., 2012) and FC-Duluth apatite (Schmitz et al., 2003; Thomson et al., 2012) and NIST SRM 612 were employed as secondary reference materials and treated as unknowns. Data reduction was performed in iolite 4 software (Paton et al., 2011) using the VizualAge_UComPbine data reduction scheme (Chew et al., 2014) using an exponential with linear equation to account for U–Pb downhole fractionation, and the built-in "Trace Element" data reduction scheme using ^{43}Ca in stoichiometric proportion as internal calibration for apatite unknowns. The U–Pb diagrams and dates were calculated using IsoplotR (Vermeesch, 2018), with ages and uncertainties being presented at the 2SE level. The FC-Duluth apatite yields a lower intercept date of 1091 ± 17 Ma (n = 25, MSWD = 1.7) and the Madagascar apatite yields a lower intercept date of 478 ± 2 Ma (n = 24, MSWD = 1.4), in agreement with expected U–Pb dates for each material.

Whole-rock Rb–Sr, Sm–Nd and Lu–Hf isotope analyses

Whole-rock Rb–Sr, Sm–Nd and Lu–Hf isotope compositions were determined at the University of Melbourne (Woodhead et al., 2019; Dalton et al., 2022; Sudholz et al., 2023). Sample powders (~100 mg) were dissolved in Krogh-style PTFE-lined steel pressure vessels (3:1 HF–HNO_3, 170 °C, 48 hrs; refluxing in HNO_3; second high-pressure stage with 6M HCl, 170 °C, 24 hrs). All samples yielded clear solutions which were gravimetrically split to yield aliquots for separate Rb–Sr, Sm–Nd and Lu–Hf isotope dilution. After equilibrating the aliquots with suitable amounts of ^{85}Rb–^{84}Sr, ^{149}Sm–^{150}Nd and ^{176}Lu–^{180}Hf tracers, Rb and Sr were extracted using a combination of Eichrom Sr resin (for Sr) and AG50W-X8 resin (200–400) for cation exchange (Rb); Sm and Nd were extracted using Eichrom TRU and LN resins; and Lu and Hf were extracted using the single-column technique of Münker et al. (2001). Total processing blanks (<0.05 ng) for each of the 6 elements were negligible.

Isotope analyses were carried out on a Nu Instruments Sapphire multi-collector ICP-MS with sample uptake via a Glass Expansion PFA nebulizer and a CETAC Aridus desolvating system. Instrumental mass bias in Sr, Nd, Sm and Hf isotope runs was corrected by normalizing to $^{88}Sr/^{86}Sr$ = 8.37521, $^{146}Nd/^{145}Nd$ = 2.0719425 (equivalent to the more familiar $^{146}Nd/^{144}Nd$ = 0.7219; Vance and Thirlwall, 2002), $^{152}Sm/^{147}Sm$ = 1.78308 and $^{179}Hf/^{177}Hf$ = 0.7325, using the exponential law as part of an online iterative spike-stripping/internal normalization procedure. Data are reported relative to SRM987 = 0.710230, La Jolla Nd = 0.511860 and JMC475 = 0.282160, respectively. External precision (reproducibility, 2 standard deviations, 2sd) is ±0.000040 (Sr), ±0.000020 (Nd) and ±0.000015 (Hf). Methods for Rb and Lu isotope dilution analyses are based on Waight et al. (2002) and Vervoort et al. (2004), respectively. $^{87}Rb/^{86}Sr$, $^{147}Sm/^{144}Nd$ and $^{176}Lu/^{177}Hf$ measured by isotope dilution have external precisions of ±0.5, ±0.2 and ±1% (2sd), respectively. Results for standard materials acquired in this campaign are listed in Appendix 2. The εNd and εHf values are calculated relative to a modern chondritic uniform reservoir (CHUR) composition with $^{147}Sm/^{144}Nd$ = 0.1960, $^{143}Nd/^{144}Nd$ = 0.512630, $^{176}Lu/^{177}Hf$ = 0.0336 and $^{176}Hf/^{177}Hf$ = 0.282785 (Bouvier et al., 2008). Decay constants are: ^{87}Rb 1.397×10^{11}/yr; ^{147}Sm 6.54×10^{-12}/yr, ^{176}Lu 1.865×10^{-11}/yr.

Results

Basement lithologies

Geological logging of the drillcores listed in Table 1 was undertaken with the aid of HyLogger™ hyperspectral data and was supplemented by sampling for polished thin sections that were mapped with TESCAN Integrated Mineral Analyzer (TIMA) for mineral identification. Overall, the drillcores consist mainly of granitic gneiss with subordinate metagabbronorite and lamprophyre, and rarer paragneiss and carbonatite (Figs 2, 3). Widespread

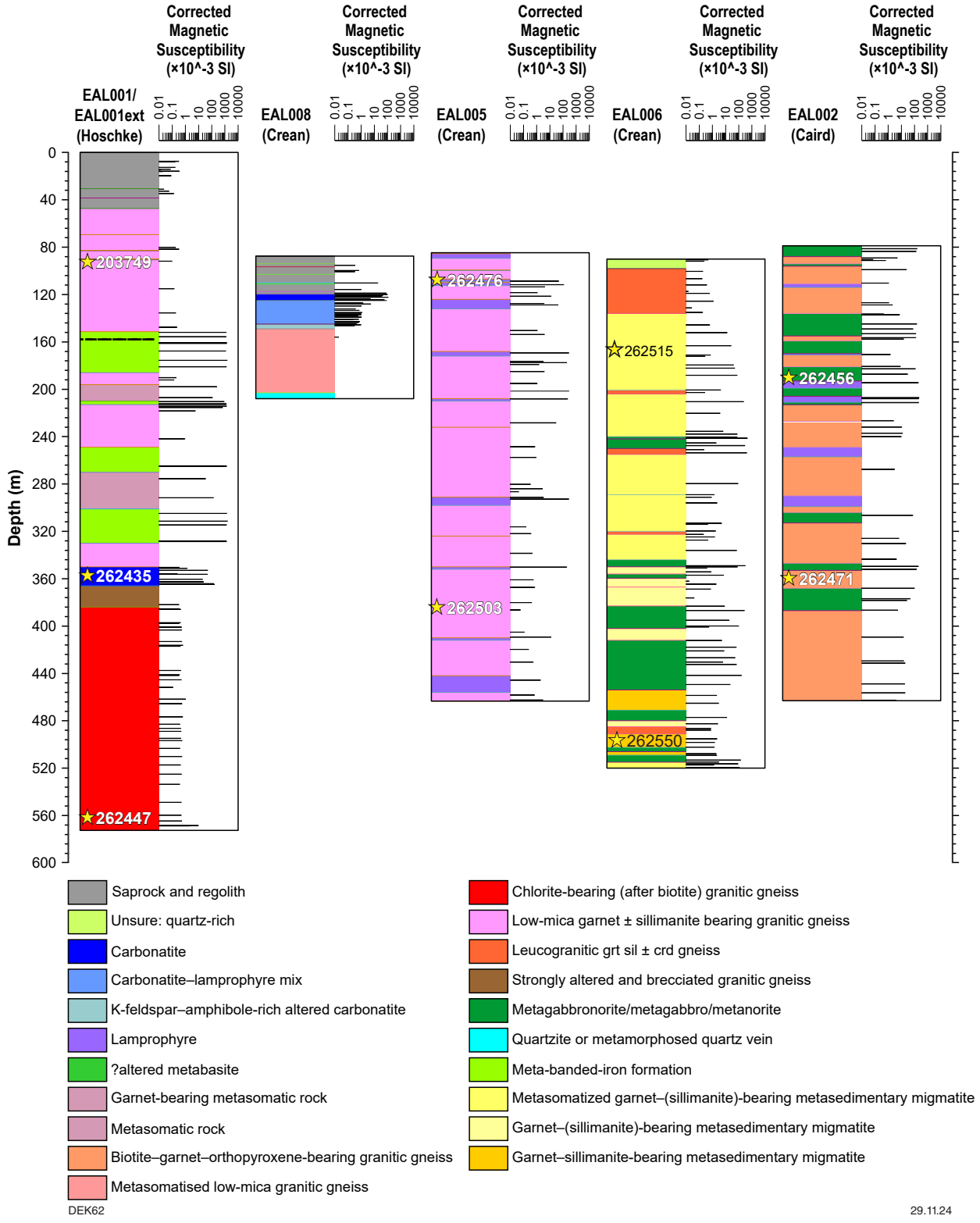

Figure 2. Interpreted lithology logs and measured magnetic susceptibility data for the five studied diamond drillcores from tenement E 80/5169. Lithological logging was undertaken by integrating visual observations with the GSWA HyLogger™ hyperspectral data, thin-section mineralogy and whole-rock geochemistry. HyLogger™ information and data for the drillcores, including photos of rock trays, are available at <geoview.dmp.wa.gov.au/geoview/?Viewer=GeoView> and www.dmirs.wa.gov.au/hylogger. Locations of new and existing GSWA geochronology samples are shown with yellow stars and corresponding sample ID labels. Magnetic susceptibility data was measured by Terra Petrophysics as part of the GSWA program of collecting statewide petrophysical data (MAGIX survey registration number 72803)

Figure 3. Representative lithologies in tenement E 80/5169 drillcores. In all photos, the diameter of drillcore is 47.6 mm: a) Tray 109 (~567–568 m) of EAL001ext. Chlorite-bearing (after biotite) granitic gneiss, featuring leucocratic patches and veins; b) Tray 38 (~194–195 m) of EAL005. Low-mica garnet-bearing granitic gneiss with rare relict igneous feldspar grain shapes (white) preserved. Garnet is also relict, mostly pseudomorphed by biotite–chlorite intergrowths (black patches); c) Tray 7 (~112 m) of EAL006. Sillimanite-rich (white) portion of leucogranitic garnet–sillimanite ± cordierite gneiss; d) Tray 32 (~175–176 m) of EAL002. Wet and dry segments of biotite–garnet–orthopyroxene-bearing granitic gneiss. Garnet is mostly confined to light-coloured layers or domains in the rock (see top right of photo), interpreted as leucosomes from partial melting; e) Tray 2 (~83.0 – 83.3 m) of EAL002. Well-foliated fresh hornblende metagabbronorite; f) Tray 105 (~507.7 m) of EAL006. Well-foliated, fresh segment of garnet–sillimanite-bearing pelitic migmatite. Light-coloured lozenges are interpreted as leucosomes from partial melting; g) Tray 45 (~303 m) of EAL001ext. Metamorphosed banded iron-formation, showing the two distinct textures: planar, zebra-striped, and more granular, spotted; h) Tray 12 (~114.2 – 115.1 m) of EAL002. Lamprophyre with distinct texture of coarse-grained phenocrysts and spidery calcite veining; i) Tray 61 (~365.6 – 365.7 m) of EAL001ext. Strongly layered, pale-pink-coloured carbonatite. Dark grains are a combination of pyrochlore and magnetite. This segment has a mylonitic texture at the base of the carbonatite and is also quartz-bearing; j) Tray 10 (~124–125 m) of EAL008. Strongly layered, mixed carbonatite and lamprophyre

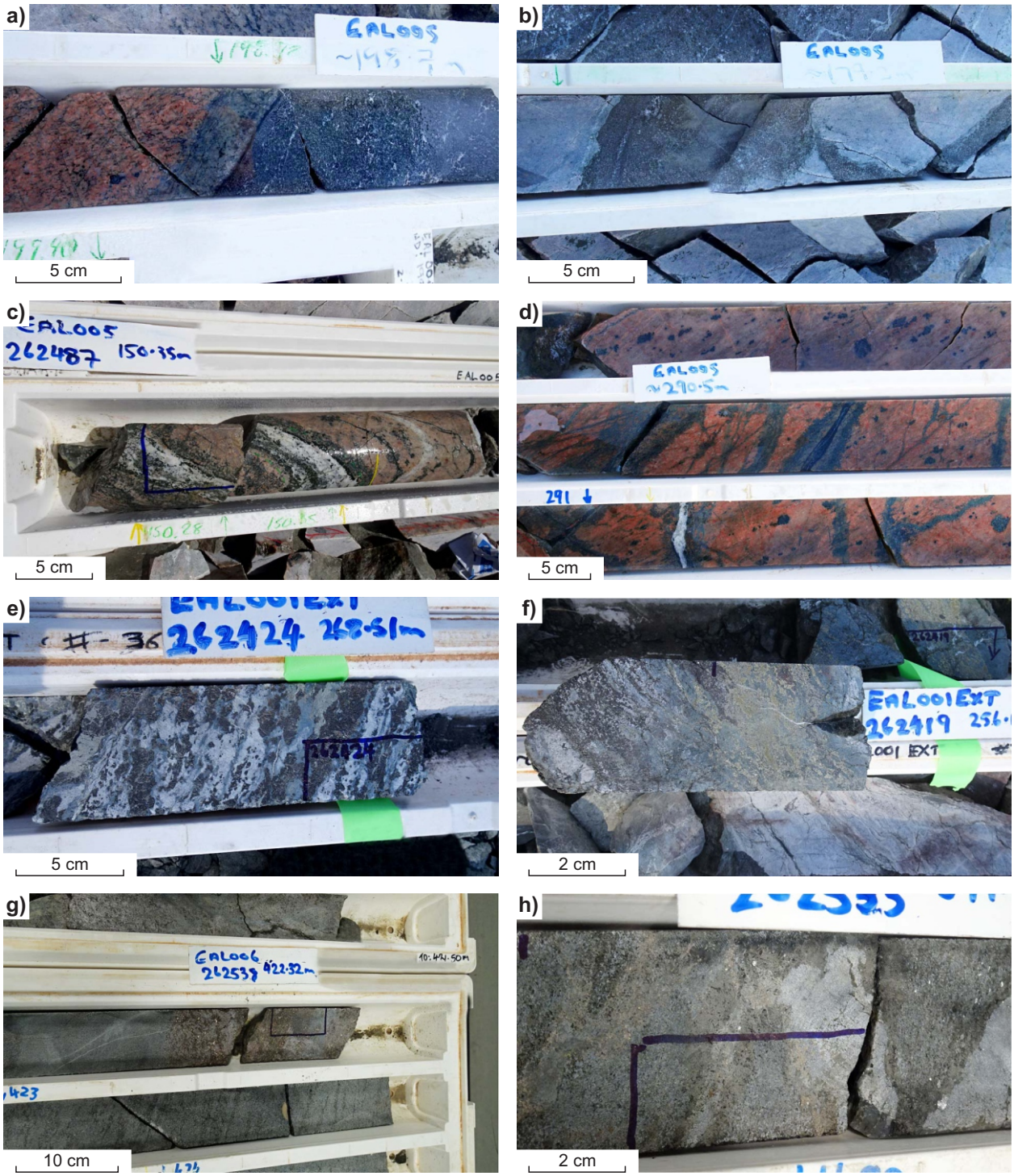

Figure 4. Key contact relationships and alteration in tenement E 80/5169 drillcores. In all photos, the diameter of drillcore is 47.6 mm: a) Tray 39 (~198.7 m) of EAL005. Intrusive contact between non-deformed lamprophyre and gneissic fabric in low-mica garnet-bearing granitic gneiss; b) Tray 33 (~179.2 m) of EAL005. Sharp intrusive contact between non-deformed lamprophyre and brecciated low-mica garnet-bearing granitic gneiss; c) Tray 24 (~150.35 m) of EAL005. Well-developed, discrete and advanced calcite–apatite–aegirine alteration zone ('antiskarn') within low-mica garnet-bearing granitic gneiss. Alteration is zoned from a calcite-rich core to an aegirine-rich outer part; d) Tray 69 (~290.5 m) of EAL005. Altered and metasomatized low-mica garnet ± sillimanite bearing granitic gneiss. Ovoid to round black spots up to ~1 cm in diameter are partly to completely retrogressed garnet. The metasomatic vein network is dominated by mineralogy of blue amphibole, aegirine and albite and, in some cases, features central calcite (white); e) Tray 36 (~268.5 m) of EAL001ext. Blue amphibole–chlorite–green amphibole alteration of banded iron-formation; f) Tray 32 (~256 m) of EAL001ext. Blue amphibole, biotite and pyrite alteration within metamorphosed banded iron-formation; g) Tray 86 (~422.3 m) of EAL006. Zone of hydrous alteration to biotite–garnet–cordierite–orthopyroxene within metagabbronorite. Well-foliated (gneissic) metagabbronorite is located in the row below the biotite-rich alteration; h) Tray 80 (~399 m) of EAL006. Quartz vein-related sulfide–hornblende ± clinopyroxene alteration in metagabbronorite

alteration and metasomatism has affected many rock types and is described in more detail below. Key relative timing relationships constrain the emplacement of lamprophyre but are less clear for carbonatite (Fig. 4). Geological logs, together with corresponding mineralogy as determined by HyLogger™, are shown in Figure 2, and visual documentation of rock types and key rock relationships are provided in Figures 3 and 4.

Four main types of granitic gneiss were identified in the drillcores, and a rare fifth type. First, altered granitic gneiss exhibits a gneissic fabric defined by a relatively abundant Fe–Mg mineral. Plagioclase is strongly orange in drillcore, attesting to hematite alteration (Fig. 3a). In thin section, quartz and microcline are fresh, and accompanied by pyrite, apatite and ilmenite. The Fe–Mg-bearing mineral is typically chlorite, although biotite (together with chlorite) also occurs in some cases. Chlorite is interpreted to have pseudomorphed biotite. Plagioclase is moderately to strongly altered to sericite and minor hematite. The 'type example' of this granitic gneiss occurs in the bottom of EAL001ext (below about 380 m depth). Networks of calcite veins occur locally within this rock type.

The second type of granitic gneiss is strongly altered, low-mica- and garnet-bearing (Fig. 3b). The alteration has partly to completely obliterated the gneissic fabric. The pre-alteration mineralogy is interpreted to be perthitic K-feldspar, quartz, garnet and rare biotite, stringers of sillimanite and possibly sodic plagioclase. Where it is possible to discern, garnet or aggregates of garnet are enveloped by an elliptical-shaped region of leucocratic material (Fig. 3b). This may represent leucosome from in situ partial melting associated with high-grade metamorphism. Local to pervasive alteration (metasomatism) is sodic and is described in the next section. Fine-grained biotite-rich coronae mantling garnet are possibly related to metasomatism. Fine-grained sillimanite occurs in feldspar-bearing portions of the rock, but not in direct contact with garnet. This granitic gneiss is extensively brecciated, resulting in very broken drillcore (essentially large chips), and it has a distinct bleached pale orange–brown colour. Networks of calcite veining are common. This type of granitic gneiss has been dated previously in drillcore EAL001 (depth 91.10 – 93.55 m) and provided a magmatic crystallization age of 1608 ± 7 Ma (GSWA 203749, Wingate et al., 2022a) and in outcrop, indicating a magmatic crystallization age of 1615 ± 6 Ma (sample LM01CJE006, Kositcin et al., 2014). This type of granitic gneiss dominates the upper part of drillcore EAL001, occurs throughout EAL005, and probably forms much of the deeper part of EAL008.

The third type of granitic gneiss is a garnet–sillimanite ± cordierite-bearing, peraluminous, leucogranitic gneiss (Fig. 3c). This rock only occurs in drillcore EAL006 and is characterized by ~5 mm porphyroblastic garnet (± cordierite) and is rich in perthitic, orange K-feldspar. Foliation is commonly defined by trails of euhedral sillimanite aggregates but is poorly developed in portions where sillimanite is rare or absent. Mica is distinctly absent.

The fourth type of granitic gneiss contains garnet and orthopyroxene, is relatively fresh and is common in drillcore EAL002. It is a biotite–mesoperthite–plagioclase–quartz gneiss with a well-defined, anastomosing fabric (Fig. 3d). Garnet typically occurs in lighter-coloured (biotite-poor) layers with diffuse margins, and the layers are interpreted as leucosomes from partial melting. Orthopyroxene is distributed throughout the melanosome part of the rock and is rare in leucosome. Orthopyroxene and garnet typically do not occur in direct contact. Geochronology (GSWA 262471) and geochemistry (see below) confirm this lithology to be granitic gneiss.

The final type of granitic gneiss is rare, only occurring in drillcore EAL006 between about 168 m and 171 m. It is medium-grained, foliated, pale orange–brown rock that has a saccharoidal texture and high Zr (645–710 ppm by portable XRF). The rock is interpreted as a leucogranitic gneiss within altered paragneiss (described below). Geochronology was undertaken on sample GSWA 262515.

A variety of other rock types occur in the studied drillcores. Hornblende metagabbronorite, hornblende metagabbro and hornblende metanorite occur in drillcores EAL002, EAL005 and EAL006 (Fig. 2) and these rock types are essentially fresh in contrast to relatively strongly altered granitic gneisses. Gneissic fabric, parallel to that in granitic gneiss, is defined by aggregates of olive–brown hornblende and elongate grains of pyroxene (Fig. 3e), and the rocks have a granoblastic texture. Rare garnet coronae mantle magnetite and ilmenite and separate those minerals from orthopyroxene in one sample of metanorite from drillcore EAL006.

Sedimentary gneiss (paragneiss) is most abundant in drillcore EAL006, in which textbook stromatic garnet–sillimanite ± cordierite migmatite occurs. Aggregates of sillimanite form a well-defined, anastomosing gneissosity that wraps around, but is also truncated by elongate grains and aggregates of garnet. Some garnets contain inclusions of sillimanite. Locally, porphyroblasts of cordierite are similar in size to garnet. Interpreted in situ leucosomes produced from partial melting have sharp to diffuse boundaries with the garnet–sillimanite melanosomes, and typically do not contain abundant garnet (Fig. 3f). Larger leucosomes have a more elliptical shape interpreted to reflect boudinage. The dominant feldspar is perthitic K-feldspar, which occurs in the matrix as well as in leucosomes. Plagioclase only occurs in some leucosomes. Variable alteration of paragneiss is common, resulting in a pale- to mid-brown rock with relict garnet and progressive consumption of sillimanite.

Rare silica-rich metasedimentary rock occurs in drillcore EAL001 among low-mica garnet-bearing granitic gneiss and above metamorphosed banded iron-formation, and possibly in the uppermost (weathered?) part of EAL006. This rock type is massive, mottled pale orange–brown, and has no distinguishing features, such as bedding or layering, to identify it as metasedimentary. However, geochemistry (see GeoVIEW as not covered below in whole-rock geochemistry section) reveals >87 wt% SiO_2 and strong positive Zr and Hf anomalies in mantle-normalized trace element spider plots, and also elevated Cr and Ni concentrations. Together, these suggest a metasedimentary origin.

Metamorphosed banded iron-formation (Fig. 3g) occurs in drillcores EAL001 and EAL001ext in discrete intervals alternating with low-mica garnet-bearing granitic gneiss between about 150 m and 330 m depth (Fig. 2). The rock has two main morphologies: one as a strongly planar 'zebra-striped' rock and the other as a more granular, spotted iron-formation, with individual spots of grey quartz of about

1.5 mm among magnetite. Micro-faulting and brecciation by networks of calcite veins is common. The mineralogy is dominantly quartz, magnetite and apatite. However, alteration occurs in some intervals, particularly deeper down in the core, closer to where carbonatite occurs, manifest as matted aggregates or radiating sheafs and acicular grains of strongly blue amphibole (Fig. 4e), as well as intergrowths of chlorite and actinolite–winchite, and, less commonly, titanite, kaersutite, biotite, albite, pyrite, bastnäsite and possible Ca-poor amphibole (cummingtonite) (Fig. 4e,f). This alteration is likely related to widespread sodic alteration documented above and in the next subsection.

Alkaline intrusions

Lamprophyre is texturally distinct from the other rock types described above as it is not deformed (Fig. 3h), and clearly cuts the gneissic fabric in those rocks, establishing a relative timing relationship (Fig. 4a,b). Some brecciation of host granitic gneiss is evident in the wallrock to the lamprophyre intrusion (Fig. 4b). Lamprophyre is biotite- and calcite-rich and has a variety of textures at the scale of drillcore, from calcite- and biotite-porphyritic to seriate. The mineralogy is dominated by biotite, calcite and clinopyroxene, and also features apatite, titanite, magnetite (some with Cr-rich cores) and ilmenite. Rare melanite (Ti-andraditic garnet) and interpreted former olivine and perovskite occur in some samples (cf. Sudholz et al., 2023). Calcite commonly occurs as ovoid aggregates or single grains that are variable in size, but commonly 0.5 mm to 1.5 mm in diameter. Calcite is also abundantly distributed throughout the matrix where it is similar in grain size to other minerals such as clinopyroxene, biotite and some apatite, probably intergrown with them. Apatite is anhedral but in numerous cases has straight crystal faces and is intergrown with other minerals such as euhedral, acicular clinopyroxene and biotite. Numerous spidery calcite vein networks anastomose through lamprophyre (e.g. Figs 3h, 4b).

Distinctly pale pink–orange carbonatite occurs in drillcores EAL001ext (below all metamorphosed banded iron-formation) and EAL008 and is calcite-rich (Fig. 3i), although some dolomite-rich intervals occur in EAL008. Strong layering is present, particularly at the boundary with underlying granitic gneiss (Fig. 3i) in EAL001ext and throughout EAL008 (Fig. 3j). The layering is considered to represent magmatic flow rather than a tectonic foliation, as neither rock type is metamorphosed. In EAL001ext, carbonatite is essentially compositionally homogeneous, whereas in EAL008 there is much stronger light and dark compositional layering (Fig. 3j). About 15 m of carbonatite was intersected in EAL001ext, and about 25–30 m in EAL008. The mineralogy of carbonatite in EAL001ext is calcite, apatite, pyrochlore, magnetite and, more rarely, quartz and chlorite, with trace zircon and bastnäsite. In EAL008, the mineralogy of light-coloured portions consists of calcite, dolomite, apatite, biotite, green–blue amphibole (ferri-winchite) and, rarely, pyrochlore; whereas, dark domains or layers have variable mineralogy including biotite, apatite, clinopyroxene, green–blue amphibole, titanite, magnetite, calcite and pyrite. Therefore, in EAL008, there is a strong mineralogical basis to suggest coexisting or unmixed carbonatite–lamprophyre. In EAL008 veins of anhydrite also crosscut carbonatite and the layering in it. Saprock and regolith immediately above carbonatite in drillcore EAL008, at about 90–117 m depth, are extremely apatite rich, contain Fe-hydroxide minerals, pyrochlore, pyrite, magnetite, biotite, ankerite–dolomite and skeletal monazite, and is elevated in REE, U, Sr, Zr, Y, as identified by portable XRF analysis.

Alteration

Low-mica garnet-bearing granitic gneiss described above, in particular, is strongly altered. Although pervasive, this alteration resulted in mottled textures and bleached appearance, and locally discrete, intense metasomatism in zones or networks concentrated along and around fractures (Fig. 4c,d). These intensely metasomatized zones are typically abundant in calcite, apatite, albite and Na-rich plagioclase, and additionally consist of one or more of aegirine, sodic (blue or blue–green) amphibole, titanite, biotite and pyrite. This form of metasomatism has produced a calcsilicate mineral assemblage comparable to fenite or an 'antiskarn' (e.g. Yaxley et al., 2022). Antiskarn alteration is particularly well developed in granitic gneiss (Fig. 4c,d) in the vicinity of lamprophyre intrusions but is not obvious within lamprophyre.

Centimetre-scale garnet–quartz metasomatic zones occur in EAL001ext (Fig. 2) and consist of highly fractured garnet porphyroblasts about 1–4 mm in size, hosted by quartz. Strongly green chlorite intergrown with biotite mantles garnet and also occurs along fractures through garnet. These zones occur among strongly metasomatized rock – interpreted as formerly low-mica garnet-bearing metagranitic rock – and proximal to metamorphosed banded iron-formation.

In drillcore EAL006, there are well-developed biotite–garnet-rich zones up to about 60 cm thick, but typically about 5–10 cm thick. These most commonly occur at the contact between metagabbronorite and (typically) garnet-bearing pelitic migmatite, but they also occur within metagabbronorite where there is no obvious other rock type (Fig. 4g). They are coarse-grained and distinctly non-foliated, with a granofels texture. The mineralogy is dominated by coarse-grained (about 2 mm) biotite and typically 3–4 mm sized (though some up to about 1 cm) porphyroblasts of red garnet. Inclusions of sillimanite needles or spinel occur in some garnet grains. Porphyroblasts of cordierite (up to about 2 mm diameter) and more rarely orthopyroxene (about 1 mm to 1.5 mm long) and disseminated and loosely aggregated grains and blebs (typically about 0.5 mm) of hercynitic spinel also occur. As these zones are distinctly more hydrous and less deformed than the high-grade metamorphic host rocks, they are interpreted to result from a metasomatic process. These zones (see GeoVIEW as not covered in next section) are characterized by elevated Li (>42 ppm), F (>3500 ppm), Y (160–249 ppm) and average heavy rare earth elements (HREE) – i.e. Gd to Lu, 86–138 ppm – concentrations. There are also rare sulfide–hornblende-bearing domains (pyrrhotite ± pyrite) at the margins of clinopyroxene–quartz veins in metagabbro in the same drillcore (Fig. 4h).

Whole-rock geochemistry

Geochemistry of the four main granitic rock types is shown in Figure 5. The degree of alteration variably affecting most samples examined here significantly undermines

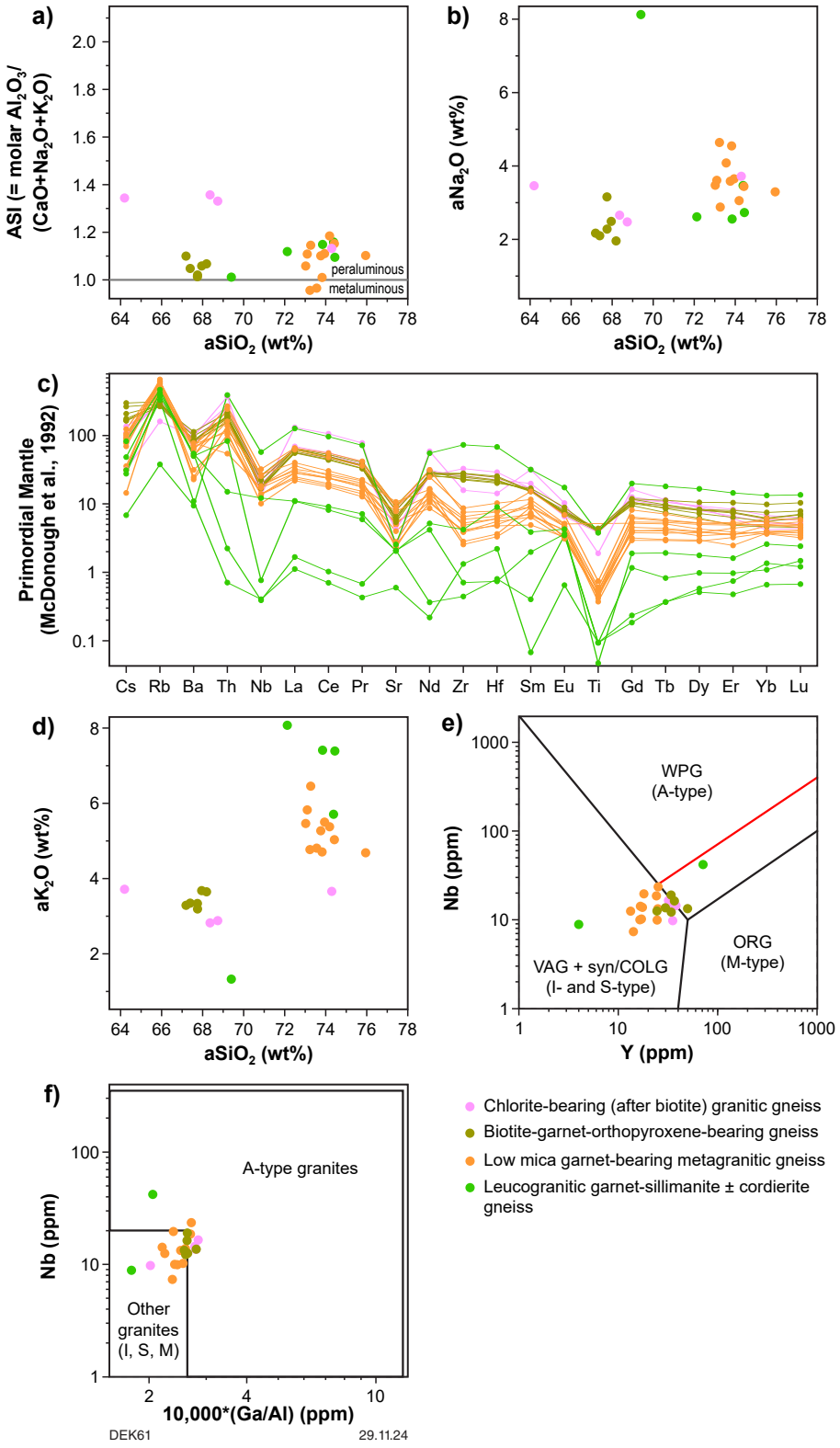

Figure 5. Geochemical summary plots for metagranitic rock samples from drillcore from tenement E 80/5169: a) aluminium saturation index (ASI) vs anhydrous silica ($aSiO_2$); b) anhydrous sodium oxide (aNa_2O) vs anhydrous silica; c) primitive mantle-normalized rare earth element (REE) spider plot; d) anhydrous potassium oxide (aK_2O) vs $aSiO_2$); e) Pearce et al. (1984) Nb vs Y discrimination diagram, WPG = within-plate granite (A-type), ORG = ocean-ridge granite (M-type), VAG = volcanic arc granite (I-type) and COLG = collisional granite (S-type); f) Whalen et al. (1987) Nb vs 10,000*(Ga/Al) A-, I-, S- and M- type granite differentiation plot

the extent to which we can recognize and confidently interpret primary geochemical features of these rocks. Many of the interpretations described below are based on variations in a suite of trace elements which are generally considered relatively immobile during all but intense forms of alteration. For some rock groups, these trace elements form tightly constrained mantle-normalized trace element patterns supporting limited mobility, and we suggest that interpretations based on those elements, for those rock groups, are relatively robust. Other interpretations, particularly those based on variations in alkali elements are significantly less robust.

Two suites of granitic gneiss are recognized: a more primitive, low-SiO_2, more FeO- and MgO-rich suite (garnet–orthopyroxene granitic gneiss, olive-coloured dots, only in EAL002) and a more evolved, higher SiO_2 and lower FeO–MgO suite (low-mica garnet-bearing metagranitic gneiss, orange dots). The garnet–orthopyroxene granitic gneiss has a tightly-constrained range of mantle-normalized incompatible trace-element patterns, suggesting limited mobility of these elements and confirming visual inspection that this type of granitic gneiss is relatively fresh. These rocks are only weakly peraluminous (i.e. alumina saturation index, ASI = molar $Al_2O_3/(CaO + Na_2O + K_2O)$ <1.1; Fig. 5a), straddle the I- to A-type granite boundary (Fig. 5e,f) and fall within the high-K calc-alkaline series. Given the possible A-type affinity and the presence of orthopyroxene, it is possible that this gneiss could be metamorphosed charnockite, particularly as orthopyroxene is not obviously located within leucosome and could, therefore, be a (recrystallized) magmatic mineral. The low-mica garnet-bearing metagranitic gneiss shows a wider spread in both ASI, to significantly more peraluminous compositions (ASI to 1.18; Fig. 5a), and in its normalized trace element patterns (Fig. 5c). Consistently high K_2O (Fig. 5d) places the rock in the transition between high-K calc-alkaline and shoshonite series, and correspondingly high Rb that suggests an S-type rather than I-type origin. This would be consistent with the generally high ASI, and the presence of rare sillimanite, but precise classification remains uncertain given the widespread alteration.

Chlorite-bearing granitic gneiss (pink dots) has mantle-normalized trace element patterns very similar to those of garnet–orthopyroxene granitic gneiss (Fig. 5c), and at equivalent SiO_2 values, also has similar Cr and major element contents (except for CaO and MgO). It shows much higher ASI (Fig. 5a), but given the unusually low CaO contents, this most likely relates to significant alteration of plagioclase. The generally similar incompatible trace element patterns with the garnet–orthopyroxene granitic gneiss make a genetic relationship between the two types plausible, even though those two types of granite do not occur in the same drillcore. Last, the leucogranitic gneiss in drillcore EAL006 that contains sillimanite and garnet ± cordierite (green dots) is moderately peraluminous (average ASI >1.1; Fig. 5a). Its trace element chemistry does not indicate a specific granite type, with the compositional range falling across class divisions (Fig. 5e,f). However, the uniformly high Rb and K_2O contents, similar to those of low-mica garnet-bearing metagranitic gneiss (Fig. 5c,d), are consistent with the ASI values and general peraluminous mineralogy in suggesting that this is metasedimentary gneiss, metasedimentary migmatite or Stype granitic gneiss, or a combination of these. The wide range in mantle-normalized trace element patterns (Fig. 5c), including generally trace-element-depleted patterns with significant positive or negative Eu anomalies, and the presence of contrasting patterns generally similar to the low-mica garnet-bearing granitic gneiss, support the presence of a range of melanosome and leucosome components. These likely relate to partial melting of proximal migmatitic garnet–sillimanite-bearing paragneiss (possibly the unit intersected in the same drillcore).

Hornblende metagabbronorite, and associated metagabbro and metanorite, show relatively similar N-MORB-normalized trace element patterns and linear Nb–Zr correlations that trace back to the origin, permitting a cogenetic and comagmatic liquid line of descent (Fig. 6a). Most samples have Mg# <42, reflecting significant compositional evolution, consistent with mildly LREE-enriched trace element patterns, but with only modest negative Nb anomalies (Fig. 6a) suggesting only a small degree of crustal contamination. Most samples have Nb/Yb ratios (~1.5) only slightly higher than primitive mantle values (1.44; Sun and McDonough, 1989). However, assessing the potential mantle source composition for these rocks is speculative because significant Th depletion in mantle-normalized trace element patterns identify potential secondary extraction of a low-degree melt component. The hornblende metagabbronorite samples are strongly gneissic with two-pyroxene–plagioclase assemblages and abundant hornblende, which is consistent with a residual mineralogy and consistent with small degrees of partial melt extraction.

The studied lamprophyres (n = 8) classify as aillikites (via Tappe et al., 2006, Si vs Fe diagram), a rare subclass of carbonate-rich ultramafic lamprophyre, analogous to those documented by Sudholz et al. (2023). SiO_2 concentrations range from 28.18 wt% to 36.29 wt%, indicating strong silica undersaturation. Mantle-normalized trace element patterns reflect an enriched mantle source similar to the ocean-island basalt (OIB) mantle reservoir, and a lack of negative Nb or Ti anomalies suggests emplacement occurred without crustal contamination (Fig. 6b). Compared to the lamprophyre chemistry presented in Sudholz et al. (2023) which shows near-primary mantle compositions, with Mg# >75, the rocks sampled here have Mg# of 55 to 74, reflecting a wide range of compositional evolution (i.e. greater fractionation). Decreasing Ni and Cr and increasing LREE with decreasing Mg# support fractionation (Fig. 6c,d,e). The alternative possibility, that variation in Mg# reflects large variations in the degree of partial melting of the mantle, is discounted on the basis of such a large variation in Mg# and on the ubiquitously high concentrations of strongly incompatible trace elements (e.g. Th, Nb, La).

The samples of carbonatite presented in this study (n = 10) are classified as calcio-carbonatite by the ternary $MgO–CaO–(FeO+Fe_2O_3+MnO)$ International Union of Geological Sciences (IUGS) rock classification scheme. Trace element patterns for carbonatite largely parallel those of lamprophyre, notably except high field strength elements (HFSE), Zr, Hf and Ti, and are therefore suggestive of a similar mantle source (Fig. 6b). Samples displaying the interlayered style of lamprophyre and carbonatite in drillcore EAL008 (Fig. 3j) commonly have trace element profiles that sit between lamprophyre and purer carbonatite (Fig. 6b), lending support to the suggestion that this interlayering reflects co-magmatic mixing or possibly carbonate–silicate immiscibility-related unmixing for the two rock types.

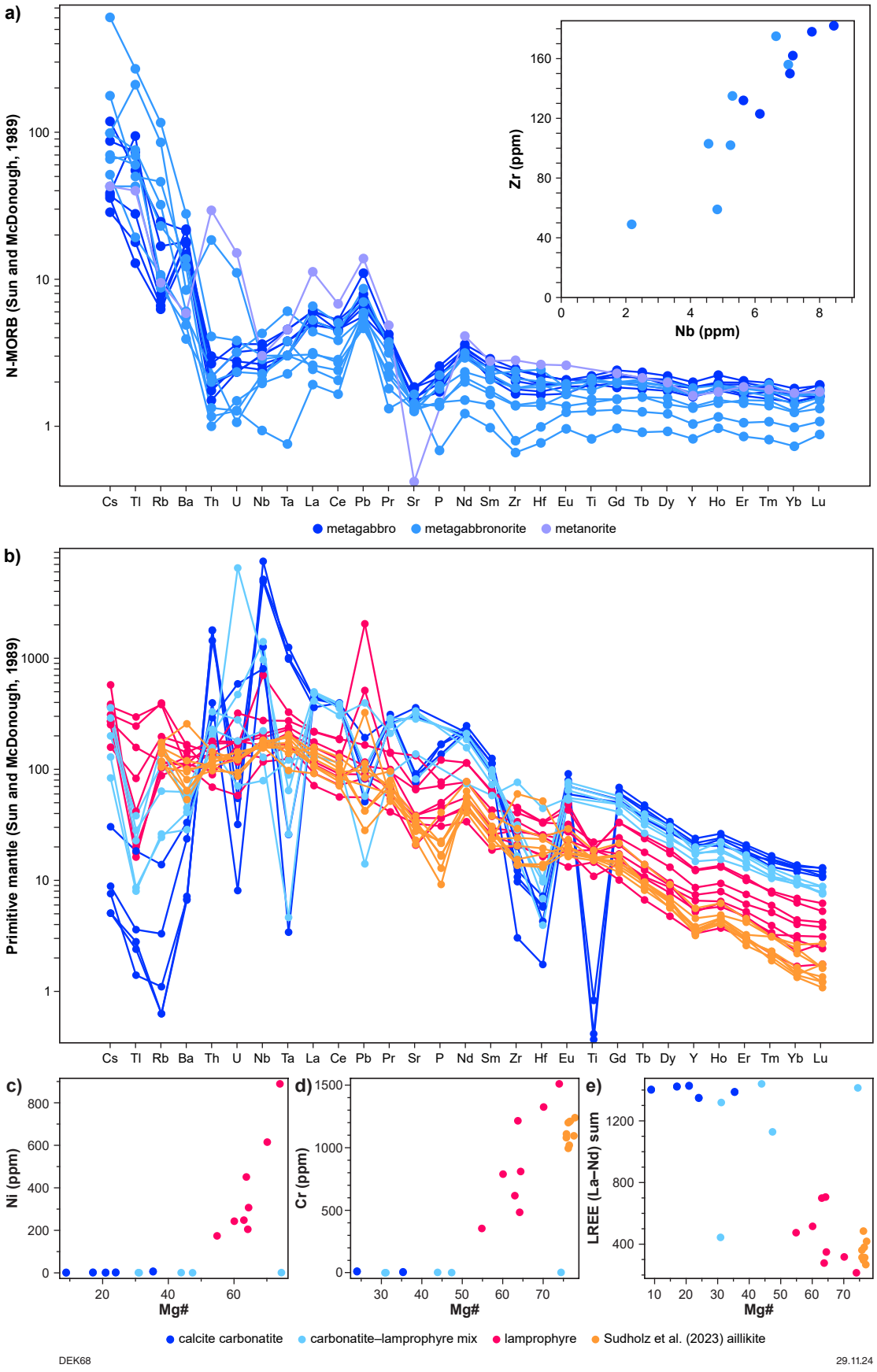

Figure 6. Geochemical summary plots for metagabbroic, lamprophyre and carbonatite rock types from drillcore from tenement E 80/5169: a) N-MORB-normalized trace element spider plot for metagabbronorite, metagabbro and metanorite samples. Inset: Zr vs Nb trace element Harker plot; b) Primitive mantle-normalized trace element spider plot for carbonatite and lamprophyre samples, additionally with lamprophyre (aillikites) geochemical data from Sudholz et al. (2023); c) Ni vs Mg# plot for carbonatite and lamprophyre samples; d) Cr vs Mg# plot for carbonatite and lamprophyre samples, additionally with lamprophyre (aillikites) geochemical data from Sudholz et al. (2023); e) LREE (La–Nd) sum (ppm) vs Mg# plot for carbonatite and lamprophyre samples, additionally with lamprophyre (aillikites) geochemical data from Sudholz et al. (2023)

Mineral chemistry

Reconnaissance EPMA was conducted on a small number of samples, including several lithologies and alteration types (Appendix 3 and Figs 7–13). Low-mica garnet-bearing granitic gneiss (GSWA 262497) has iron-rich garnet (Fig. 7; X_{Fe} = Fe/(Fe + Mg) cations = 0.94 – 0.95; *proportion*$_{almandine}$ = Fe/(Fe + Mg + Mn + Ca) cations = 0.90 – 0.91); sodic plagioclase (*proportion*$_{albite}$ = Na/(Na + K + Ca) cations = 0.81 – 0.99); F- and LREE-rich apatite (Fig. 8; F wt% = 3.79 – 4.13; LREE cations = La^{3+} + Ce^{3+} + Nd^{3+} = 0.019 or 0.29 – 0.46% of Ca site); and two chemically distinct types of biotite (Fig. 9): Ti-rich, coarse-grained matrix biotite (X_{Fe} = 0.60 – 0.67, TiO_2 wt% = 2.8 – 3.3, F wt% = 1.15 – 1.65; Cl wt% = 0.14 – 0.28); and Ferich, fine-grained biotite occurring as a product of retrogression of garnet (X_{Fe} = Fe/(Fe + Mg) cations = 0.78 – 0.82, TiO_2 wt% = 0.05 – 0.07, F wt% = 0.09 – 0.32; Cl wt% = 0.41 – 0.72).

Mineral compositions in two samples of lamprophyre were analyzed (Figs 7–10). One is geochronology sample GSWA 262476 (see below); the other, GSWA 262485, was not analyzed for age determination. Sample 262476 has Cr-poor diopside clinopyroxene (*proportion*$_{diopside}$ = 0.86 – 0.95, *proportion*$_{jadeite}$ = 0.02 – 0.06; Cr_2O_3 wt% = 0.02 – 0.10); biotite (X_{Fe} = Fe/(Fe + Mg) cations = 0.002 – 0.063; TiO_2 wt% = 0.24 – 0.89; F wt% = 0.74 – 1.38; Cl wt% = 0.025 – 0.047); F-rich apatite (F wt% = 2.44 – 3.11; LREE cations = La^{3+} + Ce^{3+} + Nd^{3+} = 0.016 – 0.035, or 0.32 – 0.69% of Ca site; SrO wt% = 0.69 – 0.92); and Sr-bearing calcite (SrO wt% = 0.24 – 0.97). Sample 262485 has melanitic (Ca–Ti-rich) garnet (TiO_2 wt% = 2.5 – 11.37, X_{Fe} = Fe/(Fe + Mg) cations = 0.68 – 0.81, Fe^{3+} cations = 0.07 – 0.30); Cr-poor diopside clinopyroxene (*proportion*$_{diopside}$ = 0.77 – 0.84, *proportion*$_{acmite}$ = 0.13 – 0.20, Cr_2O_3 wt% = 0.003 – 0.012); Frich apatite (F wt% = 2.89 – 3.18, LREE cations = La^{3+} + Ce^{3+} + Nd^{3+} = 0.009 – 0.023, or 0.19 – 0.46% of Ca site, SrO wt% = 0.022 – 0.035); and more Fe-rich biotite (X_{Fe} = Fe/(Fe + Mg) cations = 0.33 – 0.41; TiO_2 wt% = 1.27 – 3.89; F wt % = 0.31 – 0.45; Cl wt% = 0 – 0.013).

Mineral compositions in two samples of carbonatite were analyzed (Figs 8, 11, 12). One is geochronology sample GSWA 262435 (see below); the other, GSWA 262437, was not analyzed for geochronology and is strongly layered, from near the base of carbonatite in drillcore EAL001ext. Sample 262435 has Mn–Sr-bearing calcite (MnO wt% = 0.22 – 0.53; SrO wt% = 0.04 – 0.65); Frich apatite (F wt% = 3.06 – 3.93; LREE cations = La^{3+} + Ce^{3+} + Nd^{3+} = 0.011 – 0.024, or 0.23 – 0.49% of Ca site; SrO wt% = 0.74 – 0.89); and REE–Ta-rich pyrochlore (cation sum of all REE = 0.01 – 0.11 or 1.05 – 9.65% of cations in A-site; TiO_2 wt% = 2.61 – 4.73; Nb_2O_5 wt% = 60.70 – 70.58; Y_2O_3 = 0.11 – 1.12; ZrO_2 wt% = 0.30 – 3.63; Ta_2O_3 wt% = 0.60 – 2.76; ThO_2 wt% = 0.58 – 3.08). Magnetite-rich sample 262437 has Mn–Sr-bearing calcite (MnO wt% = 0.27 – 0.32; SrO wt% = 0.09 – 0.17); F-rich apatite (F wt% = 3.11 – 4.04; LREE cations = La^{3+} + Ce^{3+} + Nd^{3+} = 0.010 – 0.023, or 0.20 – 0.46% of Ca site; SrO wt% = 0.72 – 0.96); and REE–Ta-rich pyrochlore (cation sum of all REE = 0.03 – 0.10, or 2.79 – 4.49% of cations in A-site; TiO_2 wt% = 3.45 – 5.75; Nb_2O_5 wt% = 50.94 – 69.48; Y_2O_3 = 0.16 – 1.07; ZrO_2 wt% = 0.00 – 1.51; Ta_2O_3 wt% = 1.05 – 2.28; ThO_2 wt% = 1.06 – 5.89).

Mineral compositions were analyzed in one sample of a vein of sodic metasomatic rock (Figs 8–10, 13), hosted within low-mica garnet-bearing granitic gneiss collected from 126.08 – 126.14 m depth (GSWA 262480) in EAL005. The rock is rich in calcite, apatite, amphibole and clinopyroxene (see the light-coloured part of rock in Fig. 4c for a visual example). Amphibole is mostly sodic and classifies as magnesio-arfvedsonite (higher Na_2O wt% of 7.79 – 8.67, CaO wt% 0.75 – 1.66, $Na^{+\ B\text{-}site}$ cations 1.67 – 1.82) and ferri-winchite (lower Na_2O wt% of 3.16 – 5.27, CaO wt% 5.51 – 7.99, $Na^{+\ B\text{-}site}$ cations 0.81 – 1.22); and lower-Na, higher-Ca amphibole classifies as hornblende (Na_2O wt% 1.08 – 1.33, CaO wt% 9.95 – 10.69, $Na^{+\ B\text{-}site}$ cations 0.48 – 0.49). Apatite is F-rich (F wt% = 3.20 – 3.49; LREE cations = La^{3+} + Ce^{3+} + Nd^{3+} = 0.013 – 0.044, or 0.25 – 0.88% of Ca site; SrO wt% = 0.74 – 1.14). Clinopyroxene is acmite-rich, Crpoor diopside (*proportion*$_{diopside}$ = 0.71 – 0.81, *proportion*$_{acmite}$ = 0.13 – 0.17, Cr_2O_3 wt% = 0.00 – 0.013).

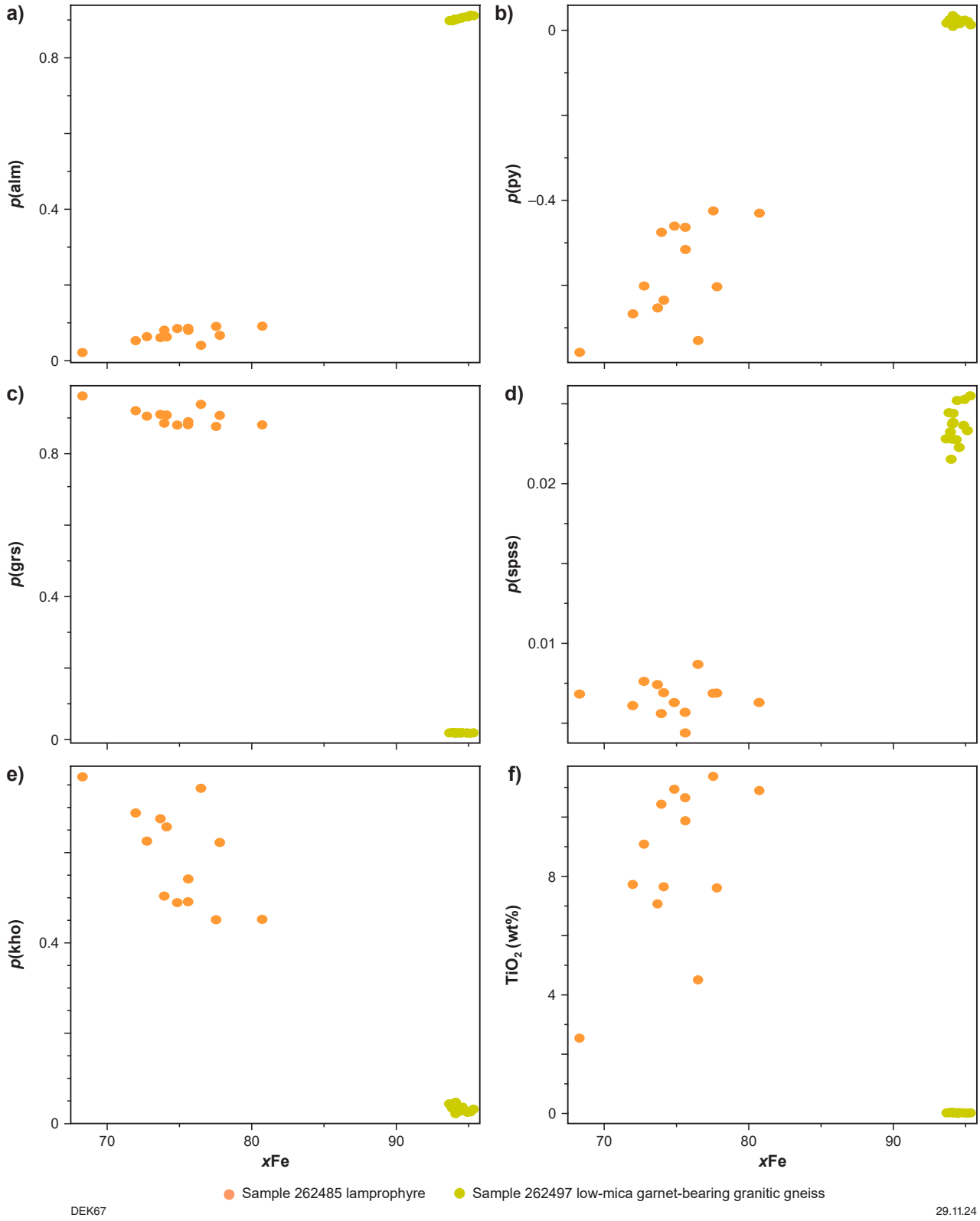

Figure 7. Chemical composition of garnet from electron probe microanalysis (EPMA) data for drillcore samples from tenement E 80/5169

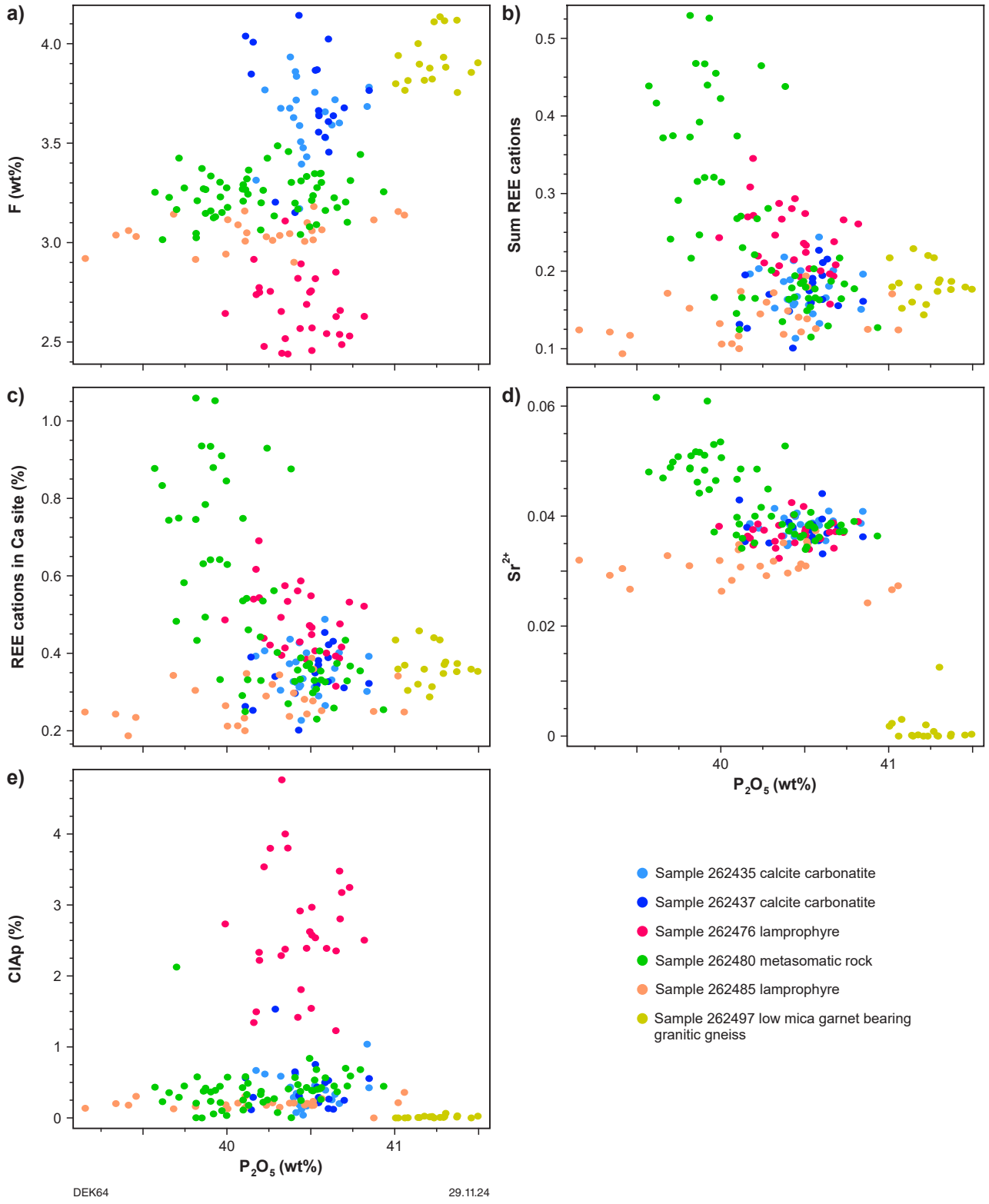

Figure 8. Chemical composition of apatite from electron probe microanalysis (EPMA) data for drillcore samples from tenement E 80/5169

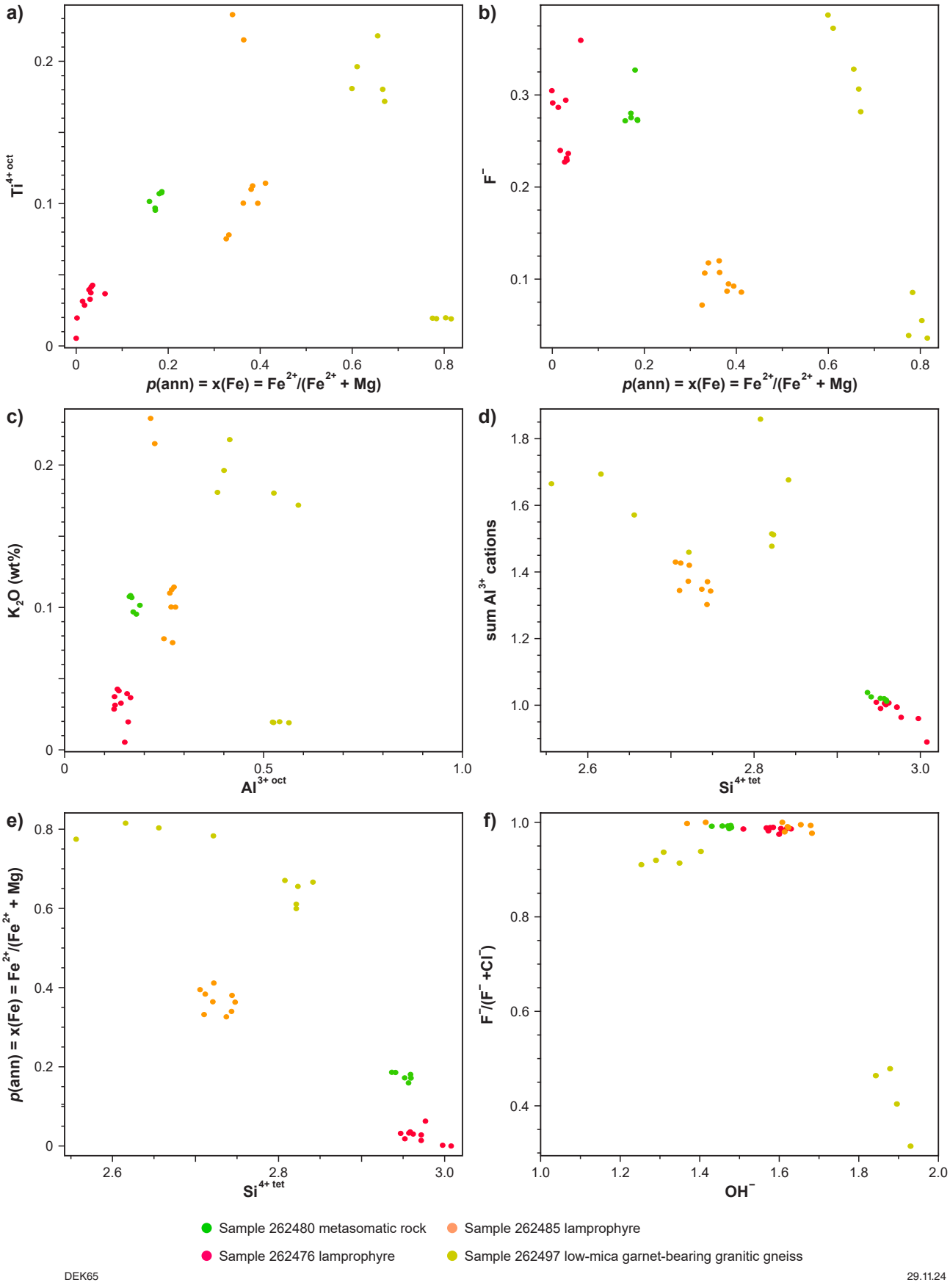

Figure 9. Chemical composition of biotite from electron probe microanalysis (EPMA) data for drillcore samples from tenement E 80/5169

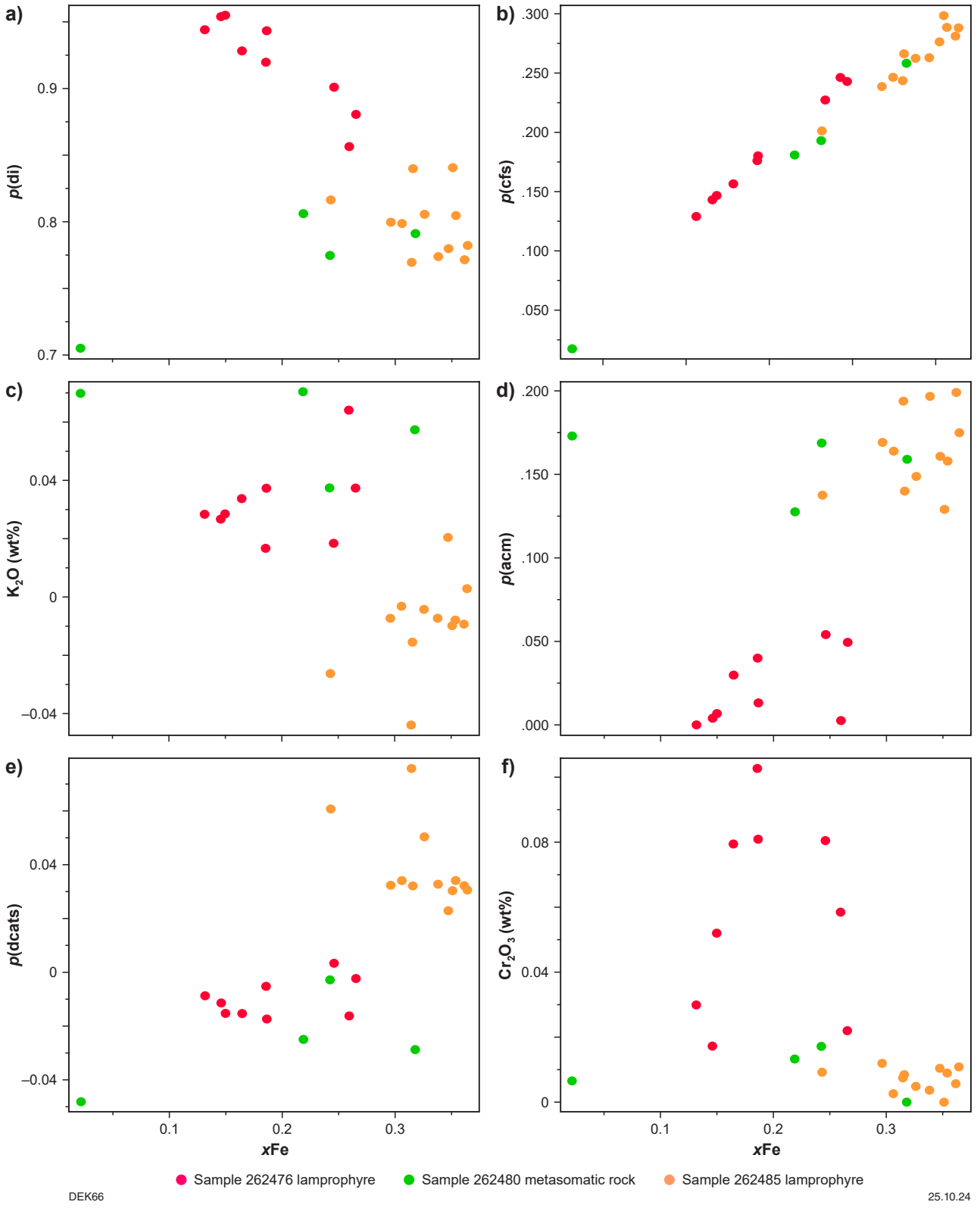

Figure 10. Chemical composition of clinopyroxene from electron probe microanalysis (EPMA) data for drillcore samples from tenement E 80/5169

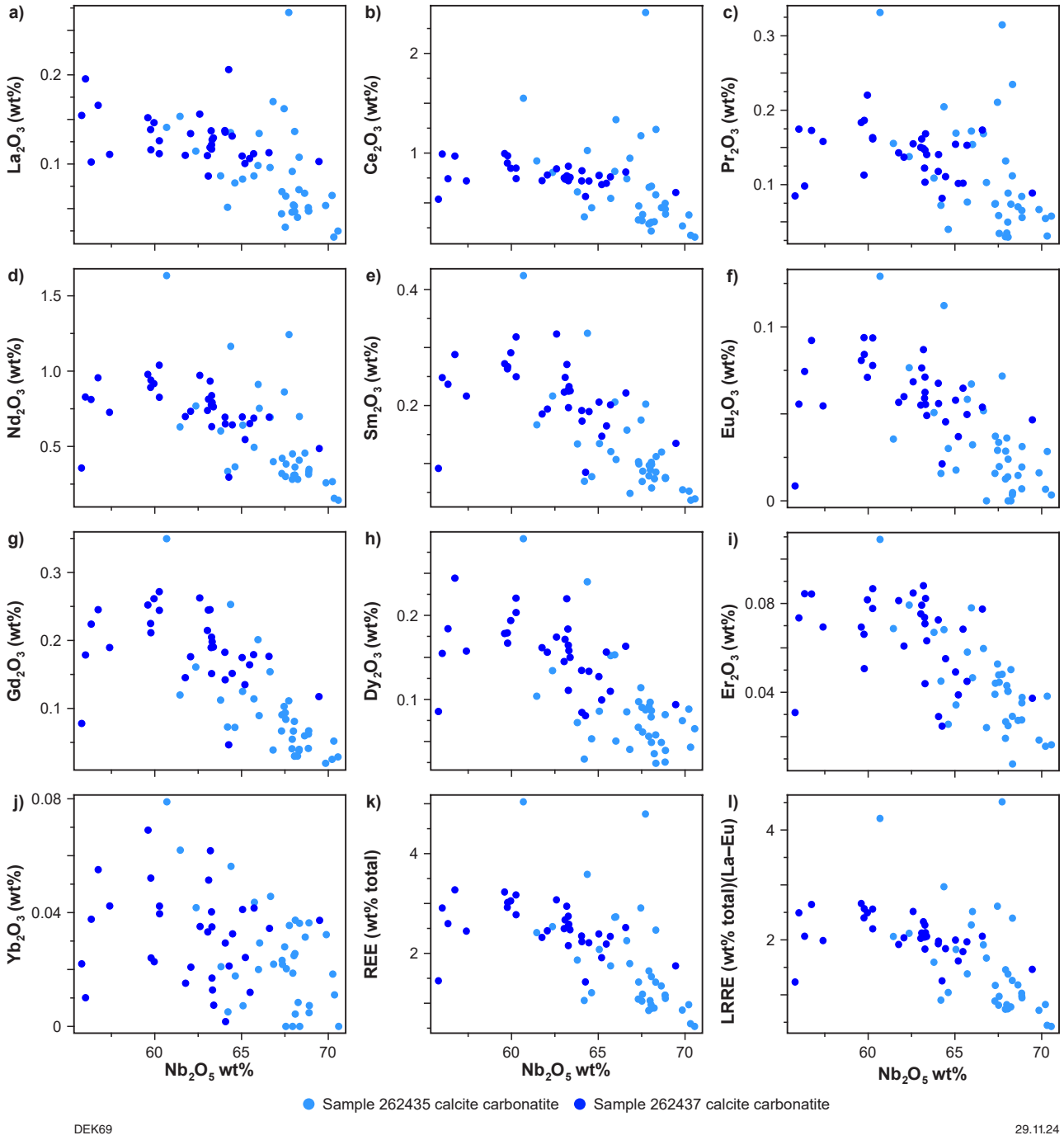

Figure 11. Rare earth element (REE) composition of pyrochlore from electron probe microanalysis (EPMA) data for drillcore samples from tenement E 80/5169

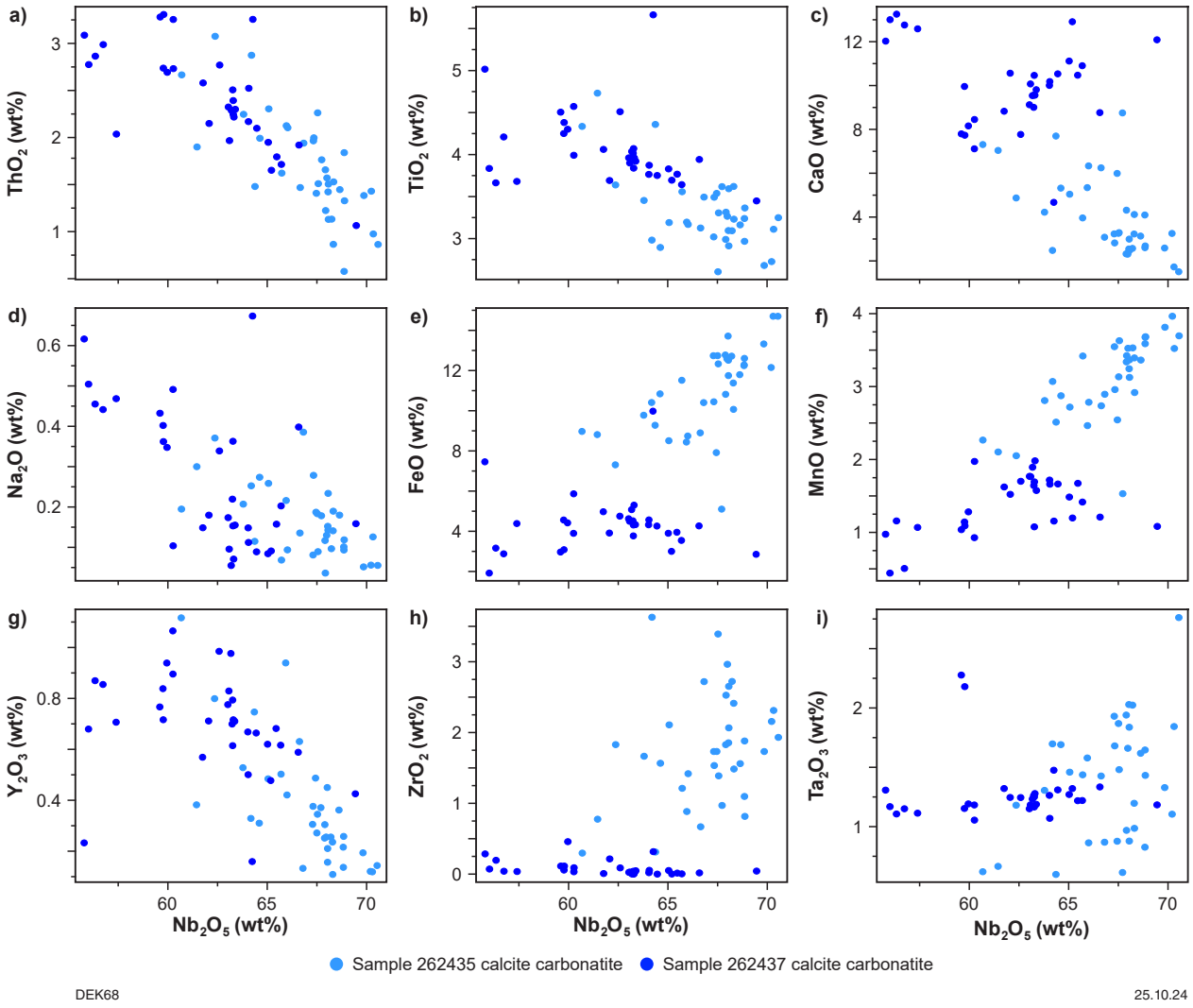

Figure 12. Non-REE composition of pyrochlore from electron probe microanalysis (EPMA) data for drillcore samples from tenement E 80/5169

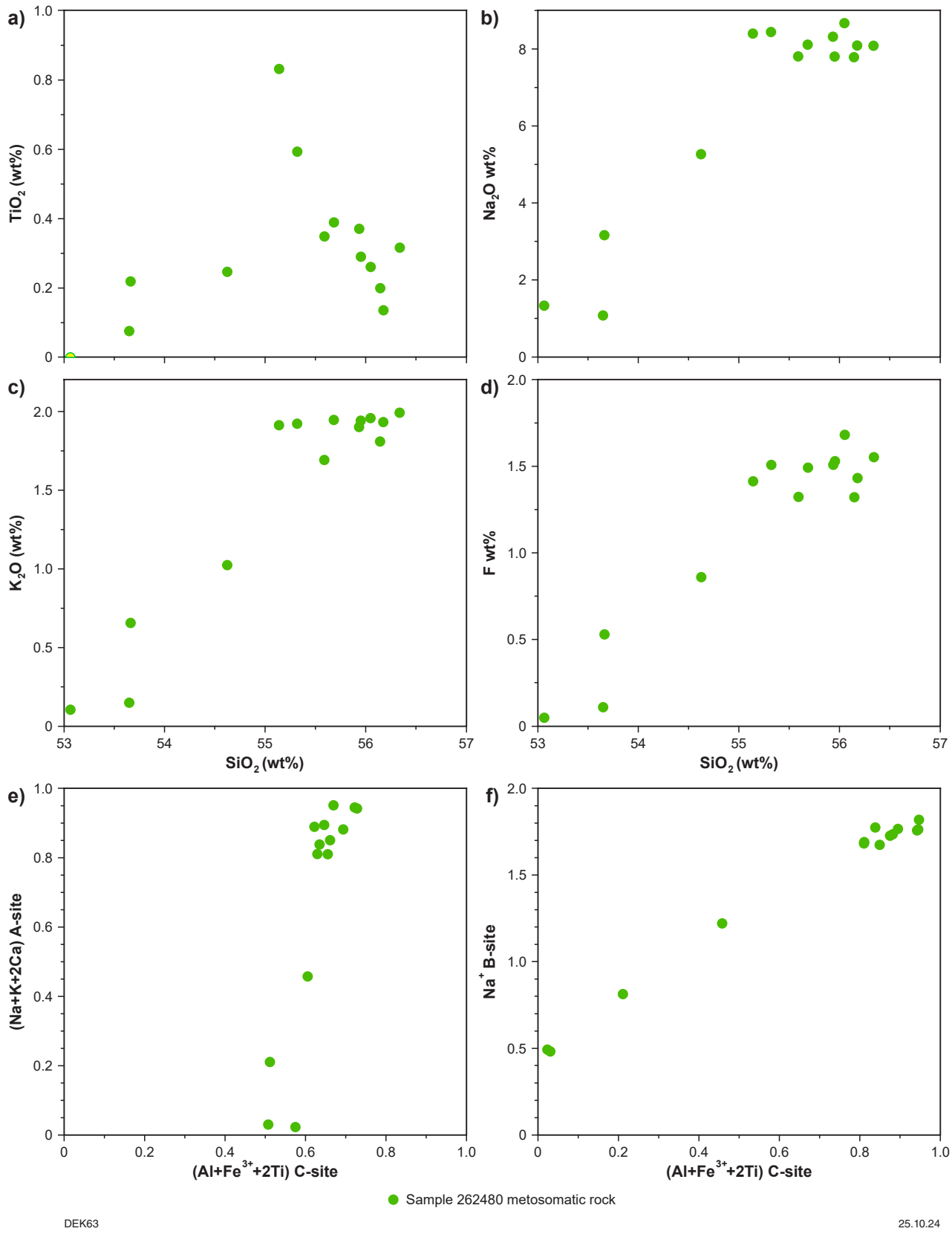

Figure 13. Chemical composition of amphibole from electron probe microanalysis (EPMA) data for drillcore samples from tenement E 80/5169

Geochronology

Geochronology of eight drillcore samples was conducted to constrain the magmatic crystallization ages of the various host and intrusive rocks, and to constrain the ages of metamorphism or alteration and maximum ages of deposition of basement rocks. U–Pb zircon analyses of seven samples are published as GSWA Geochronology Records (available from GeoVIEW) and the reader is referred to those for detailed information, although a brief summary is provided below (for clarity, most citations for this section are listed in Table 2). Apatite U–Pb and Lu–Hf geochronology results are presented below. A summary of dated samples, techniques and results is provided briefly below, as well as in Figure 14 and Table 2. The depth locations of samples within the drillcores are shown in Figure 2.

Table 2. Summary of geochronology of drillcore samples in this study from tenement E 80/5169

GSWA Sample ID	*Drillhole ID*	*Lithology*	*Technique*	*Mineral analysed*	*Age of detrital/ xenocrystic components (Ma)*	*Age of igneous crystallization (Ma)*	*Age of metamorphism (Ma)*	*Comments*	*Reference*
262435	EAL001ext	Calcite carbonatite	U–Pb	zircon	2187 ± 9 (1σ), 1873 ± 11 (1σ), 1826 ± 14 (1σ), 1805 ± 13 (1σ), 1770 ± 16 (MSWD = 0.63, n = 3), 1718 ± 15 (MSWD = 1.7, n = 10)	NA	NA	Maximum crystallization age of c. 1718 Ma	(Wingate et al., 2024g)
262435	EAL001ext	Calcite carbonatite	U–Pb	apatite	NA	NA	NA	Dominated by common Pb. Did not yield an isochron	
262435	EAL001ext	Calcite carbonatite	Lu–Hf	apatite	688 ± 47 (MSWD = 1.5, n = 10)	NA	NA	80 µm spot	
262447	EAL001ext	Monzogranite gneiss (chlorite-bearing)	U–Pb	zircon	NA	1774 ± 11 (MSWD = 0.88, n = 7)	NA		(Wingate et al., 2024h)
262456	EAL002	Lamprophyre	U–Pb	apatite	863 ± 19 (MSWD = 1.3, n = 27)	NA	NA	Maximum crystallization age of c. 863 Ma	
262456	EAL002	Lamprophyre	Lu–Hf	apatite	NA	NA	NA	Apatite too small to analyse with 80 µm spot	
262471	EAL002	Biotite–garnet–orthophyroxene-bearing granitic gneiss	U–Pb	zircon	NA	1767 ± 13 (MSWD = 1.2, n = 6)	1593 ± 6 (MSWD = 1.1, n = 10)		(Wingate et al., 2024i)
262476	EAL005	Lamprophyre	U–Pb	zircon	2674 to 684 (n = 15) 799 ± 7 (MSWD = 0.27, n = 5 692 ± 9 (MSWD = 1.2, n = 3)	NA	NA	Maximum crystallization age of c. 692 Ma	(Wingate et al., 2024a)
262503	EAL006	Low-mica garnet-bearing monzogranite gneiss	U–Pb	zircon	NA	1608 ± 4 (MSWD = 1.7, n = 16)	1575 ± 11 (MSWD = 3.7, n = 3)		(Wingate et al., 2024c)
262515	EAL006	High-Zr leucogranitic gneiss	U–Pb	zircon	2322 ± 9 (1σ) 1870 ± 13 (1σ)	1776 ± 9 (MSWD = 1.9, n = 10)	1591 ± 6 (MSWD = 1.0, n = 7)		(Wingate et al., 2024d)
262550	EAL006	Garnet–sillimanite pelitic migmatite	U–Pb	zircon	1699 ± 19 (MSWD = 2.0, n = 8)	NA	1594 ± 14 (MSWD = 1.6, n = 4)		(Wingate et al., 2024e)

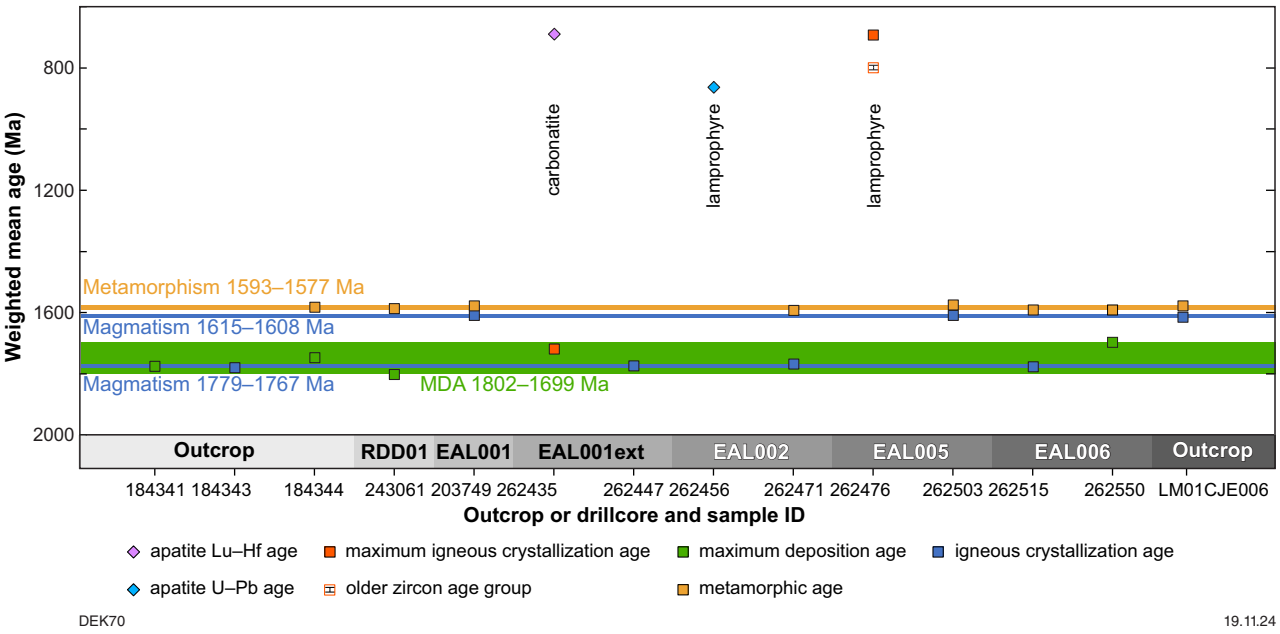

Figure 14. Summary of new and existing geochronology data from the high-intensity magnetic belt in the northern Aileron Province. Zircon data are weighted mean ages with 95% confidence intervals, and error bars for all are smaller than the symbol size. Apatite data include an inverse isochron date (Lu–Hf) and lower intercept date (U–Pb). Red symbols denote the weighted mean age of the youngest group of zircon analyses, interpreted to be xenocrystic. The red outline symbol with an internal error bar is the weighted mean age of a second group of zircon analyses in sample 262476. Blue, orange and green shading denote the ages for two intervals of magmatism, one interval of metamorphism and the interval spanned by maximum deposition ages (MDA). Existing sample data is presented for samples GSWA 184341 (Kirkland et al., 2009), 184343 (Wingate et al, 2024f), 184344 (Wingate et al., 2024b), 243061 (Wingate et al., 2022b), 203749 (Wingate et al., 2022a) and LM01CJE006 (Kositcin et al., 2014)

U–Pb zircon geochronology

Zircon geochronology by sensitive high-resolution ion microprobe (SHRIMP) was conducted on four samples of granitic gneiss, as well as one sample each of carbonatite, lamprophyre and pelitic migmatite. Granitic gneiss samples yielded two distinct ages for granitic protolith crystallization (Fig. 14; details and references in Table 2). High-Zr chlorite-bearing, garnet–orthopyroxene-bearing and leucogranitic high-Zr samples indicated ages of 1776–1767 Ma (GSWA 262447, 262471, 262515) and low-mica garnet-bearing granitic gneiss provided an age of 1608 ± 4 Ma (GSWA 262503). Analyses of high-U zircon rims in granitic gneiss samples indicate ages for metamorphism of 1593–1575 Ma (GSWA 262471, 262503, 262515; Fig. 14). The pelitic migmatite sample provided a conservative maximum age of deposition of 1699 ± 19 Ma and an age for metamorphism of 1594 ± 14 Ma (GSWA 262550).

Fifteen analyses of zircons from lamprophyre sample GSWA 262476 yielded dates of 2674–684 Ma, including two age components at c. 799 and 692 Ma (Fig. 15a; Table 2). Subhedral zircons with well-developed oscillatory zoning, including some metamict zones, and variable Th/U ratios (0.53 – 2.73) yielded the older result of 799 ± 7 Ma (n = 5, MSWD = 0.27). Larger anhedral, strongly rounded zircons (Fig. 15b) with bright oscillatory zoning (Fig. 15a) and Th/U ratios of 0.57 – 0.63 provided a mean age of 692 ± 9 Ma (n = 3, MSWD = 1.2). However, two other visually similar large, rounded zircon grains (Fig. 15b) yielded older dates (1σ) of 1190 ± 53 Ma (Th/U = 0.84) and 930 ± 14 Ma (Th/U = 0.06), and do not indicate a simple correlation between apparent age and zircon grain size and morphology. Zircons from carbonatite sample GSWA 262435 (Table 2) yielded dates at c. 2187, 1873, 1826, 1805, 1770 ± 16 Ma (MSWD = 0.63, n = 3) and 1718 ± 15 Ma (MSWD = 1.7, n = 10) (Wingate et al., 2024g). The potential geological significance of dates from lamprophyre and carbonatite are discussed later.

For comparison to the above data, Figure 14 additionally shows existing dates from other samples of basement rocks within the high-intensity magnetic belt in the northern Aileron Province, that were summarized in the *Location and geological background* section above (samples GSWA 184341, Kirkland et al., 2009; GSWA 203749, Wingate et al., 2022a; GSWA 243061, Wingate et al., 2022b; LM01CJE006, Kositcin et al., 2014). These previous determinations provide comparable constraints for the ages of magmatism and metamorphism and provide additional data for the maximum ages of deposition of metasedimentary rocks in the belt (Lake Mackay Quartzite and unnamed Fe-rich packages).

U–Pb and Lu–Hf apatite geochronology

Apatite U–Pb and Lu–Hf geochronology had mixed success in determining primary ages (Table 2; Appendices 4, 5). For carbonatite (GSWA 262435), the U–Pb method did not yield a date from apatite as all analyses are dominated by high common Pb (Fig. 16a), and Lu–Hf yielded a poorly defined inverse isochron date of 688 ± 47 Ma (MSWD = 1.5) from 10 analyses. This date was determined by anchoring the isochron to an average crustal initial $^{177}Hf/^{176}Hf$ ratio of 3.55 ± 0.03 (Fig. 16b). Although 50 Lu–Hf analyses were collected in total, 40 indicated no radiogenic Hf. For lamprophyre (GSWA 262456), U–Pb in apatite yielded a lower intercept date of 863 ± 19 Ma (MSWD = 1.3) from 27 analyses with an initial $^{207}Pb/^{206}Pb_0$ ratio of 0.873 ± 0.017 (Fig. 16c), whereas the grains were too small for the 80 µm laser spot size required for Lu–Hf analysis.

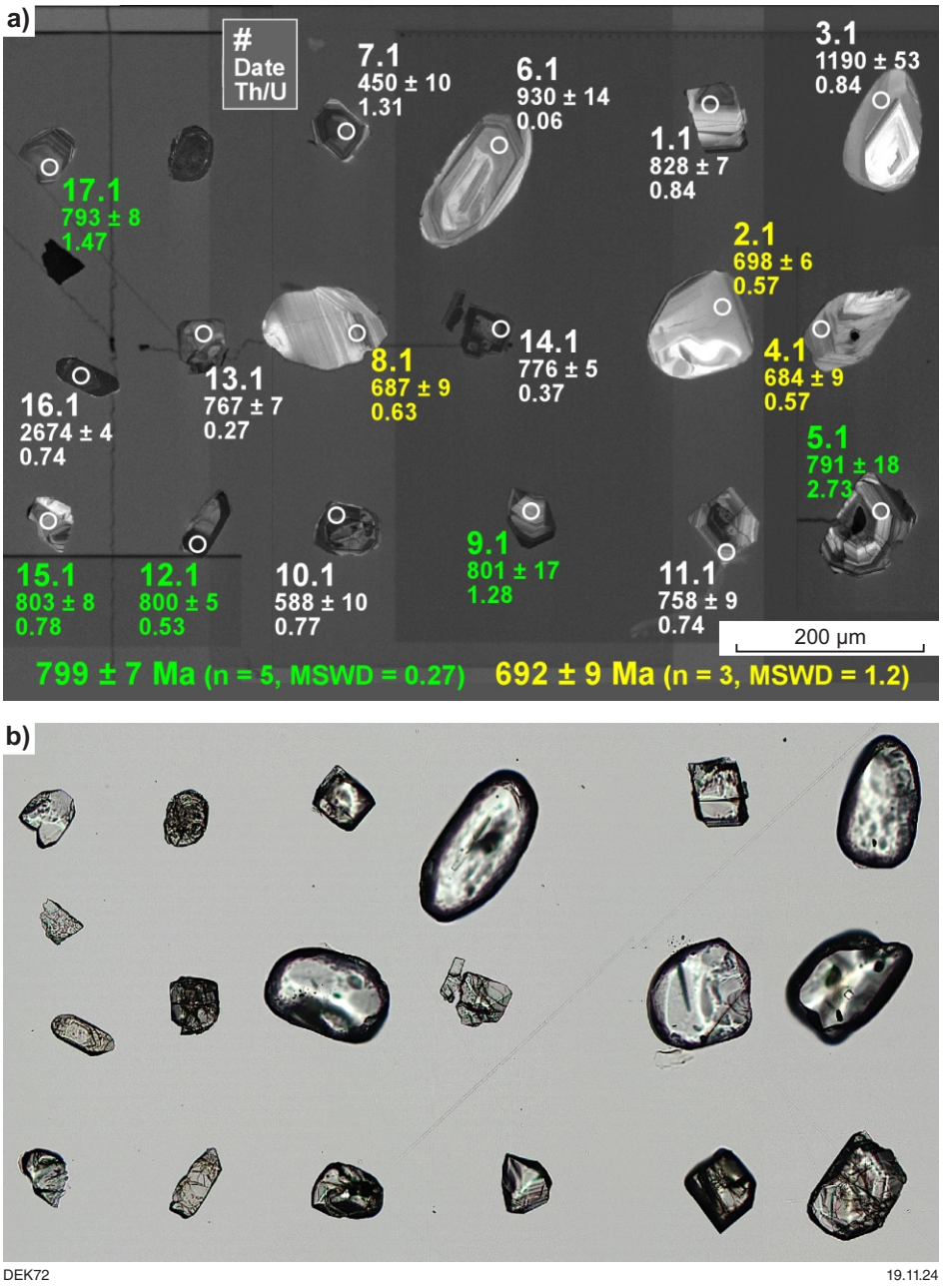

Figure 15. Annotated cathodoluminescence (CL) image (a) and transmitted-light image (b) of all zircons from sample 262476: lamprophyre dyke, Crean prospect. Numbered circles in (a) indicate the locations of analysis sites. All dates (in Ma) are based on 207-corrected $^{238}U/^{206}Pb$ ratios, except for analysis 16.1, for which the date is based on its 204-corrected $^{207}Pb/^{206}Pb$ ratio. Uncertainties in individual dates are 1σ. Weighted mean dates for age components are 95% confidence intervals; MSWD = mean square of weighted deviates.

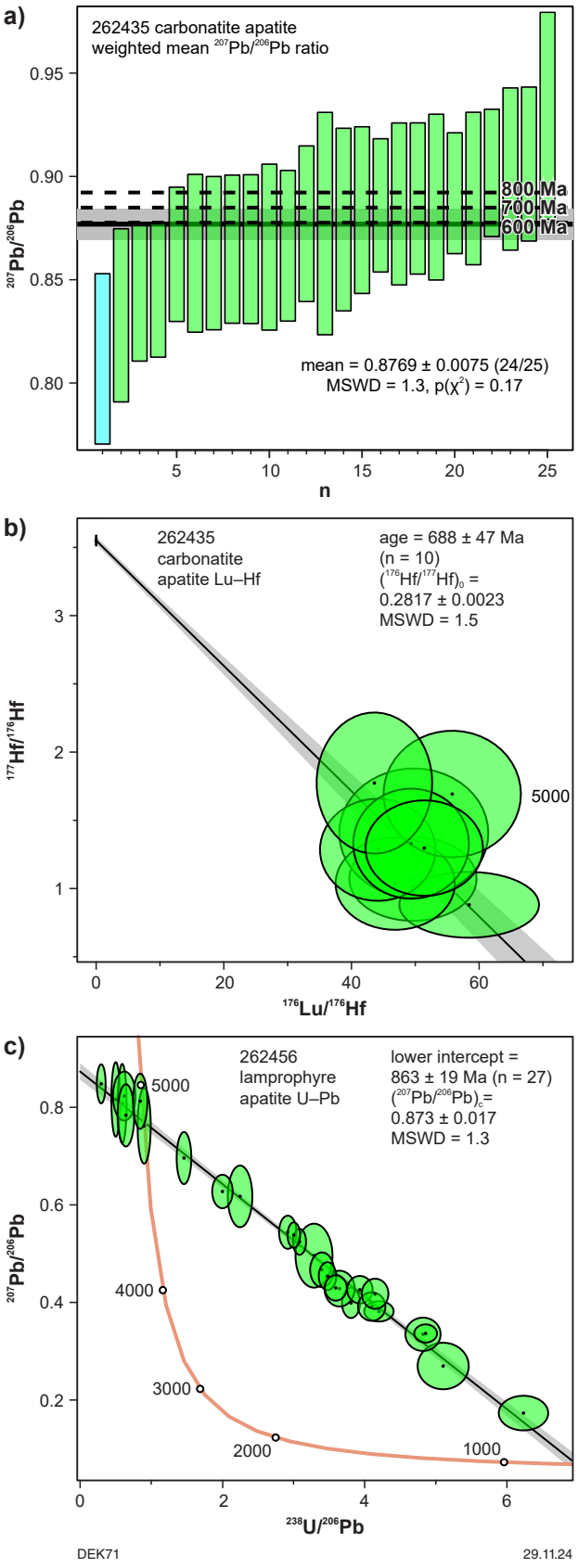

Figure 16. Analytical data from apatite: a) weighted mean $^{207}Pb/^{206}Pb$ data for low-U analyses of calcite carbonatite sample GSWA 262435, with initial $^{207}Pb/^{206}Pb$ crustal values calculated at 800 Ma (= 0.892569), 700 Ma (= 0.884783) and 600 Ma (= 0.877198) Ma using the Stacey and Kramers (1975) model; b) Lu–Hf data for calcite carbonatite sample GSWA 262435 presented as an inverse isochron anchored to an initial $^{177}Hf/^{176}Hf$ ratio of 3.55 ± 0.03; c) U–Pb Tera–Wasserburg diagram showing common-Pb mixing line and lower concordia intercept for lamprophyre dyke sample GSWA 262456

Whole-rock Nd–Sr–Hf isotopes

Whole-rock Sr, Nd and Hf compositions for carbonatite, lamprophyre and hornblende metagabbronorite are provided in Appendix 2. Using an assumed igneous crystallization age of c. 800 Ma for lamprophyres (see the *Discussion* section below), they are characterized by positive εNd(i) (+3.3 to +4.6) and εHf(i) (+5.6 to +7.2), with unradiogenic $^{87}Sr/^{86}Sr(i)$ between 0.70359 and 0.70494 (Fig. 17a). Covariance in εNd(i) and εHf(i) were similar and, for carbonatite and lamprophyre, contain values comparable to ocean-island basalt (OIB), Group I global kimberlites and aillikites reported by Sudholz et al. (2023).

Assuming an igneous crystallization age of 800 Ma, carbonatites are characterized by positive εNd(i) (+2.3 to +3.4) and εHf(i) (+3.4 to +7.7), with unradiogenic $^{87}Sr/^{86}Sr(i)$ varying between +0.70326 to +0.70674 (Fig. 17b). Two of the samples, GSWA 262560 and 262561 (both from EAL008) have very high $^{176}Lu/^{177}Hf$ ratios of 0.1476 and 0.2597, respectively. The other two samples, GSWA 262435 and 262436, have $^{176}Lu/^{177}Hf$ ratios that are lower, 0.0598 and 0.0730, respectively, but are still elevated compared to chondrite (0.0336). A quasilinear, covariant εNd(i)–εHf(i) array is not defined by the four carbonatite samples (Fig. 17b). Two of the four samples very closely approximate the εNd(i) and εHf(i) compositions of lamprophyres sampled here, as well as aillikites reported by Sudholz et al. (2023); whereas, the other two have an appreciably less radiogenic Hf signature. Two carbonatite samples with most radiogenic $^{87}Sr/^{86}Sr(i)$ signatures (+0.70571 and +0.70674) plot along one of the 'limbs' of the compiled global data for Phanerozoic carbonatites in (Precambrian) shields (Fig. 17a; see Yaxley et al., 2022).

Hf isotope data for the metagabbroic rocks are calculated with an assumed age of 1775 Ma, giving εNd of −0.9 to +1.0 (not plotted). However, as their magmatic age is unknown in detail, the age and corresponding εNd values should be taken as indicative only. Due to the intensity of deformation, the original intrusive relationships between the protoliths to metagabbroic and metagranitic rocks are obscured in these drillcores. The possible igneous crystallization ages for the metagabbroic rocks range from about 1800 Ma (potential age of the Dufaur Suite; Scrimgeour, 2013a), to 1770 Ma (Carrington Suite), to about 1640–1630 Ma (Andrew Young Complex; Claoué-Long and Hoatson, 2005; Cross et al., 2005b). Dufaur Suite or Andrew Young Complex equivalents are unlikely as the known εNd_T data for the Dufaur suite is +4.7 (presumably at 1800 Ma), and for the Andrew Young Complex is εNd_{1633} = −4.64 and −4.84 (Hoatson et al., 2005), all of which are more radiogenic than our data. An age similar to the magmatic age of c. 1615 Ma for felsic rocks is unlikely for the metagabbroic rocks as this age has not been proposed as a mafic igneous timeline; but not impossible, because the conservative minimum age constraint is the age of regional metamorphism at c. 1595 Ma. Regardless of the exact age, the depleted mantle model ages for the metagabbroic rocks suggest either extraction at about 2300–2200 Ma, which is consistent with the known North Australian Craton isotope array (e.g. see Lu et al., 2022), or mixing of a mantle-derived melt with a source that is considerably older than 2300 Ma.

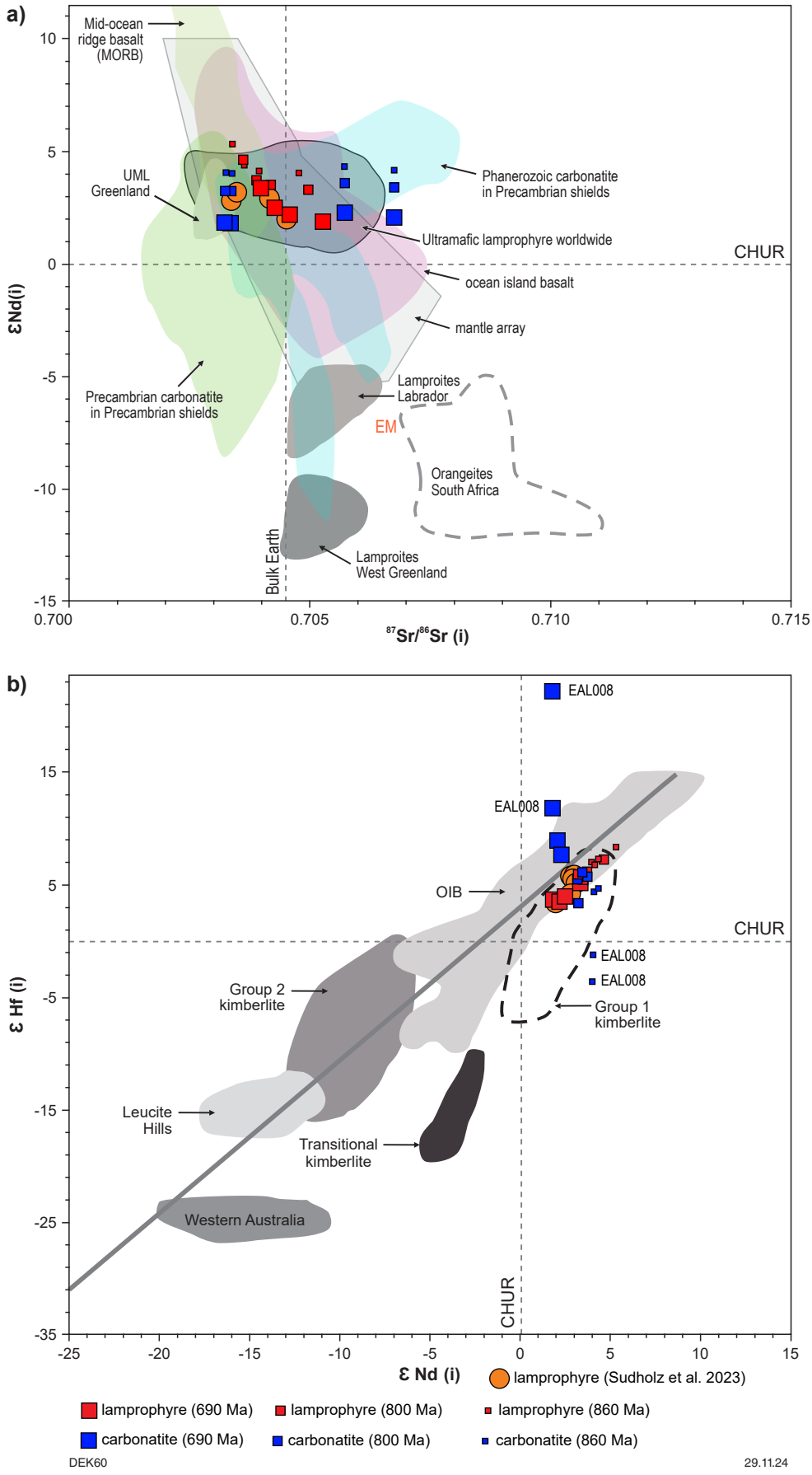

Figure 17. Whole-rock isotope data plots, adapted from Sudholz et al. (2023) and Yaxley et al. (2022): a) εNd(i) versus $^{87}Sr/^{86}Sr(i)$; b) εHf(i) versus εNd(i)

Discussion

Aileron Province gneisses

The lithologies described from the drillcores in this study show strong alteration or metasomatism in many instances, but based on integration of visual (textural), geochemistry, mineralogy and geochronology information, the protoliths are readily determined and dominated by felsic metaigneous rocks, with less common metasedimentary rocks. Metamafic rocks (metagabbronorite) form up to 20% of some drillcore intersections, although the original intrusive relationships between granitic and mafic gneisses are not preserved due to intense deformation. The youngest metagranitic rocks of this study – the 1615–1608 Ma low-mica garnet-bearing granitic gneiss – are not intruded by or interlayered with metagabbronoritic rocks. This suggests that the protolith age for metagabbronorite is older than c. 1615 Ma. Metasedimentary rocks are comparatively rare in the studied drillcores, being most abundant in EAL006, which contains stromatic garnet–sillimanite ± cordierite-bearing migmatite. The maximum deposition age for pelitic migmatitic sample GSWA 262550 from EAL006 is too young for it to be part of the 1858–1799 Ma Lander Rock Formation, and instead is more consistent with existing age constraints from the Lake Mackay Quartzite and unnamed Fe-rich metasedimentary packages.

The ages reported here for magmatic crystallization of felsic igneous protoliths and for metamorphism are consistent with known timeframes for the Aileron Province in the Paleoproterozoic and early Mesoproterozoic, respectively (e.g. Hollis et al., 2013; Scrimgeour, 2013a; Kositcin et al., 2014). In detail, it remains unclear how the lithologies of this belt and their ages differ from the lower intensity magnetic rocks to the north and south (Fig. 1). However, on the basis of new and existing data, the 1858–1799 Ma Lander Rock Formation has not been identified within the high-intensity magnetic belt, and the metasedimentary samples dated from this belt have maximum depositional ages that are younger than those for the Lander Rock Formation and possibly the Reynolds Range Group (Kirkland et al., 2009; Hollis et al., 2013; Wingate et al., 2022b; Wingate et al., 2024e). The Lake Mackay Quartzite is so far the only formally recognized (meta)sedimentary unit from within this belt. However, it remains unclear whether highly magnetic metasedimentary rocks that have previously been documented (Wingate et al., 2022b; Wray, 2023) and metamorphosed banded iron-formation and pelitic gneiss reported here (e.g. dated sample GSWA 262550, Wingate et al., 2024e), are part of the Lake Mackay Quartzite or represent a different lithostratigraphic unit. In terms of felsic igneous rocks, (meta)granitic rocks with protolith crystallization ages of c. 1780 to 1767 Ma, consistent with those of the Carrington Suite, occur in this belt (samples GSWA 184343, 262447, 262471, 262515; (Wingate et al., 2024d, 2024f, 2024h, 2024i), as well as a younger suite at 1615 to 1608 Ma (Wingate et al., 2022a; Wingate et al., 2024c) with Fe-rich garnet and F-rich biotite (Figs 7, 9) that includes the Rapide Granite (Kositcin et al., 2014).

Synthesizing the above information leads us to speculate that the high-intensity magnetic belt in the northern Aileron Province could represent a late Paleoproterozoic–early Mesoproterozoic rift developed in crust that included 1780–1767 Ma granitic rocks (and perhaps gabbronoritic rocks). In this model, both Fe-rich and quartz-rich sediments (becoming the Lake Mackay Quartzite) were deposited into basins during rifting, followed by intrusion of 1615–1608 Ma felsic (and mafic?) magmas. Most sedimentation likely post-dated 1780–1767 Ma magmatism based on the dates of detrital zircons in metasedimentary samples (cf. sample GSWA 243061, Wingate et al., 2022b), but it remains uncertain how closely sedimentation followed this magmatism.

The studied gneissic rocks were metamorphosed, involving partial melting, up to about 30 Ma after 1615–1608 Ma magmatism, as metamorphic ages from zircon rims yield ages of c. 1594 to 1577 Ma (Fig. 14). At a broader scale, 1615–1608 Ma ages for felsic magmatism are similar to those documented within the Lasseter Shear Zone that probably defines the western margin of the Aileron Province and North Australian Craton (Kelsey et al., 2022b; Martin et al., 2022). In addition, similar-age magmatism is manifest as unnamed c. 1620 Ma granitic rocks in the Ennugan Mountains in the central Aileron Province in the Northern Territory (Kositcin et al., 2013; Scrimgeour, 2013a; Beyer, 2017) and 1615–1600 Ma magmatism within the eastern Haasts Bluff Domain of the Warumpi Province (Zhao and Bennett, 1995; Scrimgeour, 2013b). The 1594– 1575 Ma age range for metamorphism overlaps with the known age range of metamorphism during the 1595–1520 Ma Chewings Orogeny recorded about 400 km farther east in the Aileron Province (see Alessio et al., 2020), and is younger than the 1624–1604 Ma age range for metamorphism reported from the Top Up Rise prospect about 100 km to the southwest at the interpreted western margin of the Aileron Province (Kelsey et al., 2022b).

The age of the proposed rift is uncertain. However, given felsic magmatism occurred at c. 1615 to 1608 Ma, and granitic rocks of this age are essentially restricted to the high-intensity magnetic belt, rifting and sedimentation could have occurred in the close lead-up to, or during, this timeframe. The existing maximum depositional age constraints from the few samples of metasedimentary rocks from this belt do not tightly constrain the age of deposition: the maximum depositional age is 1802 ± 7 Ma for sample GSWA 243061 (Wingate et al., 2022b); 1775 ± 7 Ma for sample GSWA 184341 (Kirkland et al., 2009; Hollis et al., 2013); 1745 ± 10 Ma for sample GSWA 184344 (Wingate et al., 2024b); and 1699 ± 19 Ma for sample GSWA 262550 (Wingate et al., 2024e). Nevertheless, this raises the possibility – speculative at this stage – that at least some sedimentation into the proposed rift was synchronous with either (or multiple) of: (a) the 1640–1630 Ma Liebig Event, or the lead-up to it, which has recently been reinterpreted as extension related rather than convergent (March et al., 2024), or (b) likely extension-related tectonism at c. 1690 Ma (Argilke Event; Hollis et al., 2013; March et al., 2024), or (c) 1615–1608 Ma magmatism. Both the Liebig and Argilke events are related to activity along and south of the Central Australian Suture (the boundary between Aileron and Warumpi Provinces), which is oriented quasi-parallel to the high-intensity magnetic belt of the northern Aileron Province and is, thus, in a favourable orientation for distal but contemporaneous extension. From the studied drillcores there is no evidence as to the relative timing relationship between sedimentation and emplacement of the granitic protolith to the low-mica garnet-bearing granitic gneiss.

Lamprophyre and carbonatite

The gneissic rocks described above have been intruded by lamprophyre (aillikite) dykes, which are not deformed and preserve clear crosscutting relationships with the host gneisses (Fig. 4). The intrusive relationship/s for carbonatite are less clear as carbonatite is strongly layered, but on the basis of geochronology presented above likely intrudes and, therefore, crosscuts the host gneisses.

Intersection of carbonatites (and lamprophyre) in these and other drillcores in the northern Aileron Province has generated high exploration interest (e.g. Encounter Resources Ltd, 2023, 2024; WA1 Resources Ltd, 2022, 2023) due to the elevated Nb and REE contents in these rocks (e.g. Figs 6b,e, 8, 11, 12). An important aspect of understanding the geological environment in which these rocks were generated is to constrain their age. Geochronology was collected in this study from carbonatite and lamprophyre using U–Pb and Lu–Hf isotope techniques on zircon and apatite. Interpretation of the age data is complex, as numerous possibilities arise to explain the data, and there are external constraints to consider as well.

Lamprophyre

Geochronology of two samples of lamprophyre yielded 863 ± 19 Ma (U–Pb apatite, n = 27), 799 ± 7 Ma (U–Pb zircon, n = 5) and 692 ± 9 Ma (U–Pb zircon, n= 3). Interpretation of this age data is complex. First, the process by which crystallization of magmatic zircon in lamprophyre occurs remains enigmatic, particularly as low whole-rock SiO_2 wt% contents do not promote zircon crystallization in ultramafic magma. Nevertheless, zircon in lamprophyre is commonly considered to reflect growth in the mantle rather than represent xenocrystic crustal zircons or crystallization during emplacement (Griffin et al., 2000; Page et al., 2007; Sun et al., 2018). Hence all zircons may be inherited from older rocks. This could mean both the 799 ± 7 Ma and 692 ± 9 Ma dates reflect xenocrystic components in lamprophyre. In this scenario, no zircon in this sample reflects the magmatic age of the lamprophyre.

In more detail, the physical characteristics of zircons from the two age groups add to the complexity. There is an almost bimodal zircon shape and size distribution. First, the younger large, ovoid-to-rounded zircons with well-defined oscillatory and sector zoning and bright cathodoluminescence (CL) response. The rounded exteriors of the grains truncate oscillatory zoning, implying a process subsequent to their crystallization. Second, and more common, older, smaller subhedral to euhedral zircons with well-defined straight crystal faces and square or prism shapes (Fig. 15; Wingate et al., 2024a). These smaller zircons typically have a darker CL response and many feature internal oscillatory or sector zoning (Fig. 15; Wingate et al., 2024a). There is no clear relationship between physical morphology of zircons and age. However, there is some correlation of zircon Th/U with age. Analyses defining the 799 ± 7 Ma date typically have very variable Th/U ratios (median 1.28 for a total range of 0.53 – 2.73 range, n = 5) and there are no large, ovoid/rounded zircons in this group. In contrast, the three analyses that yield the 692 ± 9 Ma date have lower Th/U ratios (median 0.57 for a total range of 0.57 – 0.63, n = 3). Although this group is defined by analyses from large, rounded zircons, this age is not exclusive to such grains, as older dates were obtained from other zircons with similar morphology (Fig. 15). The rounded nature of the larger zircons is suggestive of abrasion or partial resorption, implying that they are xenocrystic. Although Belousova et al. (1998) report that rounded and subrounded zircons are common in kimberlite, the origin of those zircons (magmatic versus xenocrystic) is unclear from their study.

Based on these considerations, there are three possibilities for interpretation of the U–Pb zircon data for sample GSWA 262476:

- First, the age component at 799 ± 7 Ma could reflect magmatic crystallization and emplacement. For the reasons outlined above involving the enigmatic origin of zircon in ultramafic magma and the physical characteristics, this possibility remains unclear. The comparable perovskite common-Pb isochron date of 806 ± 22 Ma reported by Sudholz et al. (2023) from aillikite lamprophyre located about 60 km south of our study area is circumstantially in support of this date reflecting magmatic crystallization. Nevertheless, there is no necessity that lamprophyre in our study is the same age as those from Sudholz et al. (2023), even if they are geochemically similar. If our date of 799 ± 7 Ma does reflect the magmatic crystallization age, it would imply that the younger age component at c. 692 Ma reflects enigmatic (fluid-related?) modification of zircon. Although based on only three analyses, the narrow range of Th/U ratios, as well as the U–Pb apatite data from lamprophyre, discussed below, does not support this interpretation for the younger age component.

- Second, the younger age component at 692 ± 9 Ma instead reflects the magmatic crystallization age of emplacement. This date is based entirely on analyses of three large, ovoid, rounded grains with a median Th/U ratio of 0.57. The comparable Lu–Hf apatite age of 688 ± 47 Ma, discussed below, lends support for magmatic or fluid activity at this time, but not unequivocal support for either. As lamprophyre is altered – most obviously olivine – it raises the question of the age of this alteration. Thus, it remains possible that the c. 692Ma age reflects an alteration event. Such an event could produce loss of radiogenic Pb in zircons.

- Third, neither of the above two dates from lamprophyre reflect the age of magmatic crystallization during emplacement. In this scenario, all zircon in lamprophyre is xenocrystic and the emplacement age must be younger than c. 692 Ma. Support for xenocrystic zircon could be argued based on the contrasting and varying grain morphologies, CL responses and Th/U ratios among the dataset, as well as the SiO_2-undersaturated nature of ultramafic melts that inhibit zircon crystallization. The potential source of these (xenocrystic) zircons is discussed in more detail in the *Regional correlations and mantle source region* subsection below. The main, admittedly circumstantial, constraint on the minimum age for lamprophyre is likely provided by the 635–509 Ma Angas Hills Formation (Haines and Allen, 2019). In the area proximal to the Sudholz et al. (2023) study area (farther south in the Aileron Province), lamprophyre intrudes dolomitic sedimentary rocks considered to be part of the Bitter Springs Group but does not intrude the unconformably overlying Angas Hills Formation (Spaggiari et al., 2016;

van Raalte, 2023; pers. comm. Peter Haines, 2023). The Angas Hills Formation is not known to outcrop in the northern Aileron Province; however, *if* these wider stratigraphic constraints apply in our study region, the emplacement age of lamprophyre is constrained to between about 690 and 635 Ma.

U–Pb apatite data from another lamprophyre sample (GSWA 262456) yielded 863 ± 19 Ma (n = 27; Fig. 16c), which is significantly older than the older zircon date of 799 ± 7 Ma for sample GSWA 262476 above, and introduces further uncertainty into the interpretation of age data. Textural information from apatite does not resolve whether apatite is xenocrystic, but following the logical options discussed above for zircon, it is possible. However, if apatite in lamprophyre GSWA 262456 is xenocrystic, it is from a single coherent population (Fig. 16c), and there is no (clear) evidence for younger modification (or crystallization), such as at c. 800 Ma and c. 690 Ma as seen in zircon. Unfortunately, the combination of U–Pb zircon and apatite data from the two lamprophyre samples dated in this study do not definitively establish its magmatic emplacement age, it therefore remains an open question. Moreover, whole-rock geochemical data (Fig. 6b,c,d,e) offers no distinction between dated samples GSWA 262456 and GSWA 262476 that might explain the difference in apatite versus zircon dates. Isotope data for our lamprophyre samples (Fig. 17) cluster in similar parts of $^{87}Sr/^{86}Sr(i)$–εNd(i) and εNd(i)–εHf(i) space, which does not distinguish whether one of the three dates is more plausible. An additional possibility is that there are at least two generations of lamprophyre emplacement in the study area, with one at c. 860 Ma (or younger) and another at c. 690 Ma (or younger), and a third identified outside the study area – dated by Sudholz et al. (2023) – at c. 800 Ma.

There does appear to be at least three episodes of zircon and apatite crystallization within lamprophyre, over a time frame of about 170 million years during the Neoproterozoic. Our preferred interpretation is that the magmatic age of the dated lamprophyre is Neoproterozoic and younger than c. 690 Ma. If true, lamprophyre investigated here would be at least 100 Ma younger than those dated by Sudholz et al. (2023). However, it remains an open question as to whether there are multiple generations of lamprophyre in the study area. The difference in our data from those of Sudholz et al. (2023) suggest this may be the case.

Carbonatite

An additional key question is whether the magmatic ages of carbonatite and lamprophyre are the same, since carbonatite hosts elevated concentrations of REE and Nb and is thus of exploration and economic interest. Drillcore EAL008 shows evidence of interlayered (possibly unmixed?) carbonatite and lamprophyre. From the data we have obtained, the magmatic crystallization age of the carbonatite is also unclear. U–Pb zircon data from carbonatite defines a maximum crystallization age of c. 1718 Ma (GSWA 262435), as all analyzed zircons are Paleoproterozoic. If lamprophyre and carbonatite are similar in age (i.e. Neoproterozoic), the fabric in carbonatite is more likely to represent magmatic flow, since the youngest high-grade deformation event to generate gneissic fabric in the northern Aileron Province is c. 1580 Ma. Therefore, c. 1718 Ma zircons in carbonatite are likely to be xenocrystic in origin.

U–Pb apatite data for carbonatite sample GSWA 262435 did not yield a date due to elevated common Pb. However, $^{207}Pb/^{206}Pb$ ratios from analyses with the lowest U help to approximate the initial $^{207}Pb/^{206}Pb$ value for the reservoir from which apatite grew or was modified by, albeit age unconstrained. The low-U data (24 of 47 analyses) yield a weighted mean $^{207}Pb/^{206}Pb$ ratio of 0.8769 ± 0.0075 (Fig. 16a), similar to the average crust $^{207}Pb/^{206}Pb$ ratio of 0.877198 calculated using the Stacey and Kramers (1975) terrestrial Pb evolution model for 600 Ma.

Lu–Hf apatite data from carbonatite sample GSWA 262435 yield a date of 688 ± 47 Ma (based on 10 of 50 analyses). This result is younger than the U–Pb apatite date and one group of U–Pb zircon dates from lamprophyre sample GSWA 262476, but within analytical uncertainty of the 692 ± 9 Ma date from the same lamprophyre dyke. The internal complexity of Lu–Hf zoning (if any) in apatite is not clear for the carbonatite sample. However, only 20% of Lu–Hf apatite analyses were successful, and common Pb content is high, causing the U–Pb dating attempt to be unsuccessful, and suggesting that apatite in the carbonatite may be internally complex and perhaps (strongly?) modified. As such, it is difficult to assess how much significance to assign to the Lu–Hf apatite date. Nevertheless, comparing the Lu–Hf apatite and U–Pb zircon dates from lamprophyre leads to three possibilities:

- First, that the magmatic emplacement age of both carbonatite and lamprophyre could be c. 690 Ma. This scenario is circumstantially supported by the visual observations from drillcore EAL008, in which carbonatite and lamprophyre appear to be interlayered, and contacts between the two are diffuse rather than sharp, suggesting unmixing rather than intrusive relationships. However, this interpretation is complicated for carbonatite given that εHf(i) data define a large vertical spread from +7.7 to +22.2 when calculated at 690 Ma (Fig. 17b, Appendix 2), with the two samples from drillcore EAL008 contributing most to that spread. It is not clear why εHf(i) and εNd(i) become decoupled in carbonatite for an assumed 690 Ma magmatic emplacement age but could suggest that the apatite Lu–Hf date of 688 ± 47 Ma reflects modification or alteration rather than magmatic crystallization.

- Second, and following on from above, the Lu–Hf apatite data do not yield the age for magmatic crystallization of carbonatite but instead yield the age of a different 'event' or process at c. 690 Ma that is also dated by samples of lamprophyre. In this scenario, the magmatic crystallization age for carbonatite would need to be older than c. 690 Ma. The obvious candidates, based on data from the analysis of the lamprophyre samples, are c. 800 Ma or c. 860 Ma. However, neither of these dates have been recognized in our carbonatite sample, raising obvious cause for caution with this interpretation. Nevertheless, and curiously, there is a tight clustering of εNd(i)–εHf(i) and isotope data for carbonatite when calculated at 800 Ma. Notably, both carbonatite and lamprophyre are crosscut by calcite-rich veins and show other signs of alteration (e.g. altered olivine, dusty calcite). The age(s) of these alteration and crosscutting calcite veining events are unclear.

- Third, the magmatic crystallization age for carbonatite is younger than c. 690 Ma. In this scenario, as for lamprophyre, all dated minerals reflect xenocrystic components.

Therefore, although our data are not able to unequivocally define the magmatic crystallization age for carbonatite, there is circumstantial evidence to suggest that the magmatic ages for the carbonatite and lamprophyre are similar (if not the same), and possibly c. 690 Ma or younger. This interpretation for carbonatite is necessarily cautious in light of uncertainties around the magmatic age of both lamprophyre and carbonatite, and allows for the possibility that the dated minerals are all xenocrystic.

Regional correlations and mantle source region

Regionally, the geochronology data for lamprophyre and carbonatite samples are similar to known timelines for various geological events. First, the 863 ± 19 Ma and 799 ± 7 Ma dates from this study, and 806 ± 22 Ma for lamprophyre in Sudholz et al. (2023), are similar to the age of mafic magmatism of the 837–816 Ma Willouran Large Igneous Province (LIP) (Goellnicht, 1992; Glikson et al., 1996; Reed, 1996; Wingate et al., 1998; Czarnota et al., 2009; Gardiner et al., 2018; Wingate et al., 2019; Geoscience Australia geochronology delivery portal, 2022, sample GA2006677183), which consist of sets of northwest-trending mafic dykes and sills in South Australia, Northern Territory and Western Australia, approximately following the distribution (or former distribution) of the Centralian Superbasin (e.g. Wingate et al., 1998; Kohanpour et al., 2024). Willouran LIP magmatism has been attributed to the early stages of intracratonic rifting during breakup of Rodinia (e.g. Zhao et al., 1994; Wingate et al., 1998; Li et al., 2008; Merdith et al., 2017). Numerous low-volume alkaline magmatic rocks were also emplaced in the Kimberley Region at about this time (e.g. Downes et al., 2007; Downes et al., 2023; Sudholz et al., 2023). An older suite of mafic dykes, the c. 975 Ma Central Desert Dolerite, outcrop in the Warumpi Province in Western Australia (Wyborn et al., 1998); and age-equivalent metagabbros occur within the Lasseter Shear Zone (Kelsey et al., 2022b; GSWA 228652, Wingate et al., 2024j). This period in the early Neoproterozoic corresponds approximately with deposition of Supersequence I of the intracratonic Centralian Superbasin (e.g. Walter et al., 1995; Grey et al., 2005; Munson et al., 2013).

Emplacement of the Mud Tank Carbonatite into the eastern Aileron Province, located about 620 km east of our study area, occurred at 731.0 ± 0.2 Ma (n = 2272; Gain et al., 2019; cf. Black and Gulson, 1978). This age does not occur in our samples, but our samples show a few dispersed analyses in the 776–758 Ma range (especially in GSWA 262476). These dates are similar to the ages of the c. 755 Ma Mundine Well Dolerite (Wingate and Giddings, 2000), c. 753 Ma Keene Basalt (Zi et al., 2019), and the c. 733 Ma Nindibillup Dolerite (Wingate, 2017; GSWA 199035, Wingate et al., 2020), although the significance, if any, of the correspondence is unknown. The date of c. 690 Ma corresponds to the commencement of deposition of Supersequence 2 within the Centralian Superbasin (e.g. Munson et al., 2013), though the age of this event is not precisely defined. Overall, these various suites of mafic and alkaline magmatic rocks, combined with the lamprophyre and carbonatite documented here, indicate a punctuated Neoproterozoic history of low-volume mantle melting during the early stages of development of the Centralian Superbasin.

The similarity in whole-rock geochemistry between our sampled lamprophyres and those of Sudholz et al. (2023) strongly suggests a similar mantle source with no (or very little) crustal contamination. Carbonatite has a very similar HREE spider profile and overall shape and trend to lamprophyre but is more varied in detail for other elements. Nevertheless, a similar mantle source is probably valid for carbonatite and lamprophyre. Indeed, although there are small differences in εNd(i), εHf(i) and $^{87}Sr/^{86}Sr(i)$ between lamprophyre and carbonatite (depending on assumed age), the differences are not large enough to suggest radically different sources for the two lithotypes. The absence or near-absence of crustal contamination could suggest a lithospheric mantle source either unaffected by processes such as fluid-mediated subduction enrichment, or refertilized from the asthenosphere. This is compatible with the xenocryst-derived geotherm down to 120 km within the lithospheric mantle in Sudholz et al. (2023), who also propose that their studied aillikites were derived from low-volume partial melting of silicate–carbonatite metasomatized peridotite. Given the similarity in whole-rock geochemistry and isotope data from our samples with those of Sudholz et al., the same interpretation is likely valid for this study.

These observations may help explain the origin of Neoproterozoic zircons in lamprophyre, in particular. As they are predominantly of Neoproterozoic age, and crystallization of zircon in (ultra)mafic melts at depth in the mantle has been widely documented (e.g. Griffin et al., 2000; Sun et al., 2018; Page et al., 2007), it is more reasonable to expect that at least some of the lamprophyre zircons, if not all, were sourced from the mantle rather than sourced from crustal rocks during emplacement. This is supported by the known geology of the host rocks in the northern Aileron Province, and in the high-intensity magnetic belt in particular: that is, there are no known Neoproterozoic rocks through which the lamprophyre and carbonatite intruded, and instead these rocks are hosted by Paleoproterozoic and Mesoproterozoic gneisses. For there to be Neoproterozoic crustal rocks at depth in this belt would require not only a radical revision of our understanding of this belt, but also a tectonic driver to place Neoproterozoic crustal rocks at depth prior to emplacement of the lamprophyre and carbonatite, an unlikely scenario given the presently understood tectonic and geodynamic evolution of the Aileron and Warumpi Provinces during the Neoproterozoic and Paleozoic. Xenocrystic Paleoproterozoic zircons in carbonatite attest to at least some wallrock interaction as it was emplaced, but not (so far as is known) sampling of Neoproterozoic mantle zircons by carbonatite melts.

Trace element data reveal that aillikites of this study are more fractionated than those of Sudholz et al. (2023). Only minor and rare narrow carbonatite dykes have so far been identified in the area of the southern Aileron Province studied by Sudholz et al. (2023), despite >250 lamprophyre intrusions being identified. This difference in fractionation could be important in relation to the capacity to form Nb–REE mineralizing carbonatite magmas, perhaps by unmixing, assuming that, in our study area, carbonatite and its Nb–REE mineralization are genetically and temporally related to aillikite lamprophyre through immiscible liquid

separation. Overall, despite ambiguity in interpreting the geochronology results, we tentatively conclude that the igneous crystallization age of lamprophyre and carbonatite is between c. 690 and 635 Ma. Additional geochronology, including the isotope systematics of calcite, biotite and perhaps pyrochlore (Ghobadi et al., 2018), should be attempted to try to resolve this more definitively.

Conclusions

Crystalline basement within the high-intensity magnetic belt intersected by the diamond cores studied here is characterized by granitic gneisses with two distinct magmatic crystallization ages: 1776–1767 Ma and c. 1608 Ma. The older age range corresponds to the Carrington Suite; whereas, the younger age is for granitic gneiss that is mineralogically and visually similar to the Rapide Granite previously dated at c. 1615 Ma within the Northern Territory portion of the same high-intensity magnetic belt, indicating that magmatism at this time spanned at least 1615–1608 Ma. Carrington Suite gneiss is interlayered with gabbronoritic gneiss of unknown age, although older than c. 1615 Ma. Garnet–sillimanite-bearing pelitic migmatite and metamorphosed banded iron-formation also occur in the drillcores, expanding the known occurrence of Fe-rich metasedimentary rocks within this belt (see Wingate et al., 2022b; Kelsey et al., 2022a; Fielding et al., 2023). Within the belt, the widespread 1858–1799 Ma Lander Rock Formation has not been identified, but the Lake Mackay Quartzite and Fe-rich metasedimentary rocks are present. These stratigraphic attributes differentiate this belt from the surrounding lower magnetic intensity regional geology. Granulite facies metamorphism to produce partial melting and migmatization of granitic and pelitic rocks occurred at 1594–1575 Ma.

Basement rocks are intruded by aillikite-type lamprophyre (also highly magnetic) and calcio-carbonatite, both of which are distinctly non-metamorphosed. Alteration and local sodic (antiskarn) metasomatism are common in the drillcores, with the most intense metasomatism occurring in the vicinity of lamprophyre and carbonatite intrusions. Carbonatite and lamprophyre typically do not occur together. However, one drillcore preserves strongly interlayered lamprophyre and carbonatite, strongly suggesting a cogenetic and shared temporal relationship. The precise magmatic crystallization age for emplacement of lamprophyre and carbonatite proved difficult to determine via U–Pb zircon, and U–Pb and Lu–Hf apatite geochronology. A minimum crystallization age of c. 690 Ma is likely, which is younger than aillikite-type lamprophyre documented approximately 60 km south within the Aileron Province by Sudholz et al. (2023). Aillikites documented here are more fractionated than those of Sudholz et al. (2023). This difference in fractionation could be important in relation to the capacity to form Nb–REE mineralizing carbonatite magmas, perhaps by unmixing, assuming that in our study area carbonatite and its Nb–REE mineralization are genetically and temporally related to aillikite lamprophyre.

Acknowledgements

The success of this study is due to many additional people. Thank you to: Encounter Resources Ltd staff, particularly Mark Brodie, Sarah James, Graeme Hardwick and Kate Vinnicombe for donation of non-EIS drillcore and numerous discussions about the drillcores and geology of the tenement; Perth Core Library at Carlisle staff and Monique Brouxhon for rapid facilitation of core viewing and sampling; Lena Hancock and Michael Wawryk for processing of HyLogger™ data; Terry Farrell for facilitating uploading of sample metadata to WAROX; Carlisle laboratory staff for rapid preparation of the samples for zircon and apatite geochronology; Yongjun Lu for facilitation of isotope work; Jack Lowrey for facilitation of whole-rock geochemistry; Sasha Banaszczyk for discussions about the cores while logging and sampling and insight into petrophysics data; and Tim Ivanic and David Martin for thorough reviews. Apatite geochronology was funded from Exploration Incentive Scheme (EIS) project ES55 Novel Geochronology and Isotope Analysis.

References

Alessio, KL, Hand, M, Hasterok, D, Morrissey, LJ, Kelsey, DE and Raimondo, T 2020, Thermal modelling of very long-lived (>140 Myr) high thermal gradient metamorphism as a result of radiogenic heating in the Reynolds Range, central Australia: Lithos, 352–353, article no. 105280, doi:10.1016/j.lithos.2019.105280.

Allaz, JM, Williams, ML, Jercinovic, MJ, Goemann, K and Donovan, J 2019, Multipoint Background Analysis: Gaining Precision and Accuracy in Microprobe Trace Element Analysis: Microscopy and Microanalysis, v. 25, no. 1, p. 30–46, doi:10.1017/S1431927618015660.

Armstrong, JT 1988, Quantitative analysis of silicate and oxide materials: comparison of Monte Carlo, ZAF, and ϕ (pz) procedures, *in* Microbeam analysis – 1988 *edited by* DE Newbury: San Francisco Press, San Francisco, USA, p. 239–246.

Batanova, VG, Thompson, JM, Danyushevsky, LV, Portnyagin, MV, Garbe-Schönberg, D, Hauri, E, Kimura, J-I, Chang, Q, Senda, R, Goemann, K, Chauvel, C, Campillo, S, Ionov, DA and Sobolev, AV 2019, New Olivine Reference Material for *In Situ* Microanalysis: Geostandards and Geoanalytical Research, v. 43, no. 3, p. 453–473, doi:10.1111/ggr.12266.

Belousova EA, Griffin, WL and Pearson, NJ 1998, Trace element composition and cathodoluminescence properties of southern African kimberlitic zircons: Mineralogical Magazine, v. 62, no. 3, p. 355–366.

Beyer, EE 2017, Nature and prospectivity of high-heat-producing granites of the central Aileron Province, Northern Territory: Northern Territory Geological Survey, Record 2017–004, 78p. + map data.

Beyer, EE, Hollis, JA, Whelan, JA, Glass, LM, Donnellan, N, Yaxley, G, Armstrong, R, Allen, C and Scherstén, A 2013, Summary of results. NTGS laser ablation ICPMS and SHRIMP U-Pb, Hf and O geochronology project: Pine Creek Orogen, Arunta Region, Georgina Basin and McArthur Basin, July 2008–May 2011: Northern Territory Geological Survey, Record 2012-007, 205p.

Black, LP and Gulson, BL 1978, The age of the Mud Tank Carbonatite, Strangways Range, Northern Territory: BMR Journal of Australian Geology and Geophysics, v. 3, p. 227–232.

Bouvier, A, Vervoort, JD and Patchett, PJ 2008, The Lu–Hf and Sm–Nd isotopic composition of CHUR: Constraints from unequilibrated chondrites and implications for the bulk composition of terrestrial planets: Earth and Planetary Science Letters, v. 273, no. 1–2, p. 48–57, doi:10.1016/j.epsl.2008.06.010.

Cherniak, DJ, Pyle, J and Rakovan, J 2004, Synthesis of REE and Y phosphates by Pb-free flux methods and their utilization as standards for electron microprobe analysis and in design of monazite chemical U-Th-Pb dating protocol: American Mineralogist, v. 89, no. 10, p. 1533–1539, doi:10.2138/am-2004-1023.

Chew, DM, Petrus, JA and Kamber, BS 2014, U–Pb LA–ICPMS dating using accessory mineral standards with variable common Pb: Chemical Geology, v. 363, p. 185–199, doi:10.1016/j.chemgeo.2013.11.006.

Claoué-Long, JC and Hoatson, D 2005, Proterozoic mafic–ultramafic intrusions in the Arunta Region, central Australia. Part 2: Event chronology and regional correlations: Precambrian Research, v. 142, no. 3-4, p. 134–158, doi:10.1016/j.precamres.2005.08.006.

Close, DF, Scrimgeour, IR and Edgoose, CJ 2004, Mount Rennie SF 52-15, Northern Territory (2nd edition): Geological Survey of Northern Territory, 1:250 000 Geological Series.

Cross, A, Claoué-Long, J, Scrimgeour, IR, Crispe, A and Donnellan, N 2005a, Summary of results. Joint NTGS-GA geochronology project: northern Arunta and Tanami regions, 2000-2003: Northern Territory Geological Survey, Record 2005-003, 69p.

Cross, A, Claoué-Long, JC, Scrimgeour, IR, Close, DF and Edgoose, CJ 2005b, Summary of results, Joint NTGS-GA geochronology project: southern Arunta Region: Northern Territory Geological Survey, Record 2004-003, 61p.

Czarnota, K, Berner, E, Maidment, DW, Meixner, A and Bagas, L 2009, Paterson Area 1:250 000 scale solid geology interpretation and depth to basement model, explanatory notes: Geoscience Australia, Record 2009/16, 89p.

Dalton, H, Giuliani, A, Hergt, J, Phillips, D, O'Brien, H, Ballmer, MD, Maas, R and Woodhead, JD 2022, Geodynamic and Isotopic Constraints on the Genesis of Kimberlites, Lamproites and Related Magmas from the Finnish Segment of the Karelian Craton: Geochemistry Geophysics Geosystems G3, v. 23, article no. e2021GC010324, doi:10.1029/2021GC010324.

Donovan, JJ, Singer, JW and Armstrong, JT 2016, A new EPMA method for fast trace element analysis in simple matrices: American Mineralogist, v. 101, no. 8, p. 1839–1853.

Donovan, JJ, Snyder, DA and Rivers, ML 1993, An Improved Interference Correction for Trace Element Analysis: Microbeam Analysis, v. 2, p. 23–28.

Donovan, JJ and Tingle, TN 1996, An Improved Mean Atomic Number Correction for Quantitative Microanalysis: Journal of Microscopy, v. 2, p. 1–7.

Doublier, MP, Johnson, SP, Gessner, KT, Howard, HM, Chopping, R, Smithies, RH, Martin, DMcB, Kelsey, DE, Haines, PW, Hickman, AH, Czarnota, K, Southby, C, Champion, DC, Huston, DL, Calvert, AJ, Kohanpour, F, Moro, P, Costelloe, R, Fomin, T and Kennett, BLN 2020, Basement architecture from the Pilbara Craton to the Aileron Province: new insights from deep seismic reflection line 18GA-KB1, *in* Exploring for the future: Extended Abstracts *edited by* K Czarnota, IC Roach, S Abbott, M Haynes, N Kositcin, A Ray and E Slatter: Geoscience Australia, Canberra, p. 1–6.

Downes, PJ, Griffin, BJ and Griffin, WL 2007, Mineral chemistry and zircon geochronology of xenocrysts and altered mantle and crustal xenoliths from the Aries micaceous kimberlite: Constraints on the composition and age of the central Kimberley Craton, Western Australia: Lithos, v. 93, no. 1-2, p. 175–198, doi:10.1016/j.lithos.2006.06.005.

Downes, PJ, Jaques, AL, Talavera, C, Griffin, WL, Gain, SE, Evans, NJ, Taylor, WR and Verrall, M 2023, Perovskite geochronology and petrogenesis of the Neoproterozoic Mad Gap Yards ultramafic lamprophyre dykes, East Kimberley region, Western Australia: Contributions to Mineralogy and Petrology, v. 178, no. 4, article no. 21, doi:10.1007/s00410-023-02002-2.

Droop, GTR 1987, A general equation for estimating Fe^{3+} concentrations in ferromagnesian silicates and oxides from microprobe analyses, using stoichiometric criteria: Mineralogical Magazine, v. 51, no. 361, p. 431–435.

Edgoose, CJ, Close, DF and Scrimgeour, IR 2008a, Lake Mackay, Northern Territory, SF 52-11: Northern Territory Geological Survey, 1:250 000 scale interpreted geological map.

Edgoose, CJ, Close, DF and Scrimgeour, IR 2008b, Lake Mackay, Northern Territory, SF 52-11 (2nd edition): Northern Territory Geological Survey, 1:250 000 geological map series.

Encounter Resources Ltd 2023, Mineralised carbonatites intersected over 3.5km - West Arunta: Australian Securities Exchange (ASX), 18p., released 28 June 2023, <https://www.asx.com.au/asx/v2/statistics/displayAnnouncement.do?display=pdf&idsId=02680432>.

Encounter Resources Ltd 2024, Hurley & Crean - large, depth extensive, mineralised carbonatites: Australian Securities Exchange (ASX), 13p., released 29 January 2024, <https://www.encounterresources.com.au/wpfd_file/hurley-crean-large-depth-extensive-mineralised-carbonatites/>.

Fielding, IOH, Lu, Y, Wingate, MTD, Kelsey, DE and Spaggiari, CV 2023, 243071.1: garnet-bearing sillimanite–magnetite pelitic schist, Radiator prospect; Geochronology Record 1909: Geological Survey of Western Australia, <www.demirs.wa.gov.au/geochron>.

Frogtech Geoscience 2017, 2017 Canning Basin SEEBASE study and GIS data package: Geological Survey of Western Australia, Report 182, 297p.

Gain, SEM, Gréau, Y, Henry, H, Belousova, E, Dainis, I, Griffin, WL and O'Reilly, SY 2019, Mud Tank zircon: long-term evaluation of a reference material for U-Pb dating, Hf-isotope analysis and trace element analysis: Geostandards and Geoanalytical Research, v. 43, no. 3, p. 339–354, 16p., doi:10.1111/ggr.12265.

Gardiner, NJ, Maidment, DW, Kirkland, CL, Bodorkos, S, Smithies, RH and Jeon, H 2018, Isotopic insight into the Proterozoic crustal evolution of the Rudall Province, Western Australia: Precambrian Research, v. 313, 31–50., doi:10.1016/j.precamres.2018.05.003.

Ghobadi, M, Gerdes, A, Kogarko, L, Hoefer, H and Brey, G 2018, In situ LA-ICPMS Isotopic and Geochronological Studies on Carbonatites and Phoscorites from the Guli Massif, Maymecha-Kotuy, Polar Siberia: Geochemistry International, v. 56, no. 8, p. 766–783, doi:10.1134/S0016702918080049.

Glikson, AY, Stewart, AJ, Ballhaus, CG, Clarke, GL, Feeken, EHT, Leven, JH, Sheraton, JW and Sun, SS 1996, Geology of the western Musgrave Block, central Australia, with particular reference to the mafic-ultramafic Giles Complex: Australian Geological Survey Organisation, Bulletin 239, 206p.

Goellnicht, NM 1992, Late Proterozoic fractionated granitoids and their role in the genesis of gold and base-metal mineralization in the Telfer district, Western Australia: The University of Western Australia, Perth, PhD thesis (unpublished), 132p.

Grey, K, Hocking, RM, Stevens, MK, Bagas, L, Carlsen, GM, Irimies, F, Pirajno, F, Haines, PW and Apak, SN 2005, Lithostratigraphic nomenclature of the Officer Basin and correlative parts of the Paterson Orogen, Western Australia: Geological Survey of Western Australia, Report 93, 89p.

Griffin, WL, Pearson, NJ, Belousova, EA, Jackson, SE, O'Reilly, SY, van Achterbergh, E and Shee, SR 2000, The Hf isotope composition of cratonic mantle: LAM-MC-ICPMS analysis of zircon megacrysts in kimberlites: Geochimica et Cosmochimica Acta, v. 64, no. 1, p. 133–147, doi:10.1016/S0016-7037(99)00343-9.

Haines, PW and Allen, HJ 2017, Geological reconnaissance of the southern Murraba Basin, Western Australia: revised stratigraphic position within the Centralian Superbasin and hydrocarbon potential: Geological Survey of Western Australia, Record 2017/4, 38p.

Haines, PW and Allen, HJ 2019, Angas Hills Formation (P_E-_ag-sg): Geological Survey of Western Australia, WA Geology Online, Explanatory Notes extract, viewed 17 September 2024, <www.dmp.wa.gov.au/ens>.

Haines, PW, de Souza Kovacs, N, Spaggiari, CV, Eacott, GR, Allen, HJ, Tyler, IM, Maidment, DW and Murdie, RE 2018, Macdonald, WA Sheet SF 52-14 (2nd edition): Geological Survey of Western Australia, 1:250 000 Geological Series.

Haines, PW, Wingate, MTD, Kirkland, CL and Allen, HJ 2015, Detrital zircon geochronology of upper Ediacaran to lower Cambrian deposits (Supersequence 4), western Amadeus Basin: testing revised stratigraphic correlations: Geological Survey of Western Australia, Record 2015/8, 35p.

Hawthorne, FC, Oberti, R, Harlow, GE, Maresch, WV, Martin, RF, Schumacher, JC and Welch, MD 2012, Nomenclature of the amphibole supergroup: American Mineralogist, v. 97, no. 11–12, p. 2031–2048, doi:10.2138/am.2012.4276.

Hoatson, DM, Sun, S-S and Claoué-Long, JC 2005, Proterozoic mafic–ultramafic intrusions in the Arunta Region, central Australia: Part 1: Geological setting and mineral potential: Precambrian Research, v. 142, no. 3–4, p. 93–133, doi:10.1016/j.precamres.2005.09.004.

Hollis, JA, Kirkland, CL, Spaggiari, CV, Tyler, IM, Haines, PW, Wingate, MTD, Belousova, EA and Murphy, RC 2013, Zircon U–Pb–Hf isotope evidence for links between the Warumpi and Aileron Provinces, west Arunta region: Geological Survey of Western Australia, Record 2013/9, 30p.

Hu, Z, Gao, S, Liu, Y, Hu, S, Chen, H and Yuan, H 2008, Signal enhancement in laser ablation ICP-MS by addition of nitrogen in the central channel gas: Journal of Analytical Atomic Spectrometry, v. 23, no. 8, p. 1093–1101, doi:10.1039/b804760j.

Jarosewich, E and MacIntyre, IG, 1983, Carbonate reference samples for electron microprobe and scanning electron microscope analyses: Journal of Sedimentary Research (1983) 53 (2): 677–678.

Kelsey, DE, Korhonen, FJ, Romano, SS and Spaggiari, CV 2022a, 243071.2: garnet-bearing sillimanite–magnetite pelitic schist, Radiator prospect; Metamorphic History Record 28: Geological Survey of Western Australia, 9p., <www.demirs.wa.gov.au/geochron>.

Kelsey, DE, Wingate, MTD, Spaggiari, CV, Smithies, RH, Fielding, IOH, Lu, Y, Porter, JK and Finch, EG 2022b, Crystalline basement beneath the eastern Canning Basin at the Top Up Rise prospect: Geological Survey of Western Australia, Perth, Western Australia, Record 2022/17, 22p.

Kinny, PD 2002, SHRIMP U-Pb geochronology of Arunta Province samples from the Mount Liebig and Lake Mackay 1:250 000 mapsheets: Northern Territory Geological Survey, Technical Note 2002-015.

Kirkland, CL, Smithies, RH, Spaggiari, CV, Wingate, MTD, Quentin de Gromard, R, Clark, C, Gardiner, NJ and Belousova, EA 2017, Proterozoic crustal evolution of the Eucla basement, Australia: Implications for destruction of oceanic crust during emergence of Nuna: Lithos, v. 278, p. 427–444.

Kirkland, CL, Wingate, MTD, Spaggiari, CV and Tyler, IM 2009, 184341: quartzite, Lake Mackay 818: Geological Survey of Western Australia, Geochronology Record 818, 5p.

Kohanpour, F, Tyler, I, Gorczyk, W, Kelsey, D, Fisher, C and Kemp, A 2024, Early-stage intracontinental rifting in the Neoproterozoic Centralian Superbasin: Systematic U–Pb and Lu–Hf isotopes in detrital and inherited zircons from the Yeneena Basin, northwest Australia: Precambrian Research, v. 411, article no. 107524, doi:10.1016/j.precamres.2024.107524.

Korhonen, FJ, Kelsey, DE, Fielding, IOH and Romano, SS 2020, The utility of the metamorphic rock record: constraining the pressure–temperature–time conditions of metamorphism: Geological Survey of Western Australia, Record 2020/14, 24p.

Kositcin, N, Beyer, EE and Whelan, JA 2014, Summary of results. Joint NTGS–GA SHRIMP geochronology project: Arunta region, July 2013–June 2014: Northern Territory Geological Survey, NTGS Record 2014-008, 30p.

Kositcin, N, Beyer, EE, Whelan, JA, Close, DF, Hallett, L and Dunkley, DJ 2013, Summary of results. Joint NTGS-GA geochronology project: Arunta Region, Ngalia Basin, Tanami Region and Murphy Province, July 2011–June 2012: Northern Territory Geological Survey, Record 2013-004, 39p.

Kositcin, N and McGloin, MV 2017, Summary of results. Joint NTGS–GA geochronology project: Aileron Province, July 2016–June 2017: Northern Territory Geological Survey, Record 2017-011, 16p.

Li, X-Y, Zhang, C, Behrens, H and Holtz, F 2020a, Calculating amphibole formula from electron microprobe analysis data using a machine learning method based on principal components regression: Lithos, 362-363, article no. 105469, doi:10.1016/j.lithos.2020.105469.

Li, X-Y, Zhang, C, Behrens, H and Holtz, F 2020b, Calculating biotite formula from electron microprobe analysis data using a machine learning method based on principal components regression: Lithos, 356-357, article no. 105371, doi:10.1016/j.lithos.2020.105371.

Li, X-Y, Zhang, C, Behrens, H and Holtz, F 2022, On the improvement of calculating biotite formula from EPMA data: Reexamination of the methods of Dymek (1983), Yavuz and Öztas (1997), Li et al. (2020) and reply to the discussion of Baidya and Das: Lithos, 412–413, article no. 106403, doi:10.1016/j.lithos.2021.106403.

Li, Y and Vermeesch, P 2021, Short Communication: Inverse isochron regression for Re-Os, K-Ca and other chronometers: Geochronology Discussions, v. 3, no. 2, p. 415–420, doi:10.5194/gchron-3-415-2021.

Li, ZX, Bogdanova, SV, Collins, AS, Davidson, A, Waele, B de, Ernst, RE, Fitzsimons, ICW, Fuck, RA, Gladkochub, DP, Jacobs, J, Karlstrom, KE, Lu, S, Natapov, LM, Pease, V, Pisarevsky, SA, Thrane, K and Vernikovsky, V 2008, Assembly, configuration, and break-up history of Rodinia: A synthesis: Precambrian Research, v. 160, no. 1–2, p. 179–210, doi:10.1016/j.precamres.2007.04.021.

Lowrey, JR, Smithies, RH, Champion, DC and Cassidy, KC 2023, Systematic classification of Yilgarn Craton granitic rocks: Geological Survey of Western Australia; Record 2023/12, 27p.

Lu, Y, Wingate, MTD, Smithies, RH, Gessner, K, Johnson, SP, Kemp, AIS, Kelsey, DE, Haines, PW, Martin, DMcB, Martin, L and Lindsay, M 2022, Preserved intercratonic lithosphere reveals Proterozoic assembly of Australia: Geology, v. 50, no. 10, p. 1202–1207, doi:10.1130/G50256.1.

March, S, Hand, M, Morrissey, L and Kelsey, D 2024, Extension during the Liebig Orogeny: revised tectonic setting of Paleoproterozoic central Australia: Gondwana Research, v. 134, p. 365–384, doi:10.1016/j.gr.2024.07.013.

Marincea, Ș, Dumitraș, D-G, Sava Ghineț, C and Dal Bo, F 2022, Carbonate-Bearing, F-Overcompensated Fluorapatite in Magnesian Exoskarns from Valea Rea, Budureasa, Romania: Minerals, v. 12, article no. 1083, doi:10.3390/min12091083.

Martin, DMcB, Murdie, RE, Kelsey, DE, Quentin de Gromard, R, Thomas, CM, Cutten, HN, Zhan, Y, Haines, PW and Brett, J 2022, Compilation and geological implications of the major crustal boundaries map and 3D model of Western Australia: Geological Survey of Western Australia, Record 2022/7, 49p.

McGregor, N, Murphy, D and James, S 2021, Annual Report for C195/2020 – Aileron project combined annual mineral exploration report E80/5169, E80/5469, E80/5470, 8 January 2020 to 7 January 2021: Hamelin Resources Pty Ltd: Geological Survey of Western Australia, Statutory mineral exploration report A126702, <www.demirs.wa.gov.au/wamex>, 20p.

McGuire, AV, Francis, CA and Dyar, MD 1992, Mineral standards for electron microprobe analysis of oxygen: American Mineralogist, v. 77, no. 9–10, p. 1087–1091.

Merdith, AS, Collins, AS, Williams, SE, Pisarevsky, S, Foden, JD, Archibald, DB, Blades, ML, Alessio, BL, Armistead, S, Plavsa, D, Clark, C and Müller, RD 2017, A full-plate global reconstruction of the Neoproterozoic: Gondwana Research, v. 50, p. 84–134, doi:10.1016/j.gr.2017.04.001.

Moy, A, Fournelle, J, Nachlas, W, Dungan, M, Locock, A, Bullock, E, Donovan, J, Cathey, H, Allaz, J and von der Handt, A 2023, On the importance of including all elements in the EPMA matrix correction: Microscopy and Microanalysis, v. 29, no. Supplement_1, p. 855–856, doi:10.1093/micmic/ozad067.424.

Münker, C, Weyer, S, Scherer, E and Mezger, K 2001, Separation of high field strength elements (Nb, Ta, Zr, Hf) and Lu from rock samples for MC-ICPMS measurements: Geochemistry Geophysics Geosystems G3, v. 2, no. 12, article no. 2001GC000183, doi:10.1029/2001GC000183.

Munson, TJ, Kruse, PD and Ahmad, M 2013, Chapter 22: Centralian Superbasin, *in* Geology and mineral resources of the Northern Territory *compiled by* M Ahmad and TJ Munson: Northern Territory Geological Survey, Special Publication 5, p. 22:1–22:19.

Nebel, O, Morel, MLA, Vroon, PZ et al., 2009, Isotope Dilution Determinations of Lu, Hf, Zr, Ta and W, and Hf Isotope Compositions of NIST SRM 610 and 612 Glass Wafers: Geostandards and Geoanalytical Research, v. 33, no. 4. p.487–499, doi:10.1111/j.1751-908X.2009.00032.x.

Page, FZ, Fu, B, Kita, NT, Fournelle, J, Spicuzza, MJ, Schulze, DJ, Viljoen, F, Basei, MAS and Valley, JW 2007, Zircons from kimberlite: New insights from oxygen isotopes, trace elements, and Ti in zircon thermometry: Geochimica et Cosmochimica Acta, v. 71, no. 15, p. 3887–3903, doi:10.1016/j.gca.2007.04.031.

Paton, C, Hellstrom, J, Paul, B, Woodhead, J and Hergt, J 2011, Iolite: Freeware for the visualization and processing of mass spectrometer data: Journal of Analytical Atomic Spectrometry, v. 26, p. 2508–2518.

Pearce, JA, Harris, NB and Tindle, AG 1984, Trace Element Discrimination Diagrams for the Tectonic Interpretation of Granitic Rocks: Journal of Petrology v. 25, no. 4, p. 956–983

Reddy, D 2012, Surrender Report, Webb Project E80/3820 East Pilbara Shire, Western Australia, Reporting period 30 January 2008 to 12 June 2012: Meteoric Resources NL: Geological Survey of Western Australia, Statutory mineral exploration report A94934, <www.demirs.wa.gov.au/wamex>, 22p., (unpublished).

Reed, A 1996, The structural, stratigraphic and temporal setting of the Maroochydore copper prospect, Paterson Orogen, Western Australia: The University of Western Australia, Perth, Australia, PhD thesis (unpublished), 289p.

Ribeiro, BV, Kirkland, CL, Smit, M, Musiyachenko, K, Korhonen, FJ, Evans, NJ, Rankenburg, K, McDonald, BJ, Glorie, S, Goemann, K, Belousov, I, Oalmann, J, Clark, C and Makin, S 2024, Garnet Reference Materials for In Situ Lu-Hf Geochronology: Geostandards and Geoanalytical Research, doi:10.1111/ggr.12579.

Rubatto, D, Williams, IS and Buick, IS 2001, Zircon and monazite response to prograde metamorphism in the Reynolds Range, central Australia: Contributions to Mineralogy and Petrology, v. 140, no. 4, p. 458–468.

Scherer, E, Münker, C and Mezger, K 2001, Calibration of the Lutetium–Hafnium Clock: Science, v. 293, p. 683–687, doi:10.1126/science.1061372.

Schmitz, MD, Bowring, SA and Ireland, TR 2003, Evaluation of Duluth Complex anorthositic series (AS3) zircon as a U-Pb geochronological standard: new high-precision isotope dilution thermal ionization mass spectrometry results: Geochimica et Cosmochimica Acta, v. 67, no. 19, p. 3665–3672, doi:10.1016/S0016-7037(03)00200-X.

Schoene, B and Bowring, SA 2006, U–Pb systematics of the McClure Mountain syenite: thermochronological constraints on the age of the $^{40}Ar/^{39}Ar$ standard MMhb: Contributions to Mineralogy and Petrology, v. 151, no. 5, p. 615–630, doi:10.1007/s00410-006-0077-4.

Scrimgeour, IR 2013a, Chapter 12: Aileron Province, *in* Geology and mineral resources of the Northern Territory *compiled by* M Ahmad and TJ Munson: Northern Territory Geological Survey, Special Publication 5, p. 12:1–12:74.

Scrimgeour, IR 2013b, Chapter 13: Warumpi Province, *in* Geology and mineral resources of the Northern Territory *compiled by* M Ahmad and TJ Munson: Northern Territory Geological Survey, Special Publication 5, p. 13:1–13:21.

Scrimgeour, IR, Close, DF and Edgoose, CJ 2005a, Mount Liebig, Northern Territory, SF 52-16: Explanatory notes: Northern Territory Geological Survey, 1:250 000 Geological Map Series Explanatory Notes.

Scrimgeour, IR, Kinny, PD, Close, DF and Edgoose, CJ 2005b, High-*T* granulites and polymetamorphism in the southern Arunta Region, central Australia: Evidence for a 1.64 Ga accretional event: Precambrian Research, v. 142, no. 1–2, p. 1–27, doi:10.1016/j.precamres.2005.08.005.

Simeonova, A 2024, C195/2020 – Aileron project combined annual mineral exploration report for the period ending 07/01/2024: Encounter Resources Limited: Geological Survey of Western Australia, Statutory mineral exploration report A139448, <www.demirs.wa.gov.au/wamex>, 25p.

Simeonova, A and Hardwick, G 2023, EIS Co-funded drilling Aileron project final report – round 26, DAG2022/00837276: Encounter Resources Limited: Geological Survey of Western Australia, Statutory mineral exploration report A137593, <www.demirs.wa.gov.au/wamex>, 16p.

Simpson, A, Gilbert, S, Tamblyn, R, Hand, M, Spandler, C, Nixon, A and Glorie, S 2021, In-situ Lu Hf geochronology of garnet, apatite and xenotime by LA ICP MS/MS: Chemical Geology, v. 577, article no. 120299, doi:10.1016/j.chemgeo.2021.120299.

Simpson, A, Glorie, S, Hand, M, Gilbert, S, Spandler, C, Dmitrijeva, M, Swain, G, Nixon, A, Mulder, J and Münker, C 2024, *In situ* apatite and carbonate Lu–Hf and molybdenite Re–Os geochronology for ore deposit research: Method validation and example application to Cu–Au mineralisation: Geoscience Frontiers, v. 15, no. 5, article no. 101867, doi:10.1016/j.gsf.2024.101867.

Söderlund, U, Patchett, PJ, Vervoort, JD and Isachsen, CE 2004, The ^{176}Lu decay constant determined by Lu–Hf and U–Pb isotope systematics of Precambrian mafic intrusions: Earth and Planetary Science Letters, v. 219, no. 3, p. 311–324.

Spaggiari, CV, Haines, PW, Tyler, IM, Allen, H-J, de Souza Kovacs, N and Maidment, D 2016, Webb, WA Sheet SF 52-10 (2nd edition): Geological Survey of Western Australia, 1:250 000 Geological Series.

Stacey, JS and Kramers, JD 1975, Approximation of terrestrial lead isotope evolution by a two-stage model, Earth and Planetary Science Letters v. 26, no. 2, p. 207–221.

Sudholz, ZJ, Reddicliffe, TH, Jaques, AL, Yaxley, GM, Haynes, M, Gorbatov, A, Czarnota, K, Frigo, C, Maas, R and Knowles, B 2023, Petrology, Age, and Rift Origin of Ultramafic Lamprophyres (Aillikites) at Mount Webb, a New Alkaline Province in Central Australia: Geochemistry Geophysics Geosystems G3, v. 24, no. 10, article no. e2023GC011120, doi:10.1029/2023GC011120.

Sun, J, Tappe, S, Kostrovitsky, SI, Liu, C-Z, Skuzovatov, SY and Wu, F-Y 2018, Mantle sources of kimberlites through time: A U–Pb and Lu–Hf isotope study of zircon megacrysts from the Siberian diamond fields: Chemical Geology, v. 479, p. 228–240, doi:10.1016/j.chemgeo.2018.01.013.

Sun, S-S and McDonough, WF 1989, Chemical and isotopic systematics of oceanic basalts: Implications for mantle composition and processes, *in* Magmatism in the Ocean Basins *edited by* AD Saunders and MJ Norry: The Geological Society of London, Special Publication 42, p. 313–345.

Tappe, S, Foley, SF, Jenner, GA, Heaman, LM, Kjarsgaard, BA, Romer, RL, Stracke, A, Joyce, N and Hoefs, J 2006, Genesis of Ultramafic Lamprophyres and Carbonatites at Aillik Bay, Labrador: a Consequence of Incipient Lithospheric Thinning beneath the North Atlantic Craton: Journal of Petrology, v. 47, no. 7, p. 1261–1315.

Thomson, SN, Gehrels, GE, Ruiz, J and Buchwaldt, R 2012, Routine low-damage apatite U-Pb dating using laser ablation–multicollector–ICPMS: Geochemistry Geophysics Geosystems G3, v. 13, no. 2, doi:10.1029/2011GC003928.

van Raalte, K 2023, Final surrender report E80/4407 Webb project for the period ending 11/5/2023: CGN Resources Limited: Geological Survey of Western Australia, Statutory mineral exploration report A136003, <www.demirs.wa.gov.au/wamex>, 28p.

Vance, D and Thirwall, MF 2002, An assessment of mass discrimination in MC-ICPMS using Nd isotopes: Chemical Geology, v. 185, no. 3–4, p. 227–240, doi:10.1016/S0009-2541(01)00402-8.

Vandenberg, L, Green, M and Crispe, A 2006, Highland Rocks, Northern Territory, SF 52-07 (2nd edition): Northern Territory Geological Survey, 1:250 000 geological map series.

Velásquez-Ruiz, F, Reich, M, Broom-Fendley, S, Beard, CD, Barra, F, Romero, R and Cordiero, P 2024, Origin of carbonatite-related niobium deposits: Insights from pyrochlore geochemistry: Geochimica et Cosmochimica Acta, v. 366, p. 1–16, doi:10.1016/j.gca.2023.12.010.

Vermeesch, P 2018, IsoplotR: A free and open toolbox for geochronology: Geoscience Frontiers, v. 9, p. 1479–1493.

Vervoort, JD, Patchett, JP, Söderlund, U and Baker, M 2004, Isotopic composition of Yb and the determination of Lu concentrations and Lu/Hf ratios by isotope dilution using MC-ICPMS: Geochemistry Geophysics Geosystems G3, v. 5, no. 11, doi:10.1029/2004GC000721.

Veter, M, Foley, SF, Mertz-Kraus, R and Groschopf, N 2017, Trace elements in olivine of ultramafic lamprophyres controlled by phlogopite-rich mineral assemblages in the mantle source: Lithos, v. 292, p. 81–95, doi:10.1016/j.lithos.2017.08.020.

WA1 Resources Ltd 2022, West Arunta project: discovery of niobium-REE mineralised carbonatite system: Australian Securities Exchange (ASX), 13p., released 26 October 2022, <https://announcements.asx.com.au/asxpdf/20221026/pdf/45gryt4b4970gs.pdf>.

WA1 Resources Ltd 2023, West Arunta project: high-grade enriched niobium horizon extends at Luni: Australian Securities Exchange (ASX), 15p., released 21 August 2023, <https://announcements.asx.com.au/asxpdf/20230821/pdf/05stnbtnw49xtq.pdf>.

Waight, T, Baker, J and Willigers, B 2002, Rb isotope dilution analyses by MC-ICPMS using Zr to correct for mass fractionation: towards improved Rb–Sr geochronology?: Chemical Geology, v. 186, no. 1–2, p. 99–116, doi:10.1016/S0009-2541(01)00420-X.

Walter, MR and Veevers, JJ 1997, Australian Neoproterozoic palaeogeography, tectonics, and supercontinental connections: AGSO Journal of Australian Geology & Geophysics, v. 17, p. 73–92.

Walter, MR, Veevers, JJ, Calver, CR and Grey, K 1995, Neoproterozoic stratigraphy of the Centralian Superbasin, Australia: Precambrian Research, v. 73, no. 1-4, p. 173–195, doi:10.1016/0301-9268(94)00077-5.

Whalen, JB, Currie, KL and Chappell, BW 1987, A-type granites: geochemical characteristics, discrimination and petrogenesis: Contributions to Mineralogy and Petrology, v. 95, p. 407–419.

White, RW, Powell, R, Holland, TJB, Johnson, TE and Green, ECR 2014a, New mineral activity–composition relations for thermodynamic calculations in metapelitic systems: Journal of Metamorphic Geology, v. 32, no. 3, p. 261–286, doi:10.1111/jmg.12071.

White, RW, Powell, R and Johnson, TE 2014b, The effect of Mn on mineral stability in metapelites revisited: New *a–x* relations for manganese-bearing minerals: Journal of Metamorphic Geology, v. 32, p. 809–828, doi:10.1111/jmg.12095.

Wingate, MTD 2017, Mafic dyke swarms and large igneous provinces in Western Australia get a digital makeover: Geological Survey of Western Australia, Record 2017/2, p. 4–8.

Wingate, MTD, Campbell, IH, Compston, W and Gibson, GM 1998, Ion microprobe U–Pb ages for Neoproterozoic basaltic magmatism in south-central Australia and implications for the breakup of Rodinia: Precambrian Research, v. 87, no. 3–4, p. 135–159, doi:10.1016/S0301-9268(97)00072-7.

Wingate, MTD, Denyszyn, S and Lu, Y 2020, 199035: dolerite dyke, Lort River; Geochronology Record 1676: Geological Survey of Western Australia, 4p.

Wingate, MTD, Fielding, IOH, Kelsey, DE, Turnbull, RE and Lu, Y 2024a, 262476.1: lamprophyre dyke, Crean prospect; Geochronology Record 2006: Geological Survey of Western Australia, 3p., <www.demirs.wa.gov.au/geochron>.

Wingate, MTD, Fielding, IOH and Lu, Y 2022a, 203749: altered granitic rock, Aileron prospect; Geochronology Record 1897: Geological Survey of Western Australia, 5p., <www.demirs.wa.gov.au/geochron>.

Wingate, MTD, Fielding, IOH, Lu, Y, Kelsey, DE and Tyler, IM 2024b, 184344.1: quartzite, Lake Mackay; Geochronology Record 2000: Geological Survey of Western Australia, 4p., <www.demirs.wa.gov.au/geochron>.

Wingate, MTD, Fielding, IOH, Turnbull, RE and Kelsey, DE 2024c, 262503.1: monzogranite gneiss, Crean prospect; Geochronology Record 2007: Geological Survey of Western Australia, 3p., <www.demirs.wa.gov.au/geochron>.

Wingate, MTD, Fielding, IOH, Turnbull, RE and Kelsey, DE 2024d, 262515.1: monzogranite gneiss, Crean prospect; Geochronology Record 2008: Geological Survey of Western Australia, 3p., <www.demirs.wa.gov.au/geochron>.

Wingate, MTD, Fielding, IOH, Turnbull, RE and Kelsey, DE 2024e, 262550.1: pelitic migmatite, Crean prospect; Geochronology Record 2009: Geological Survey of Western Australia, 4p., <www.demirs.wa.gov.au/geochron>.

Wingate, MTD, Fielding, IOH, Turnbull, RE, Lu, Y and Kelsey, DE 2024f, 184343.1: granitic gneiss, Lake Mackay; Geochronology Record 1999: Geological Survey of Western Australia, 4p., <www.demirs.wa.gov.au/geochron>.

Wingate, MTD, Fielding, IOH, Turnbull, RE, Lu, Y and Kelsey, DE 2024g, 262435.1: calcite carbonatite, Hoschke prospect; Geochronology Record 2003: Geological Survey of Western Australia, 3p., <www.demirs.wa.gov.au/geochron>.

Wingate, MTD, Fielding, IOH, Turnbull, RE, Lu, Y and Kelsey, DE 2024h, 262447.1: monzogranite gneiss, Hoschke prospect; Geochronology Record 2004: Geological Survey of Western Australia, 3p., <www.demirs.wa.gov.au/geochron>.

Wingate, MTD, Fielding, IOH, Turnbull, RE, Lu, Y and Kelsey, DE 2024i, 262471.1: granitic gneiss, Caird prospect; Geochronology Record 2005: Geological Survey of Western Australia, 3p., <www.demirs.wa.gov.au/geochron>.

Wingate, MTD, Lu, Y, Fielding, IOH, Kelsey, DE and Spaggiari, CV 2024j, 228652: metagabbro, Top Up Rise; Geochronology Record 1941: Geological Survey of Western Australia, <www.demirs.wa.gov.au/geochron>.

Wingate, MTD, Lu, Y, Fielding, IOH, Kelsey, DE and Spaggiari, CV 2022b, 243061: siliciclastic schist, Radiator prospect; Geochronology Record 1389: Geological Survey of Western Australia, 6p., <www.demirs.wa.gov.au/geochron>.

Wingate, MTD, Lu, Y and Haines, PW 2019, 199495: metagabbro vein, Frankenstein 1; Geochronology Record 1561: Geological Survey of Western Australia, 4p., <www.demirs.wa.gov.au/geochron>.

Woodhead, J, Hergt, J, Giuliani, A, Maas, R, Phillips, D, Pearson, DG and Nowell, G 2019, Kimberlites reveal 2.5-billion-year evolution of a deep, isolated mantle reservoir: Nature, v. 573, p. 578–581, doi:10.1038/s41586-019-1574-8.

Worden, KE, Carson, CJ, Close, DF, Donnellan, N and Scrimgeour, IR 2008, Summary of results. Joint NTGS-GA geochronology project: Tanami Region, Arunta Region, Pine Creek Orogen, and Halls Creek Orogen correlatives, January 2005 – March 2007: Northern Territory Geological Survey, Record 2008-003, 180p.

Worden, KE, Claoué-Long, JC and Scrimgeour, IR 2006, Summary of results. Joint NTGS-GA geochronology project: Pine Creek Orogen, Tanami Region, Arunta Region and Amadeus Basin, July–December 2004: Northern Territory Geological Survey, Record 2006-006, 63p.

Wray, S 2023, Combined annual report on exploration for the period 1/04/2022 to 31/03/2023, C170/2022: WA1 Resources Ltd: Geological Survey of Western Australia, Statutory mineral exploration report A135789, <www.demirs.wa.gov.au/wamex>, 18p.

Wyborn, LAI, Hazell, M, Page, R, Idnurm, M and Sun, S-S 1998, A newly discovered major Proterozoic granite-alteration system in the Mount Webb region, central Australia, and implications for Cu–Au mineralisation: Australian Geological Survey Organisation, Research Newsletter 28, 1–6.

Yaxley, GM, Anenburg, M, Tappe, S, Decree, S and Guzmics, T 2022, Carbonatites: Classification, Sources, Evolution, and Emplacement: Annual Review of Earth and Planetary Sciences, v. 50, no. 1, p. 261–293, doi:10.1146/annurev-earth-032320-104243.

Young, DN, Edgoose, CJ, Blake, DH and Shaw, RD 1995a, Mount Doreen SF 52-12 (2nd edition): Geological Survey of Northern Territory, Darwin, Northern Territory, 1:250 000 Geological Series Explanatory Notes, 55p.

Young, DN, Fanning, CM, Shaw, RD, Edgoose, CJ, Blake, DH, Page, RW and Camacho, A 1995b, U Pb zircon dating of tectonomagmatic events in the northern Arunta Inlier, central Australia: Precambrian Research, v. 71, p. 45–68.

Zhan, Y 2018, A seismic interpretation of the southwestern Canning Basin, Western Australia: Geological Survey of Western Australia, Report 178, 34p.

Zhao, J-X and Bennett, VC 1995, SHRIMP U-Pb zircon geochronology of granites in the Arunta Inlier, central Australia: implications for Proterozoic crustal evolution: Precambrian Research, v. 71, p. 17–43.

Zhao, J-X, McCulloch, MT and Korsch, RJ 1994, Characterisation of a plume-related ~800 Ma magmatic event and its implications for basin formation in central-southern Australia: Earth and Planetary Science Letters, v. 121, no. 3–4, p. 349–367, doi:10.1016/0012-821X(94)90077-9.

Zhao, L, Tyler, IM, Gorczyk, W, Murdie, RE, Gessner, K, Lu, Y, Smithies, H, Li, T, Yang, J, Zhan, A, Wan, B, Sun, B and Yuan, H 2022, Seismic evidence of two cryptic sutures in Northwestern Australia: Implications for the style of subduction during the Paleoproterozoic assembly of Columbia: Earth and Planetary Science Letters, v. 579, article no. 117342, 11p., doi:10.1016/j.epsl.2021.117342.

Zi, J-W, Haines, PW, Wang, X-C, Jourdan, F, Rasmussen, B, Halverson, GP, Sheppard, S and Li, C-F 2019, Pyroxene $^{40}Ar/^{39}Ar$ Dating of Basalt and Applications to Large Igneous Provinces and Precambrian Stratigraphic Correlations: Journal of Geophysical Research: Solid Earth, v. 124, 18p., doi:10.1029/2019JB017713.

Zurevinski, SE and Mitchell, RH 2004, Extreme compositional variation of pyrochlore-group minerals at the Oka Carbonatite Complex, Quebec: evidence of magma mixing? The Canadian Mineralogist, v. 42, no. 4, p. 1159–1168, doi:10.2113/gscanmin.42.4.1159.

RECORD 2024/5

CARBONATITE, LAMPROPHYRE AND HOST ROCKS IN THE NORTHERN AILERON PROVINCE

DE Kelsey, IOH Fielding, MTD Wingate, RH Smithies, RE Turnbull, BV Ribeiro, R Maas, A Wainwright, CL Kirkland, K Goemann, SS Romano, M Dröllner

Access GSWA products

All products
All GSWA products are free to download as PDFs from the DEMIRS eBookshop <www.demirs.wa.gov.au/ebookshop>.
View other geoscience information on our website <www.demirs.wa.gov.au/gswa>.

Hard copies
Limited products are available to purchase as hard copies from the First Floor Counter at Mineral House or via the DEMIRS eBookshop <www.demirs.wa.gov.au/ebookshop>.

Fieldnotes
Fieldnotes is a free digital-only quarterly newsletter which provides regular updates to the State's exploration industry and geoscientists about GSWA's latest programs, products and services.
Access by subscribing to the GSWA eNewsletter <www.demirs.wa.gov.au/gswaenewsletter> or downloading the free PDF from the DEMIRS eBookshop <www.demirs.wa.gov.au/ebookshop>.

GSWA eNewsletter
The GSWA eNewsletter is an online newsletter that contains information on workshops, field trips, training and other events.
To keep informed, please subscribe <www.demirs.wa.gov.au/gswaenewsletter>.

Further details of geoscience products are available from:

First Floor Counter
Department of Energy, Mines, Industry Regulation and Safety
100 Plain Street
EAST PERTH WESTERN AUSTRALIA 6004
Phone: +61 8 9222 3626 Email: publications@demirs.wa.gov.au
www.demirs.wa.gov.au/GSWApublications